Scaling massive MIMO with imperfect transceivers

Sheikhi, Ashkan

2025

Document Version:
Publisher's PDF, also known as Version of record

Scaling Massive MIMO with Imperfect Transceivers

Ashkan Sheikhi

Lund 2025

"Scaling Massive MIMO with Imperfect Transceivers"

Series of licentiate and doctoral theses
No. 188
ISSN 1654-790X188
ISBN 978-91-8104-661-8 (print)
ISBN 978-91-8104-662-5 (pdf)

This thesis is produced by using the LaTeX Documentation System
Printed in Sweden by *Tryckeriet i E-huset*, Lund.

Department of Electrical and Information Technology
Lund University, Box 118, SE-221 00 Lund, Sweden

"My life is one long escape from myself."
S. Johnson

Popular Science

It has been more than two decade since we passed the point when majority of earth's population connected to the internet and gained full access to mobile communications. The number of connected devices however has been constantly and rapidly growing due to the emerging applications and services, such as smart vehicles, smart home, self-controlled robot workers, remote-controlled machinery, and so on. During recent years, not only the number of connected devices is increasing rapidly, but also the amount of information transmitted by each device over the wireless networks have been growing explosively. For example, smartphones are now capable of recording videos with resolutions beyond 4K and very high refresh rates, and most streaming platforms offer 4K quality by default. Online video games are constantly increasing their connectivity requirements, and new applications, such as virtual reality (VR) and augmented reality (AR), are now commercialized at a large scale. Therefore, the network demands are increasing significantly on a daily basis and the advancements in wireless technology are constantly struggling to keep up with the level of users demands.

Massive multiple-input multiple-output (MIMO) and large intelligent surface (LIS) are two of the major key technologies in the recent wave of advancements in 5G and 6G wireless networks. These technologies enable the network to serve multiple users with very high data rates and high reliability, by exploiting the spatial domain of the wireless channel. The performance gain from deploying these systems highly depends on the possibility to increase the number of transmit and receive antennas up to hundreds or thousands of elements. While in theory there can be infinite gain from scaling up these systems, deploying hundreds to thousands of transceiver chains with high-end hardware components limits the scalability of massive MIMO in terms of cost efficiency. High-end hardware components not only increase the deployment cost of such networks, but also may increase the power consumption of the transceivers and system infrastructure, which is not favorable both for the vendors and the environment. On the other hand, it may not be efficient to scale these systems arbitrarily with low-end hardware, since the real-world low-end

hardware components introduce distortion into these systems and limit their performance. Therefore, reducing the requirements on hardware components quality while maintaining the system performance is of great importance to enable the scalability of massive MIMO for future wireless networks.

In this thesis, we focus on scaling up massive MIMO and beyond with imperfect transceivers. In particular, we study the performance of massive MIMO and LIS systems with imperfect hardware components to analyze the scalability of these systems in practice. We also propose solutions to optimize the system performance while taking into account the non-ideal effects in hardware components. We propose compensations schemes to mitigate the effects of imperfect transceivers and we show that by adopting the proposed schemes, we can improve the overall systems efficiency, which paves the way for scaling up massive MIMO systems to meet the increasing demands in future wireless networks.

Abstract

The number of users and the information transmitted over wireless networks have been growing constantly during the last decades. Nowadays, the pace of this growth is extremely sharp because of the new applications which heavily rely on wireless networks to meet users' demands. Wireless networks infrastructures are constantly developing to meet these demands. Massive MIMO and LIS are two of the main technologies which are the key-enablers for the current and future wireless networks. The performance gains achieved from these system are mainly due to the large number of deployed transceiver chains, which enables serving more users by exploiting spatial domain multiplexing to meet the higher service requirements. The possibility to scale up these systems is a necessity to constantly meet the network demands. Deploying massive MIMO and LIS systems with non-ideal hardware components is of great importance to make the scalability of these systems feasible. In theory, the performance of these systems can grow unboundedly by scaling up the number of transceiver chains. However, assuming ideal hardware components for the transceivers is not realistic from a practical point of view, since the number of transceiver chains are in the order of hundreds to thousands, and the deployment cost, processing complexity, and power consumption can limit the scaling of such systems.

This work presents an analysis of hardware quality, complexity, power consumption, versus performance of wireless communication systems, with a particular focus on massive MIMO and LIS architectures. We derive closed-form scaling laws that relate analogue front ends (AFEs) power consumption to key system and environmental parameters, such as bandwidth, signal-to-noise-plus-distortion-ratio (SNDR), and fading conditions, enabling informed decisions for low-power design. For massive MIMO systems, we explore both traditional and machine learning-based digital pre-distortion (DPD) strategies. In particular, we propose optimization of per-antenna DPD sizes under hardware constraints and adaptive neural DPD allocation strategies based on channel conditions, demonstrating substantial capacity improvements and system cost reductions. We further analyze the effects of non-ideal receiver chains on LISs, and propose

efficient antenna and panel selection schemes to sustain LIS performance with fewer number of transceiver chains. Finally, we propose an over-the-air (OTA) method to jointly perform DPD and reciprocity calibration in massive MIMO and LIS systems, mitigating transmitter non-linearity and non-reciprocity without dedicated hardware or iterative algorithms. Collectively, these contributions provide new insights and tools for the design of energy- and cost-efficient wireless systems that remain robust under realistic hardware constraints.

Preface

This doctoral thesis summarizes the most relevant research contributions from my PhD studies at the department of Electrical and Information Technology (EIT), Lund University, Sweden.

The current thesis is comprised of Part I and Part II. Part I contains an overview of the research field in which I have been working during my PhD, including some useful preliminary knowledge and a brief contextualization of my contributions in this field. Part II is composed of 7 papers that constitute my contribution to the research field. The included papers are listed below, with a detailed contributions of the author.

List Of Included Papers

Paper I **A. Sheikhi**, F. Rusek, and O. Edfors, "Massive MIMO with Per-Antenna Digital Predistortion Size Optimization: Does it Help?," in *IEEE International Conference on Communications (ICC),*, Montreal, QC, Canada, 2021, pp. 1-6.

Personal contributions: I proposed the framework of the paper based on discussions with the co-authors. My contributions include the idea, problem definition, methodology, and the simulation results. I also took the lead role in writing the paper.

Paper II **A. Sheikhi** and O. Edfors, "Machine Learning Based Digital Pre-Distortion in Massive MIMO Systems: Complexity-Performance Tradeoffs," in *2023 IEEE Wireless Communications and Networking Conference (WCNC)*, Glasgow, United Kingdom, 2023, pp. 1-6.

Personal contributions: I proposed the framework of the paper based on discussions with the co-authors. My contributions include the idea, problem definition, methodology, and the simulation results. I also took the lead role in writing the paper.

Paper III **A. Sheikhi**, J. Vidal Alegría, and O. Edfors, "Large Intelligent Surfaces with Low-End Receivers: From Scaling to Antenna and Panel Selection," under revision for publication in *IEEE Transactions on Wireless Communications*, 2025.

Personal contributions: I proposed the framework of the paper based on discussions with the co-authors. My contributions include the idea, problem definition, methodology, and the simulation results. I also took the lead role in writing the paper.

Paper IV **A. Sheikhi**, J. Vidal Alegría, and O. Edfors, "Hardware Distortion Modeling for Panel Selection in Large Intelligent Surfaces," in *2024 58th Asilomar Conference on Signals, Systems, and Computers*, Pacific Grove, CA, USA, 2024, pp. 822-826.

Personal contributions: I proposed the framework of the paper based on discussions with the co-authors. My contributions include the idea, problem definition, methodology, and the simulation results. I also took the lead role in writing the paper.

Paper V **A. Sheikhi**, O. Edfors, and J. V. Alegría "Over-the-Air DPD and Reciprocity Calibration in Massive MIMO and Beyond," in *IEEE Wireless Communications Letters*, August 2025, [published, early access].

Personal contributions: I proposed the framework of the paper based on discussions with the co-authors. My contributions include the idea, problem definition, methodology, and the simulation results. I also took the lead role in writing the paper.

Paper VI **A. Sheikhi**, O. Edfors, and J. Vidal Alegría, "Over-the-Air DPD and Reciprocity Calibration for Panel-based Large Intelligent Surfaces" [Manuscript]

Personal contributions: I proposed the framework of the paper based on discussions with the co-authors. My contributions include the idea, problem definition, methodology, and the simulation results. I also took the lead role in writing the paper.

Paper VII M. Sarajlić, **A. Sheikhi**, L. Liu, H. Sjöland and O. Edfors, "Power Scaling Laws for Radio Receiver Front Ends," in *IEEE Transactions on Circuits and Systems I: Regular Papers*, vol. 68, no. 5, pp. 2183-2195, May 2021.

Personal contributions: I provided a theoretical validation for the proposed scaling laws in this paper. I have also contributed to the writing of the manuscript in the final revision.

Other Works

During my PhD, I have also contributed to the following works that are not included in this thesis:

- **A. Sheikhi**, S. M. Razavizadeh and I. Lee, "A Comparison of TDD and FDD Massive MIMO Systems Against Smart Jamming," in IEEE Access, vol. 8, pp. 72068-72077, 2020.
- **A. Sheikhi**, O Edfors, and F Rusek, "Determination of digital pre-distorter size of an access node," *US Patent App. 18/566,397, 2024, European Patent Granted, EP4348828B1, August 2025.*
- J. A. Andersson, S. Willhammar, and **A. Sheikhi**, "Hybrid Data Communication Lab – a Case Study," *Proceedings från LTHs 12:e Pedagogiska inspirationskonferensen*, (pp. 80-82).

Acknowledgements

I cannot write many words before mentioning Ove. Thank you for everything. The supervision part is definitely a minor part of what I'm grateful for. You have taught me so much on so many levels, you always had my back, no matter the situation, I always felt better after talking with you. Juan V., thank you for all your kind help during the later stages of this PhD. You made a huge difference. More importantly, I'm grateful for your friendship and all the fun we had over the years. The same applies to all my current and former colleagues at the EIT department here in Sweden. Working and socializing with such amazing people, from all over the world, has been an exceptional gift. I truly enjoyed it, I will always remember the good memories, and I'm deeply grateful for all the collaborations, fikas, lunches, department activities, deep conversations, laughter, and all your kind help during my PhD. I'm specifically thankful to Fredrik R., Johan T., Anders J., Michael L., Fredrik T., Vincent, Hedieh, Sara G., Christian N., Juan S., Neharika, Guoda, Liang, Umar, Jesus R., Baktash, Masoud J., Muris, Masoud N., Iman, Farnaz M., Fatemeh, Amir, Ilayda, Mojtaba, Hamid, Michiel S., Dino, Erik M., Xuhong, Xuesong, Alexei, Galina, Junshi, Amirreza, Andreia P., Sarah, Leif, Henrik S., Ali A., Lucas, Stefan H., Daniel S., Sirvan, Linda, Margit, Erik G., and Elisabeth.

My friends! You mean the world to me. You are truly like my family—except that I had a choice. I have cherished all the moments we've shared over the years. Spending time with you is one of the very few things in life that actually meant something to me.

My dear family! I love you, and I miss you every single day. Thank you for everything, and I hope I can see you again very soon. My love, Shiva! I can't find the right words to describe how grateful I am for all your kindness and love. Thank you for being the most caring person I have ever known.

Ashkan

List of Acronyms and Abbreviations

ADC	analogue to digital convertor
AFE	analogue front end
AGC	automatic gain control
AR	augmented reality
AWGN	additive white Gaussian noise
BB	base-band
BBU	baseband unit
BER	bit error rate
BS	base station
CRLB	Cramer-Rao Lower Bound
CSI	channel state information
DAC	digital to analogue convertor
DL	downlink
DPD	digital pre-distortion
EB	Exa byte
EE	energy efficiency
FDD	frequency-division duplexing
LIS	large intelligent surface
LMMSE	linear minimum mean squared error
LNA	low noise amplifier
LOS	line of sight

LS	least-squares
MIMO	multiple-input multiple-output
MRC	maximum ratio combining
MRT	maximum ratio transmission
MSE	mean square error
MU-MIMO	Multi-user MIMO
MVU	minimum-variance unbiased
NN	neural network
OFDM	orthogonal frequency-division multiplexing
OTA	over-the-air
PA	power amplifier
PAPR	peak-to-average power ratio
RF	radio frequency
RX	receiver
SDMA	space division multiple access
SISO	single-input-single-output
SNDR	signal-to-noise-plus-distortion-ratio
SNR	signal to noise ratio
TDD	time-division duplexing
TX	transmitter
UE	user equipment
UL	uplink
VR	virtual reality
ZF	zero-forcing

Notation

The following notation will be used throughout the remainder of this thesis:

- Lowercase, bold lowercase and bold uppercase letters are used for scalars, column vectors, and matrices, respectively.
- The operations $(\cdot)^{\mathrm{T}}$, $(\cdot)^*$ and $(\cdot)^{\mathrm{H}}$ denote transpose, conjugate, and conjugate transpose, respectively. Euclidean norm of a vector $\boldsymbol{a}$ is denoted by $\|\boldsymbol{a}\|$.
- A diagonal matrix $\boldsymbol{Q}$ with diagonal elements $a_1, a_2, \ldots, a_N$ is denoted by $\mathrm{diag}(a_1, a_2, \ldots, a_N)$. For a vector $\boldsymbol{v}$, $\mathrm{diag}(\boldsymbol{v})$ denotes a diagonal matrix with elements of $\boldsymbol{v}$ on the main diagonal.
- Identity matrix of size $N \times N$ is denoted by $\mathbf{I}_N$.
- $\Re\{A\}$ and $\Im\{A\}$ denote real and imaginary parts of a complex variable A, respectively.
- Zero-mean complex Gaussian random vector $\boldsymbol{a}$ with covariance matrix $\boldsymbol{C}$ is denoted by $\boldsymbol{a} \sim \mathcal{CN}(\boldsymbol{0}, \boldsymbol{C})$, and $\mathbb{E}\{\cdot\}$ denotes the expectation operator.

Contents

Part I

Overview of Research Field

Chapter 1

Introduction

This chapter provides a general introduction to this thesis. In Section 1.1, the main motivations behind the research conducted in this thesis is presented. Section 1.2 provides the scope of the thesis. In Section 1.3, the main goals of this thesis are remarked. Section 1.4, provides the outline of the thesis.

1.1 Thesis Context and Motivation

During the last 20 years, the number of wireless devices and the information transmitted over wireless networks have grown explosively [1], (see Fig. 1.1). Modern applications which heavily rely on the wireless networks to meet the users demands have emerged. As a result, wireless networks and circuit design for wireless transceivers have been two of the most important research topics in the world of technology. The development of 5G and emerging 6G infrastructures continues to evolve to meet these growing network demands [2]. Two key technologies driving this progress are Massive MIMO [3] and LIS [4], which serve as critical enablers for both current and future wireless networks. Their impressive performance gains largely stem from the deployment of a high number of transceiver chains, enabling greater user capacity through spatial multiplexing and supporting more demanding network requirements [5].

To keep pace with increasing demand, the ability to scale up massive MIMO systems is essential. In theory, the performance of these systems may increase indefinitely by deploying more transceiver chains [6]. However, this only holds under specific condition, such as assuming ideal hardware components, which is impractical in real-world scenarios—particularly when dealing with hundreds or thousands of transceiver chains. The associated costs, processing complexity, and power consumption present significant limitations. The power consumption of each transceiver can also become a bottleneck, especially if there are tight

Figure 1.1: Global mobile network data traffic and year-on-year growth (Exa byte (EB) per month) [1]

requirements on the non-linearity of amplifiers and the out-of-band emissions [7]. As a result, implementing Massive MIMO and LIS with imperfect hardware is crucial to ensure the scalability of these systems remains practical and cost-efficient [4], [5], [8]. Therefore, it is of high importance to, first, analyze the effects of imperfect transceivers when scaling up massive MIMO systems, and second, design compensation methods and optimizations to increase the cost efficiency when scaling up massive MIMO systems.

1.2 Thesis Scope

In practical wireless communication systems, hardware components often show non-ideal effects, introducing imperfections that can degrade system performance. These non-ideal effects include nonlinearities in power amplifiers, phase noise, I/Q imbalance in mixers, and quantization errors. Such impairments can affect the reliability of data transmission and quality of service for the users. To mitigate these effects, signal processing-based compensation techniques are used, including DPD, phase noise estimation, and calibration algorithms. Additionally, distortion-aware system design and smart signal processing algorithms can improve resilience against these non-ideal effects.

To deal with these challenges when scaling up massive MIMO systems, we need to make the transceiver design as efficient as possible. A potential direction to follow is to optimize the signal processing schemes and system architectures while maintaining the hardware quality at a minimum level. In other words, we want to get the most gain from each transceiver chain while limiting the implementation costs, e.g., by using inexpensive hardware components.

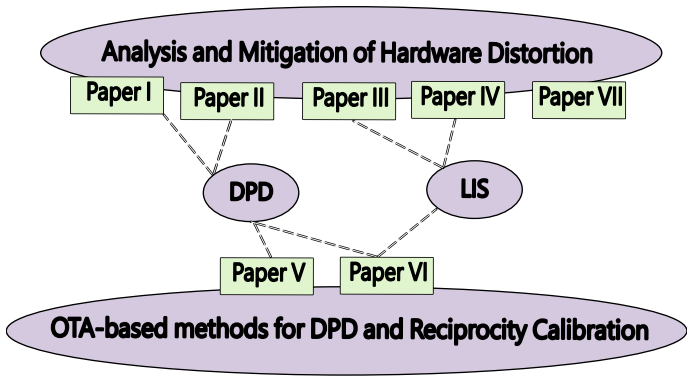

Figure 1.2: Thesis scope and papers categorization.

Therefore, providing methodologies and smart design through system-level optimizations is of great importance.

In this thesis, we first analyze the non-ideal effects with precise models and information theoretical derivations, and subsequently design smart optimization methods to mitigate the adverse effects of these non-ideal effects. To study the effects, we leverage statistical signal processing and information theory methods. However, the model selection is of high importance as well, since it implies a trade-off between accuracy and analytical tractability. We analyze the performance with different non-ideal effects and derive performance metrics which can be used for optimizing systems. Then, we leverage the mentioned analysis and define optimization problems to mitigate the effects of non-ideal hardware components. We also develop novel compensation methods based on low-complexity OTA measurements and machine learning to further improve systems performance.

1.3 Thesis Goals

The main thesis goal is to investigate the feasibility of scaling up massive MIMO and LIS systems with imperfect transceiver chains. In particular, the first goal of this thesis is to propose frameworks and provide analytical results to study the effects of imperfect transceivers when scaling up massive MIMO and beyond. Secondly, the thesis focuses on providing optimized schemes to mitigate the effects of hardware distortion on the system performance, by proposing DPD size optimization, OTA-DPD compensation, and antenna selection solutions. The thesis includes 7 papers, which are categorized as illustrated in Fig. 1.2. Connections between the papers contributions and the thesis goals are described with more details in Chapter 3.

1.4 Thesis Outline

This thesis consists of two parts. In Part I, an overview of the research field of the thesis is provided. In Chapter 1, an introduction to the subject is presented, including the thesis motivation and goals. Chapter 2 provides some related background knowledge which is essential to understanding the results of this thesis. Chapter 3 provides a detailed discussion of the contributions and results from the included papers. Chapter 4 presents the main conclusions based on the results of this thesis, and provides directions for future work based on the content of this thesis. In Part 2, the 7 papers included in the thesis are provided, with some changes of formatting to match the rest of the thesis.

Chapter 2

Related Background

In this chapter, fundamental concepts and definitions used in the thesis are briefly introduced. We first present basics of a communication system and the definition of capacity in Section 2.1. In Section 2.2, we provide some fundamental concepts of MIMO systems and their advantages with a general description of Multi-user MIMO (MU-MIMO) systems, which provides the basic framework for the technologies studied in this thesis. Section 2.3 includes fundamentals of massive MIMO system and beyond, including LIS systems, which are the two major technologies considered in this thesis. Then, we introduce basic components of a wireless transceiver in Section 2.4, followed by the non-ideal effects of imperfect transceivers in sections 2.5 and 2.5.1.

2.1 Communication System and Capacity

In the simplest format of a communication system, a transmitter sends some information, over a channel, to a receiver. The term channel refers to the medium connecting the transmitter and receiver, which can be wired or wireless. In the context of wireless communication systems, channel refers to the radio channel between a transmitter a receiver. In order to analyze a communication link, mathematical models are used for both the information transmitted between transmitter and receiver, and for the channel. In a simple form of a digital communication system, the signal received at a single-antenna receiver after going through a narrow-band channel can be modeled as

$$r = hs + n, \tag{2.1}$$

where the complex-valued variables s, h, and n model the symbols transmitted by a single-antenna transmitter, the channel, and the additive noise at the

receiver, respectively.

The concept of capacity was introduced by Claude Shannon, who is widely known as the "Father of Information Theory". In one of his main works titled "A mathematical theory of communication", he provided the definition of channel capacity, defined as "the highest information rate over a channel that can be achieved with arbitrary small error probability" [9]. For the single-input-single-output (SISO) communication system model in (2.1), the channel capacity is defined as

$$C_{\text{SISO}} = \max_{p(s)} \mathcal{I}[s;r], \tag{2.2}$$

where $\mathcal{I}[s;r]$ is the average mutual information between s and r. The maximization is performed over all the possible probability distributions of s given by $p(s)$. If we assume a zero-mean Gaussian distribution for n, with $\sigma^2 = \mathbb{E}[|n|^2]$, and perfect knowledge of h at the receiver, we can calculate the capacity as [10], [11]

$$C_{\text{SISO}} = \log_2\left(1 + \frac{P|h|^2}{\sigma^2}\right) \tag{2.3}$$

where $P = \mathbb{E}[|s|^2]$. In general, calculating the channel capacity is not trivial, and in many cases, we are only able to find some bounds on the capacity [12]. It can be seen from equation (2.3) that the SISO capacity grows with the ratio of received signal power and the noise variance, which we refer to as signal to noise ratio (SNR).

2.2 MIMO Communication Systems

MIMO technology has been a key technology in wireless networks for more than two decades. MIMO, in its original form, is also called point-to-point MIMO, and refers to a communication system where both the transmitter and the receiver have two or more antennas, as depicted in Fig. 2.1. By equipping the transmitter and receiver with multiple antennas, higher reliability and capacity can be achieved in the wireless channel, without requiring additional bandwidth or transmit power. In particular, there are three main advantages in MIMO scenarios [10], [13], [14]:

- Multiplexing: Increasing data throughput by sending independent data streams across different antennas, improving the capacity of wireless communication systems.
- Diversity: Transmitting the same data signal over multiple paths between antennas, improving the reliability of communication systems and reducing the system bit error rate (BER).

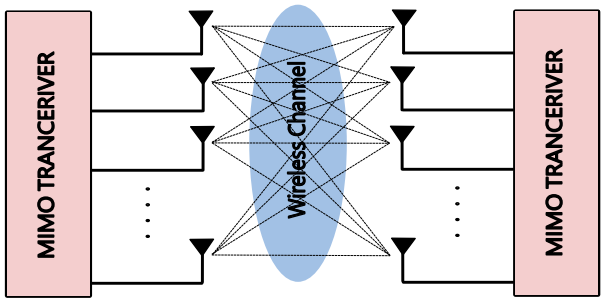

Figure 2.1: MIMO Wireless System.

- Array Gain: Increases the SNR by exploiting beamforming of the signal from transmitter to the receiver, focusing the transmitted energy in specific directions to improve signal quality and reduce interference, which improves the capacity of wireless communication systems.

2.2.1 MIMO Capacity

To define the MIMO capacity, we can generalize the formulation in Section 2.1, to a multiple-antenna transmitter and receiver. Assume that the transmitter and receiver have N_{TX} and N_{RX} antennas respectively. The received signal is modeled as

$$\boldsymbol{r} = \boldsymbol{H}\boldsymbol{s} + \boldsymbol{n}, \tag{2.4}$$

where $\boldsymbol{H}$ is a $N_{\mathrm{RX}} \times N_{\mathrm{TX}}$ channel matrix, $\boldsymbol{s}$ is the complex-valued transmitted symbol, and $\boldsymbol{n}$ is the additive zero-mean Gaussian noise. The capacity for the MIMO system can be derived as [10], [15]

$$C_{\mathrm{MIMO}} = \max_{\boldsymbol{R_{ss}}} \log_2 \left(\det \left[\boldsymbol{I}_{N_{\mathrm{RX}}} + \frac{1}{\sigma^2} \boldsymbol{H}\boldsymbol{R_{ss}}\boldsymbol{H}^H \right] \right) \tag{2.5}$$

where the transmitted signal and additive noise distributions are zero-mean Gaussian with covariance matrix $\boldsymbol{R_{ss}}$ and $\sigma^2 \boldsymbol{I}_{N_{\mathrm{RX}}}$, respectively. The MIMO channel is a random matrix and the capacity defined above is calculated for one realization of the channel. To evaluate the performance of the MIMO system over all the possible realizations of the channel, we can use the concept of ergodic capacity, which is defined as the average of the capacity, defined above, over all the realizations of the random channel matrix $\boldsymbol{H}$.

2.2.2 MU-MIMO

The concept of point-to-point MIMO was not directly applicable to a cellular wireless network where single-antenna users are not co-located and they can not

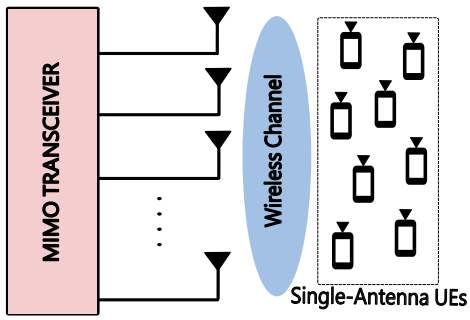

Figure 2.2: MU-MIMO Wireless System.

co-operate in the same way as one multi-antenna system. Therefore, a new class of MIMO systems were developed based on the original MIMO concept where many single-antenna user equipments (UEs) communicate with a multi-antenna base station (BS), commonly known as MU-MIMO, as illustrated in Fig. 2.2. It was shown that with smart signal processing steps during transmission and reception, i.e., in downlink (DL) and uplink (UL), the advantages of the original point-to-point MIMO technology can also be achieved in MU-MIMO systems [16], [17], [18].

Assume that a MIMO transceiver, i.e., BS, with M antennas, is serving K single-antenna UEs. The channel between the BS and UEs is modeled by a $M \times K$ matrix $\boldsymbol{H}$. In the UL, each UE transmits a signal s_k to the BS over $\boldsymbol{H}$. The received signal at the BS can be modeled as

$$\boldsymbol{y} = \boldsymbol{H}\boldsymbol{s} + \boldsymbol{n}, \tag{2.6}$$

where $\boldsymbol{s}$ is a $K \times 1$ vector containing all the signals s_k. Each column of the matrix $\boldsymbol{H}$ contains the channel vector $\boldsymbol{h}_k$ between the k'th UE and the BS. The BS can have an estimate of $\boldsymbol{H}$ if the UEs transmit pilots over the channel. Then, the BS can exploit the channel knowledge to recover the transmitted signals, by selecting a combining scheme. For example, the BS can use a zero-forcing (ZF) scheme, and multiply $\boldsymbol{y}$ with the pseudo-inverse of $\boldsymbol{H}$, given by

$$\boldsymbol{V}_{\text{ZF}} = (\boldsymbol{H}^H\boldsymbol{H})^{-1}\boldsymbol{H}^H \tag{2.7}$$

which can effectively cancel the inter-user interference.

To quantify the capacity of MU-MIMO, let's assume that the BS has full knowledge of $\boldsymbol{H}$ while the UEs have no information about the channel and cannot cop-operate. The constraint of the UEs not being able to cooperate means that they can only transmit independent symbols, thus enforcing $\boldsymbol{R_{ss}}$ to be diagonal. Assuming UEs with equal power available for transmission gives $\boldsymbol{R_{ss}} = P_s\boldsymbol{I}_K$, which incidentally coincides with the MIMO capacity-achieving

distribution when the channel is unknown at the transmitter. Therefore, the capacity of a MU-MIMO, with the setup as described above, is given by

$$C_{\text{MU-MIMO}} = \log_2 \left(\det \left[\boldsymbol{I}_M + \frac{P_s}{\sigma^2} \boldsymbol{H} \boldsymbol{H}^H \right] \right). \tag{2.8}$$

The MU-MIMO framework is the fundamental system model for massive MIMO and LIS, which we repeatedly consider throughout this thesis and the included papers.

2.3 Massive MIMO and Beyond

Massive MIMO was introduced in 2010 as a major advancement in MU-MIMO systems, in which the number of antennas at the BS scales up by one or more orders of magnitude [3]. This enhancement enables the system to exploit the spatial domain more effectively and serve many UEs with higher reliability and data rates [19]. It has been proven in both theory and practice that massive MIMO can provide a significant capacity boost in the communication network, which helps the system designers and the operators to meet the network requirements in 5G and beyond [5], [20]. With tens to hundreds of antenna elements deployed at the BS, massive MIMO has the potential to serve many UEs using space division multiple access (SDMA) with only linear and simple precoding and combining schemes, such as maximum ratio transmission (MRT) in DL and maximum ratio combining (MRC) in UL [6], [11]. Examples of massive MIMO array deployment scenarios are illustrated in Fig. 2.3.

2.3.1 Channel Hardening

One of the main properties of the wireless channels in massive MIMO systems is the channel hardening effect. It has been shown that by increasing the number of antenna elements, the wireless channel starts to behave deterministically [21], averaging out the small-scale fading effects. This results in a more stable effective channel to each UE, which is defined as the channel after performing precoding/combining. With a more deterministic and stable channel, the need for frequent power allocation and channel estimation is reduced, and the UEs can experience a more robust and reliable connectivity [22], [23], [24].

2.3.2 OFDM vs Single-Carrier

Massive MIMO can operate in both single-carrier and orthogonal frequency-division multiplexing (OFDM) transmission mode [25]. OFDM has shown great benefits for wide-band digital communications systems, especially for frequency-selective radio channel with multi-path propagation, by providing

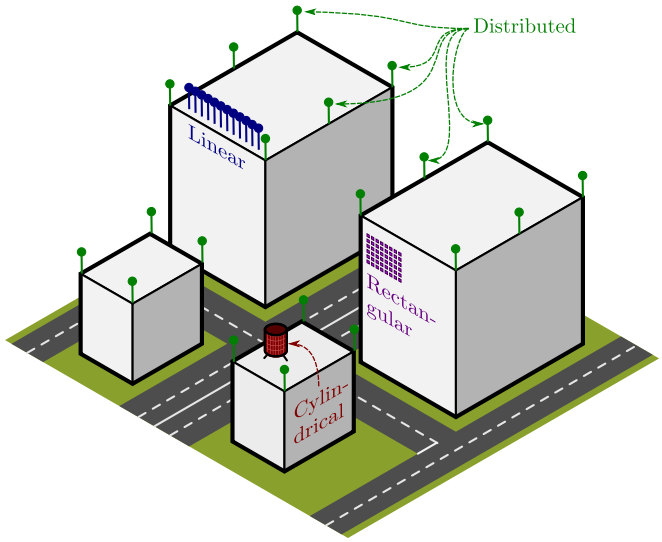

Figure 2.3: Massive MIMO array deployment examples in Wireless Networks [5].

better orthogonality in transmission channels without the need for complex equalization filters, improving inter-user interference cancellation [26], [27]. The authors in [25] proved that in massive MIMO, the performance of single-carrier and OFDM transmission are close in terms of the achievable rate, especially when the channel hardening effect is strong. The reason is that with channel hardening, all sub-carriers have equally good channels and the advantage of OFDM, which is the possibility to do water-filling in frequency domain, results in minor gain. Interestingly, the computational complexity of both transmission modes is also identical for massive MIMO [25]. However, there are differences when deploying massive MIMO in practice. For example, an OFDM massive MIMO system is less sensitive to time synchronization errors, while single-carrier system is less sensitive to errors in frequency synchronizations [25].

2.3.3 TDD mode

Massive MIMO was initially developed for time-division duplexing (TDD) systems, where UL and DL data are transmitted over the same frequency range, at different time intervals [3], [5]. The main advantage of this assumption is that the BS can rely on channel reciprocity to acquire the downlink channel from the uplink channel estimates [28], [29]. When massive MIMO was introduced, most of the commercial networks were operating in frequency-division duplexing (FDD) mode, and there were initial debates and discussions to en-

able deploying massive MIMO in FDD mode, mainly to reduce deployment costs [30]. However, later it was shown that to achieve the benefits of massive MIMO, operating in TDD mode is crucial. In TDD mode, the DL and UL channels are reciprocal and the number of pilots for channel estimation scales with the number of UEs. On the other hand, FDD mode could not exploit the channel reciprocity, and the number of downlink pilots for channel estimation scales with the number of BS antennas. For massive MIMO, where the number of BS antennas can grow large, the pilot overhead issue can limit the performance gain of increasing the number of antennas [31], [32]. Therefore, TDD was a clear choice and it is the standard mode considered in massive MIMO deployments [20].

2.3.4 Reciprocity Calibration

In an ideal TDD system, the massive MIMO BS can rely on perfect channel reciprocity, which means the BS can acquire the DL channel directly by transposing the estimated channel in UL. However, in practical deployments, the differences between transmitter (TX) and receiver (RX) hardware may compromise this assumption. In fact, ignoring these differences and directly using the UL channel can result in significant performance loss [28]. To deal with this problem, reciprocity calibration methods are used to compensate the difference between TX and RX hardware. There are several approaches for reciprocity calibration in massive MIMO. OTA-based reciprocity calibration methods relying on mutual-coupling measurements are specially promising since they do not require dedicated hardware for reciprocity calibration [28], [33], [34], [35].

In the literature of reciprocity calibration, the response of TX and RX hardware at both the BS and UEs are modeled by linear complex gains [1]. Let us denote the propagation channel from K UEs to the M-antenna BS by a $M \times K$ matrix $\boldsymbol{H}$. The effective UL channel which is affected by the BS RX and UEs TX hardware responses, is

$$\boldsymbol{H}_{\mathrm{UL}} = \boldsymbol{R}_{\mathrm{B}} \boldsymbol{H} \boldsymbol{T}_{\mathrm{U}}, \tag{2.9}$$

where $\boldsymbol{R}_{\mathrm{B}} = \mathrm{diag}(r_1^{\mathrm{B}}, \ldots, r_M^{\mathrm{B}})$ and $\boldsymbol{T}_{\mathrm{U}} = \mathrm{diag}(t_1^{\mathrm{U}}, \ldots, t_K^{\mathrm{U}})$ include the linear response of the BS RX and the UE TX hardware. If the BS simply transposes this matrix, it cannot acquire the DL channel, since the effective DL channel is

$$\boldsymbol{H}_{\mathrm{DL}} = \boldsymbol{R}_{\mathrm{U}} \boldsymbol{H}^{\mathrm{T}} \boldsymbol{T}_{\mathrm{B}}, \tag{2.10}$$

where $\boldsymbol{R}_{\mathrm{U}} = \mathrm{diag}(r_1^{\mathrm{U}}, \ldots, r_K^{\mathrm{U}})$, $\boldsymbol{T}_{\mathrm{B}} = \mathrm{diag}(t_1^{\mathrm{B}}, \ldots, t_M^{\mathrm{B}})$ are associated with the linear response of the UEs RX and BS TX hardware. The goal of reciprocity

[1] This assumption is idealistic. We propose reciprocity calibration methods with non-linearity at TX hardware in Paper V and Paper VI

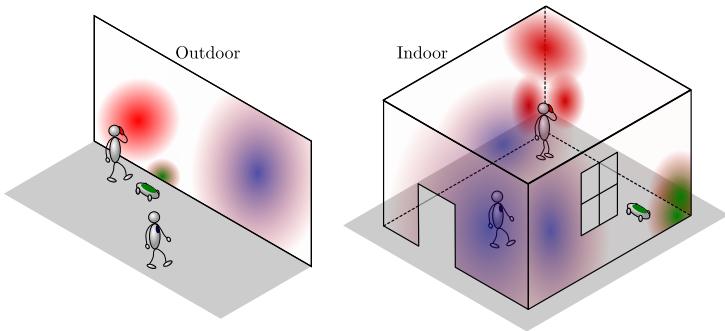

Figure 2.4: LIS deployment examples [4].

calibration is to compensate this difference. It has been shown that by estimating the reciprocity calibration matrix given by

$$\boldsymbol{C} = \boldsymbol{T}_{\mathrm{B}} \boldsymbol{R}_{\mathrm{B}}^{-1}. \tag{2.11}$$

The BS can effectively find a scaled version of $\boldsymbol{H}_{\mathrm{DL}}$ from $\boldsymbol{H}_{\mathrm{UL}}$, which can be deployed in DL precoding with a minimal performance loss compared to an ideal case with perfect knowledge of $\boldsymbol{H}_{\mathrm{DL}}$ [28], [36]. The OTA-based reciprocity calibration methods are considered in Paper V and Paper VI, where we propose OTA-based methods to perform both the DPD and reciprocity calibration.

2.3.5 LIS

LISs have emerged as one of the potential development directions after the deployment of massive MIMO systems. The LIS technology was introduced in [4], [37] as a large surface of electromagnetically active material, improving the communication system performance by enabling much higher degrees of freedom compared to massive MIMO systems. The initial theoretical model assumes a continuous model where any point of a surface can transmit and receive signals. While this continuous model is useful to understand the concepts and fundamental limits of a LIS system, it can not be implemented in that form with current technology. Instead, a dense antenna array deployed throughout a large surface is more realistic, which can also be interpreted as a sampled version of the continuous LIS model [4], [38]. More practical implementations of LIS consider dividing the surface into dense multi-antenna panels with a lower number of antennas on each panel, which is a more flexible and scalable design with reduced system complexity [39]. We deal with LIS and panel-based LIS systems in Paper III, Paper IV, and Paper VI.

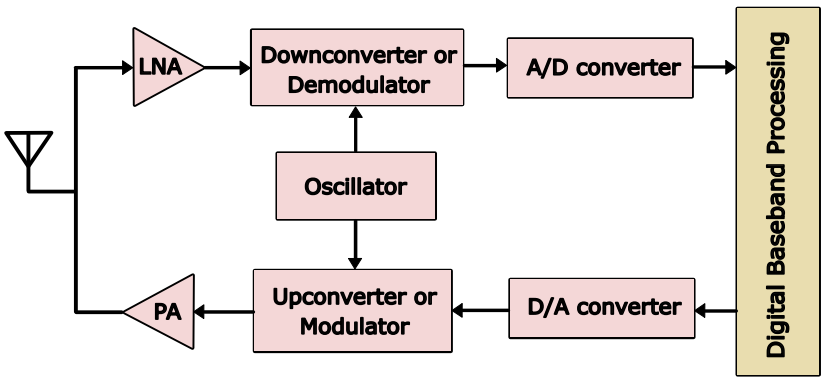

Figure 2.5: Wireless Transceiver.

2.4 Wireless Transceivers

Wireless transceivers are the core components of communication systems, enabling transmitting and receiving signals over the wireless channels. In a modern digital wireless system, the transmitter converts a source of information into a digital data by sampling and quantization. Then, the digital signal is transformed into an analog radio frequency (RF) signal using digital to analogue convertor (DAC) and modulation. The RF signal is transmitted through the channel from the transmit antennas. The receiver at the other side of the channel, receives the analogue signal from its receive antennas. An inverse operation is then performed on the received signal, where the signal is demodulated and digitized after going through an analogue to digital convertor (ADC) to recover the transmitted data. The main task of the receiver is to recover (detect) the transmitted information with minimum error. This whole process involves several stages, including filtering, amplification, frequency conversion, etc. The hardware architecture of a wireless transceiver includes many key components such as antennas, low noise amplifier (LNA), power amplifier (PA), mixers, oscillators, etc. In Fig. 2.5 a simple scheme of a wireless transceiver is illustrated [40].

2.5 Transceivers Imperfection

In practical wireless transceivers, hardware components often show non-ideal behavior, introducing various imperfections that can degrade the system performance. Most of the theoretical work in the area of massive MIMO disregard the non-ideal behavior of transceivers for analytical tractability. These non-ideal effects are mainly due to non-linearity in power amplifiers, phase noise in oscillators, In-phase Quadrature (I/Q) imbalance in mixers, and quantization errors

in low-resolution ADCs. Such impairments can lead to signal distortion, spectral regrowth, and reduced SNDR, limiting the performance of wireless systems [41]. For example, power amplifier non-linearities can cause inter-modulation distortion which generates in-band and out-of-band distortion and degrade the SNDR [40]. Understanding and addressing these non-ideal effects is essential for designing reliable and efficient wireless communication systems. It has been suggested that massive MIMO is generally more resilient to some effects from hardware impairments [42] mainly because those impairments are averaged out over many transceiver chains. However, those studies are only considering simple statistical models to analyze the imperfect hardware effects. On the other hand, the problem with imperfect transceiver is still crucial to consider when scaling up massive MIMO systems, mainly because in massive MIMO and beyond, due to a large number of TX-chains and RX-chain, deploying low-power and low-cost components are favorable for the sake of cost-efficiency. Accurate modeling and analysis of the non-ideal effects, and compensation methods to mitigate the effects of the hardware distortion are of great importance for such systems.

To deal with the challenges mentioned above, we need to make the massive MIMO and LIS transceiver design as efficient as possible. In general, the path to follow is to optimize the signal processing schemes and system designs to enable deploying lower-quality and lower-cost hardware components while maintaining the performance at a favorable level. In other words, we want to get the most gain from each transceiver chain while limiting the implementation costs, e.g., by using inexpensive hardware components. The main aim of this thesis is to provide methodologies and smart design through system-level optimizations to mitigate the effects of non-ideal hardware components in future MIMO systems. We need to study these effects by selecting high-accuracy models, performing information theoretical analysis, and subsequently designing smart optimization methods to mitigate the adverse effects. However, the model selection is of high importance as well since it results in a trade-off between accuracy and analytical tractability. In this thesis, we analyze the performance with different non-ideal effects and derive performance metrics which can be used for optimizing the systems. Then, we can leverage the analysis from above and define optimization problems to mitigate the effects of non-ideal hardware components. We can also develop novel compensation methods based on low-complexity OTA measurements and machine learning to further improve the system performance.

2.5.1 Modeling Hardware Impairment

One of the most crucial steps in analyzing massive MIMO systems with imperfect transceivers is the model selection. As remarked earlier, the model selection is important because it leads to a trade-off between accuracy and

analytical tractability. For this reason, most of the theoretical works on this subject consider the most simplistic models for hardware impairment. It is very common in the literature to model the residual hardware impairment[2] as an additive complex Gaussian distortion at the output, which is therefore treated as noise. This model is partly motivated based on the central limit theorem, by assuming that the residual hardware impairment is an aggregate effect of several hardware impairment effects [42], [43]. When considering this model for a transceiver with hardware impairment, the variance of the additive distortion term, i.e., distortion power, is proportional to the input power of the transceiver [43], [44], [45]. Let us consider the SISO system from Section 2.1, where both the TX and RX have hardware impairment. The received signal can be modeled as

$$r = h(s + \eta_t) + \eta_r + n, \tag{2.12}$$

where $\eta_t \sim \mathcal{CN}(0, \kappa_t P)$ and $\eta_r \sim \mathcal{CN}(0, \kappa_r P|h|^2)$, as remarked above. The scalar variables κ_t and κ_r can be interpreted as the level of hardware impairment, i.e., for an ideal system $\kappa_t = \kappa_r = 0$. The additive distortion terms in this model are assumed independent of the desired signal s. Therefore, we can treat them as noise in the capacity calculation, resulting in

$$C_{\text{SISO}} = \log_2 \left(1 + \frac{P|h|^2}{\kappa_t P + \kappa_r P|h|^2 + \sigma^2} \right). \tag{2.13}$$

While this statistical model can be adopted to gain insights about the hardware impairment effects with high analytical tractability, it is not accurate enough when considering specific hardware impairment effects. There are more complicated models with higher accuracy, which are generally known as behavioral models [46], [47], [48].

2.5.2 DPD

To mitigate the performance degradation caused by non-ideal hardware effects in wireless transceivers, compensation methods such as linearization and calibration are performed at both TX and RX. Linearization techniques are primarily employed to address the nonlinear behavior in PAs. A prominent method is DPD, which applies an inverse nonlinear function to the input signal, effectively canceling the distortion introduced by the amplifier [46], [49], [50], [51], [52]. This allows for more efficient amplifier operation near saturation without significantly increasing distortion, thereby improving spectral efficiency and power usage. We deal with DPD and optimization problems regarding DPDs in Paper I, Paper II, Paper V, and Paper VI.

[2]It is called the "residual" hardware impairment since it is assumed that mitigation techniques have been applied to compensate the impairment effects while some of the adverse effects remain even after the compensations.

DPDs are mainly designed based on the Volterra series and memory polynomial models [46]. Another class of DPDs, gaining more interest in recent years due to the new wave of machine learning applications, is neural network (NN)-DPD. It has been shown that a well-designed and well-trained NN-DPD can outperform the conventional DPDs at the same level of complexity and power consumption [53], [54], [55]. Most of the works in this regard are focusing on designing a novel low-complexity design of an NN-DPD for a single transceiver chain. We deal with NN-DPD schemes for massive MIMO in Paper II.

2.5.3 Non-linearity

Non-linearity is one of the most dominant effects when analyzing imperfect transceivers in MIMO system. While the main source of non-linearity is the PA in TX, other components in TX and RX can also show adverse non-linear behaviors. To understand the effect of non-linearity in a transceiver, let us consider an amplifier where the output is $y = f(x)$. For an ideal amplifier, $f(x) = Gx$, where G is the amplifier gain. However, when the input power of the amplifier grows large, the output is no longer a linear function of the input, and non-linearity effects appear. The non-linearity effect in this model is memory-less, while in practice there can be non-linearity with memory, i.e., the output at time t depends on the input at t and before [56]. For the memory-less case, approximating the non-linear function $f(x)$ can effectively model the non-linear effects of amplifier with high accuracy [40], [46]. In that case, the output is modeled by

$$y = f(x) = \sum_{k=0}^{L-1} a_{2k+1}\ x|x|^{2k}, \tag{2.14}$$

where a_{2k+1} are the model parameters. As it can be seen, only the odd-order terms are considered in the model. The motivation behind ignoring even-order terms is because those terms result in harmonics which are typically far from the frequency band of the signal. On the other hand, the odd-order terms are the ones with a dominant in-band and out-of-band distortion, due to adverse effects such as gain compression and inter-modulation [40]. Behavioral models such as the memory-less polynomial model above or memory polynomial models as the one considered in [56], can be leveraged to model and analyze other hardware impairment effects such as cross-talk [47], or the aggregated non-linear effects of all the components in a TX-chain or RX-chain. The model parameters can be estimated based on input-output measurements of the non-linear component [57], or by exploiting OTA measurements [58].

The effect of non-linearity in a massive MIMO system is more severe when the input power to the amplifiers grows high. This is especially important in

the PA of the BS, and dealing with the non-linearity at the TX in BS side with DPD methods is crucial to improve the DL performance. The PA non-linearity issue can be more severe when deploying massive MIMO with an OFDM transmission. The main reason is that, compared to a single-carrier transmission, OFDM has a higher peak-to-average power ratio (PAPR) which can result in higher non-linear effects at the PAs. Therefore, considering higher-complexity DPDs and memory-effects is more important for an OFDM massive MIMO system [59], [60].

2.5.4 Bussgang Decomposition

As remarked previously, analyzing the performance of a wireless system with non-linear components results in high-complexity formulations, which reduces the analytical tractability of the analysis. To deal with this high-complexity and simplify the problems, we can leverage the Bussgang decomposition [61], [62], [63], which is a direct result of the original Bussgang theorem [64]. Let us assume a non-linear component with input-output function given by

$$y = f(x), \tag{2.15}$$

where x and y are two complex random variables. In the context of wireless transceivers, x and y can be the input and output of a PA. The Bussgang decomposition can be applied to this non-linear function as

$$y = Bx + \eta, \tag{2.16}$$

where

$$B = \frac{C_{yx}}{C_{xx}} = \frac{\mathbb{E}\left[yx^*\right]}{\mathbb{E}\left[|x|^2\right]}, \tag{2.17}$$

is the Bussgang gain, and $\eta = f(x) - Bx$ is a zero-mean random variable uncorrelated to both x and y [62]. One should note that, while η and x are uncorrelated, they are generally not independent. The Bussgang decomposition can be interpreted as the linear minimum mean squared error (LMMSE) of y given x, where η is the estimation error. In case of a MIMO non-linear system with input $\boldsymbol{x}$ and output y, the same decomposition can be applied with the Bussgang gain defined as a matrix given by

$$\boldsymbol{B} = \boldsymbol{C}_{yx}\boldsymbol{C}_{xx}^{-1} = \mathbb{E}\left[\boldsymbol{y}\boldsymbol{x}^H\right]\left(\mathbb{E}\left[\boldsymbol{x}\boldsymbol{x}^H\right]\right)^{-1}. \tag{2.18}$$

The Bussgang decomposition is a very useful tool in analyzing the performance of imperfect transceivers with non-linear TX and RX chains, including non-linear amplifiers, low-resolution ADCs, etc [62]. We have leveraged this decomposition in Paper III and Paper IV.

Chapter 3

Overview of thesis contributions

In this chapter, a summary of thesis contributions is presented. The thesis includes 7 papers, all related to the general background covered in Chapters 2, categorized as illustrated in Fig. 1.2. For each paper, a brief summary of the results is provided, all in connection to the thesis goals from Chapter 1.

3.1 Paper I: Massive MIMO with Per-Antenna Digital Predistortion Size Optimization: Does it Help?

When deploying large arrays in massive MIMO scenarios, not all the antennas contribute equally to the system performance. Therefore, antenna selection schemes can be performed to use only a portion of the array for signal transmission [65]. With the same motivation, we have proposed to optimize the per-antenna DPD sizes in a DL massive MIMO system with residual hardware impairment. In particular, we first quantify the capacity after applying per-antenna DPD with different numbers of coefficients at each antenna and then maximize the capacity by finding optimum values of the per-antenna DPD sizes under a constraint on the total number of DPD coefficients in the system. Two closed-form sub-optimal solutions are derived and numerical examples illustrate that their performance is very close to the optimal solution. It is shown that, when the channel large-scale gains have high variation over the transmitter array, which is the case in practical scenarios, using our proposed optimized DPD sizes can improve the system capacity significantly. This allows us to scale down the massive MIMO system but still maintain performance. We also

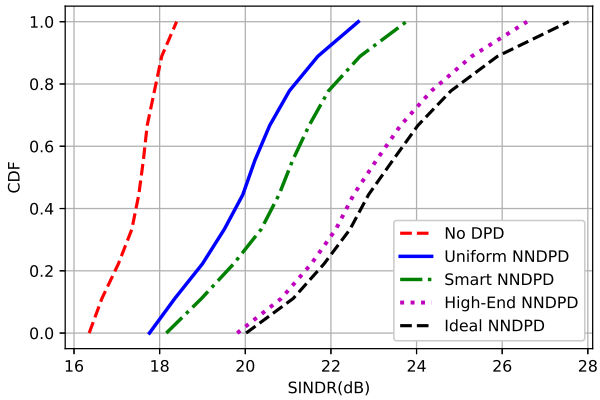

Figure 3.1: CDF of SINDR (dB) for a UE randomly located at the cell area [67],(Paper II).

study the asymptotic behavior of the derived capacity and show that by using the optimized DPD sizes, the system performance can approach the asymptotic bound with a significantly smaller number of antennas [66],(Paper I).

3.2 Paper II: Machine Learning Based Digital Pre-Distortion in Massive MIMO Systems: Complexity-Performance Trade-offs

With the same motivation and based on the results from [65], [66], we have considered the trade-off between complexity and performance in massive MIMO systems with NN-DPD blocks at the base station. In particular, we consider a multi-user massive MIMO system with per-antenna NN-DPDs, each with an adjustable NN architecture in terms of the size and the number of NN hidden layers. We first analyze the system performance in terms of compensation of the non-linear hardware distortion for different levels of NN-DPD complexity and number of antennas. We illustrate the required level of complexity in the trained NN-DPD blocks to approach the performance of an ideal conventional DPD. The statistics of the signal to interference and noise plus distortion ratio for a randomly located UE are selected as the performance metrics. We then assume a limited total digital computation power to be allocated among the NN-DPD blocks and propose to select the NN-DPD architecture of each TX branch based on the channel conditions of its corresponding antenna. To illustrate the importance of such a smart DPD resource allocation, we have

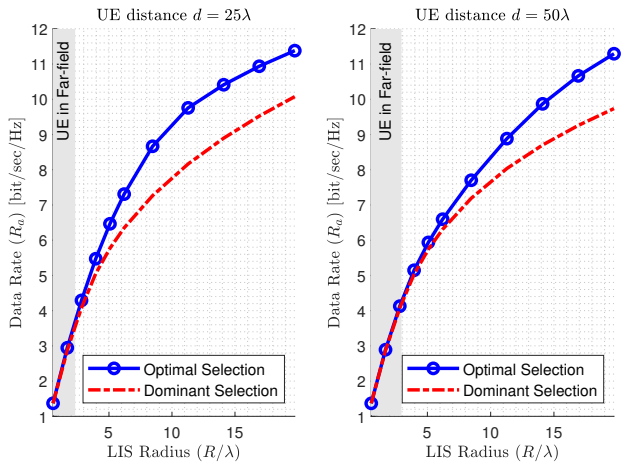

Figure 3.2: Achievable data rate with perfect AGC vs LIS radius in terms of number of wavelengths, λ, with fixed back-off for optimal antenna selection solved from (42) and dominant antenna selection where the antennas with highest received power are selected [68],(Paper III).

analyzed the performance of a massive MIMO system with different NN-DPD architecture selection strategies. Numerical results, such as Fig. 3.1, indicate that by adopting the smart NN-DPD resource allocation, a significant boost in the system performance can be achieved, making room for reducing the overall system cost when scaling a massive MIMO system [67],(Paper II).

3.3 Paper III: Large Intelligent Surfaces with Low-End Receivers: From Scaling to Antenna and Panel Selection

We analyze the performance of LIS with hardware distortion at its RX-chains. In particular, we consider the memory-less polynomial model for non-ideal hardware and derive analytical expressions for the signal to noise plus distortion ratio after applying MRC at the LIS. We also study the effect of back-off and automatic gain control on the RX-chains. The derived expressions enable us to evaluate the scalability of LIS when hardware impairments are present. We also study the cost of assuming ideal hardware by analyzing the minimum scaling required to achieve the same performance with non-ideal hardware. Then, we exploit the analytical expressions to propose optimized antenna selection schemes for LIS and we show that such schemes can improve the performance significantly, with Fig. 3.2 included here as an example. In particular, the

antenna selection schemes allow the LIS to have lower number of non-ideal RX-chains for signal reception while maintaining a good performance. We also consider a more practical case where the LIS is deployed as a grid of multi-antenna panels, and we propose panel selection schemes to optimize the complexity-performance trade-offs and improve the system overall efficiency [68],(Paper III).

3.4 Paper IV: Hardware Distortion Modeling for Panel Selection in Large Intelligent Surfaces

Hardware distortion in LISs may limit their performance when scaling up such systems. It is of great importance to model the non-ideal effects in their transceivers to study the hardware distortions that can affect their performance. Therefore, we have focused on modeling and studying the effects of nonlinear RX-chains in LISs. We first derive expressions for SNDR of a LIS with a memory-less polynomial-based model at its RX-chains. Then, we propose a simplified double-parameter exponential model for the distortion power and show that, compared to the polynomial based model, the exponential model can improve the analytical tractability for SNDR optimization problems. In particular, we consider panel selection optimization problems in a panel-based LIS scenario and show that the proposed model enables us to derive two closed-form sub-optimal solutions for panel selection, and can be a favorable alternative to high-order polynomial models in terms of computation complexity, especially for theoretical works on hardware distortion in MIMO and LIS systems. Numerical results show that the sub-optimal closed-form solutions have a near-optimal performance in terms of SNDR compared to the global optimum found by high-complexity heuristic search methods [69],(Paper IV).

3.5 Paper V: Over-the-Air DPD and Reciprocity Calibration in Massive MIMO and Beyond

Non-linear transceivers and non-reciprocity of downlink and uplink channels are two major challenges in the deployment of MIMO systems. We consider an OTA approach for DPD and reciprocity calibration to jointly address these issues. In particular, we consider a memory-less non-linearity model for the BS transmitters, and we propose a method to linearize the transmitters and perform the calibration by using mutual coupling OTA measurements between BS antennas. We show that, by using only the OTA-based data, we can linearize

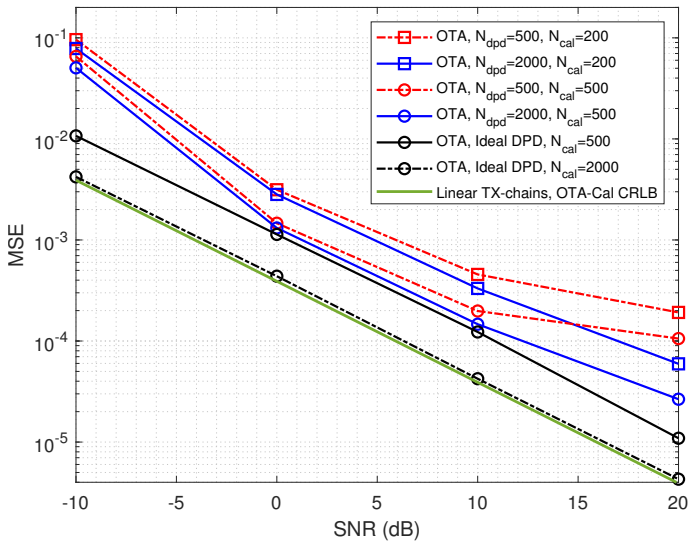

Figure 3.3: Average mean square error (MSE) of calibration matrix estimation using the proposed OTA-based DPD and Calibration. [58],(Paper V)

the transmitters and design the calibration to compensate for both the non-linearity and non-reciprocity of BS transceivers effectively. This allows us to alleviate the requirement to have dedicated hardware modules for transceiver characterization. Moreover, the proposed reciprocity calibration method is solely based on closed-form linear transformations, achieving a significant complexity reduction over state-of-the-art methods, which usually rely on costly iterative computations. Simulation results, such as Fig. 3.3, showcase the potential of our approach in terms of the calibration matrix estimation error and downlink data-rates when applying ZF precoding after using our OTA-based DPD and reciprocity calibration method [58],(Paper V).

3.6 Paper VI: Over-the-Air DPD and Reciprocity Calibration for Panel-based Large Intelligent Surfaces

We consider OTA-based DPD and reciprocity calibration methods for LISs systems. We first show the feasibility of performing OTA-DPD and calibration in LIS with non-linear transmitters modeled by an arbitrarily-high order polynomial. While the OTA-based method can be effective for LIS systems in general, its performance can be degraded under specific channel conditions, especially in panel-based LIS deployments which, is widely considered as a more prac-

tical implementation scheme for LIS. Therefore, we propose specific methods to improve the performance of the OTA-based methods for panel-based LIS scenarios. We show that, under certain conditions such as severe channel attenuation between certain panels, the original OTA-based method performance degrades. We propose two techniques to improve the performance under such conditions. Numerical results show that the proposed techniques can improve the performance of the OTA-based methods significantly, effectively enabling the OTA-DPD and calibration for practical panel-based LIS systems [Paper VI].

3.7 Paper VII: Power Scaling Laws for Radio Receiver Front Ends

We combine practically verified results from circuit theory with communication-theoretic laws. As a result, we obtain closed-form theoretical expressions linking fundamental system design and environment parameters with the power consumption of analog front ends (AFEs) for communication receivers. This collection of scaling laws and bounds is meant to serve as a theoretical reference for practical low power AFE design. We show how AFE power consumption scales with bandwidth, *SNDR*, and *SIR*. We build our analysis based on two well established power consumption studies and show that, although they have different design approaches, they lead to the same scaling laws. The obtained scaling laws are subsequently used to derive relations between AFE power consumption and several other important communication system parameters, namely, digital modulation constellation size, symbol error probability, error control coding gain, and coding rate. Such relations, in turn, can be used when deciding which system design strategies to adopt for low-power applications. For instance, we show how AFE power scales with environment parameters if the performance is kept constant and we use these results to illustrate that adapting to fading fluctuations can theoretically reduce AFE power consumption by at least 20x [7],(Paper VII).

Chapter 4

Conclusions and Future Work

This chapter summarizes the main conclusions of the thesis, and provides a connection between the papers results and the thesis goals introduced in Chapter 1. Directions for future work based on this thesis, and a general outlook on the topic is also provided at the end of this chapter.

4.1 Conclusions

In this thesis, we have mainly focused on two questions:

1. How does transceivers imperfection affect the scaling of massive MIMO and LIS for future wireless networks?

2. What possible compensation problems and system optimizations can be performed to mitigate the effects of the imperfect transceiver when scaling up massive MIMO?

To answer question 1, we first focused on studying the performance of massive MIMO and LIS systems with non-ideal hardware distortion. In particular, we conducted a theoretical work on this subject by selecting precise but analytically friendly models for the imperfect transceiver chains, and derived analytical expressions to study the scaling behaviors of massive MIMO and LIS systems with non-linear transceivers. We show that hardware distortion can be an important factor which limits the potential gains of these systems when scaling up the number of antennas and transceiver chains. Such analysis provides a better understanding on the impact of deploying hardware components of a certain quality in the design and implementation of massive MIMO

and LIS systems. Furthermore, we derive scaling laws relating the power consumption, bandwidth, non-linearity, and performance of receiver AFEs, which can be leveraged for receiver design and power budgeting of the AFEs for low-power receivers in massive MIMO and beyond. These results, which are partly answering question 1, are presented in all the 7 included papers.

For question 2, we use the results and analytical expressions to propose smart compensation methods, define optimization problems, and propose solutions to mitigate the adverse effects of non-ideal hardware components in imperfect transceivers. The mitigation solutions are mainly proposed in terms of DPD schemes, DPD resources optimization, and antenna selection methods, which are presented in papers I-V and VII. We explain the proposed solutions briefly here. We show that by optimizing the DPD resources, both conventional and NN-DPDs, based on antennas contribution, we can improve the system performance significantly, which means that the designer can use hardware components with lower quality while maintaining the system performance. We have also proposed OTA-based methods to perform the DPD and reciprocity calibration in massive MIMO and LIS systems. We show that we can leverage the same hardware and links that are already used for reciprocity calibration to perform the DPD, effectively reducing the need for complex DPD blocks and enabling higher scaling gains. We also proposed antenna selection and panel selection schemes for LIS systems with hardware distortion, and showed that by taking into account the hardware distortion in antenna and pane selection schemes, we can improve the system performance, which can alleviate the scaling challenges in LIS systems.

To summarize the conclusions, this thesis provides analytical results to illustrate and formulate the adverse effect of non-ideal hardware components in massive MIMO and LIS systems, and shows that, although the hardware distortion can be a limiting factor when scaling up these systems, we can deploy smart DPD and antenna selection schemes to mitigate the adverse effects of hardware distortion and therefore facilitate the scaling of massive MIMO and beyond.

4.2 Future Work

While we have tried to study the effect of hardware distortion on massive MIMO and LIS, and we have proposed solutions to improve system performance and mitigate the adverse effects of hardware distortion, there are still many open problems and unanswered questions around the subject. In general, higher accuracy in the models considered for hardware distortion can strengthen the analysis, with the cost of higher complexity and less analytical tractability. The main challenge for those models is the computation complexity of the corresponding schemes, which may suggest that more focus on data-based methods

such as NN-DPDs is of great importance. On the other hand, considering other non-ideal effects such as low-resolution ADCs, phase noise, and out of band distortions from amplifiers, either jointly or individually, can be beneficial to further generalize the results of this thesis. OTA-based methods to compensate non-linearity and reciprocity calibration with more general hardware models and different channel models, combined with more rigorous and optimized estimation methods, can be a potential follow-up path for future work based on this thesis. Generalizing the results from this thesis for wideband OFDM transmission method and studying the differences can also be a potential direction for future work.

References

[1] "Ericsson mobility report," *Technical report*, Feb. 2025.

[2] C.-X. Wang et al., "On the road to 6G: Visions, requirements, key technologies, and testbeds," *IEEE Communications Surveys & Tutorials*, vol. 25, no. 2, pp. 905–974, 2023.

[3] T. L. Marzetta, "Noncooperative cellular wireless with unlimited numbers of base station antennas," *IEEE Transactions on Wireless Communications*, vol. 9, no. 11, pp. 3590–3600, 2010.

[4] S. Hu, F. Rusek, and O. Edfors, "Beyond massive MIMO: The potential of data transmission with large intelligent surfaces," *IEEE Transactions on Signal Processing*, vol. 66, no. 10, pp. 2746–2758, 2018.

[5] E. G. Larsson, O. Edfors, F. Tufvesson, and T. L. Marzetta, "Massive MIMO for next generation wireless systems," *IEEE Communications Magazine*, vol. 52, no. 2, pp. 186–195, 2014.

[6] E. Björnson, J. Hoydis, and L. Sanguinetti, "Massive MIMO has unlimited capacity," *IEEE Transactions on Wireless Communications*, vol. 17, no. 1, pp. 574–590, 2018.

[7] M. Sarajlić, A. Sheikhi, L. Liu, H. Sjöland, and O. Edfors, "Power scaling laws for radio receiver front ends," *IEEE Transactions on Circuits and Systems I: Regular Papers*, vol. 68, no. 5, pp. 2183–2195, 2021.

[8] F. Rusek et al., "Scaling up MIMO: Opportunities and challenges with very large arrays," *IEEE Signal Processing Magazine*, vol. 30, no. 1, pp. 40–60, 2013.

[9] C. E. Shannon, "A mathematical theory of communication," *The Bell System Technical Journal*, vol. 27, no. 3, pp. 379–423, 1948.

[10] J. R. Hampton, *Introduction to MIMO communications*. Cambridge university press, 2013.

[11] E. Björnson, J. Hoydis, and L. Sanguinetti, "Massive MIMO networks: Spectral, energy, and hardware efficiency," *Foundations and Trends® in Signal Processing*, vol. 11, no. 3-4, pp. 154–655, 2017.

[12] A. Goldsmith, *Wireless Communications*. USA: Cambridge University Press, 2005.

[13] R. W. Heath Jr and A. Lozano, *Foundations of MIMO communication*. Cambridge University Press, 2018.

[14] A. PAULRAJ, D. GORE, R. NABAR, and H. BOLCSKEI, "An overview of MIMO communications - a key to gigabit wireless," *Proceedings of the IEEE*, vol. 92, no. 2, pp. 198–218, 2004.

[15] E. Telatar, "Capacity of multi-antenna gaussian channels," *European Transactions on Telecommunications*, vol. 10, no. 6, pp. 585–595, 1999.

[16] P. Viswanath and D. Tse, "Sum capacity of the vector gaussian broadcast channel and uplink–downlink duality," *IEEE Transactions on Information Theory*, vol. 49, no. 8, pp. 1912–1921, 2003.

[17] G. Caire and S. Shamai, "On the achievable throughput of a multiantenna Gaussian broadcast channel," *IEEE Transactions on Information Theory*, vol. 49, no. 7, pp. 1691–1706, 2003.

[18] D. Tse and P. Viswanath, *Fundamentals of Wireless Communication.* Cambridge University Press, 2005.

[19] F. Rusek et al., "Scaling up MIMO: Opportunities and challenges with very large arrays," *IEEE Signal Processing Magazine*, vol. 30, no. 1, pp. 40–60, 2013.

[20] E. Björnson, L. Sanguinetti, H. Wymeersch, J. Hoydis, and T. L. Marzetta, "Massive MIMO is a reality—what is next?: Five promising research directions for antenna arrays," *Digital Signal Processing*, vol. 94, pp. 3–20, 2019, Special Issue on Source Localization in Massive MIMO.

[21] B. Hochwald, T. Marzetta, and V. Tarokh, "Multiple-antenna channel hardening and its implications for rate feedback and scheduling," *IEEE Transactions on Information Theory*, vol. 50, no. 9, pp. 1893–1909, 2004.

[22] H. Q. Ngo and E. G. Larsson, "No downlink pilots are needed in TDD massive MIMO," *IEEE Transactions on Wireless Communications*, vol. 16, no. 5, pp. 2921–2935, 2017.

[23] S. Willhammar, J. Flordelis, L. Van der Perre, and F. Tufvesson, "Channel hardening in massive MIMO - a measurement based analysis," in *2018 IEEE 19th International Workshop on Signal Processing Advances in Wireless Communications (SPAWC)*, 2018, pp. 1–5.

[24] S. Willhammar, J. Flordelis, L. Van Der Perre, and F. Tufvesson, "Channel hardening in massive MIMO: Model parameters and experimental assessment," *IEEE Open Journal of the Communications Society*, vol. 1, pp. 501–512, 2020.

[25] C. Mollén, E. G. Larsson, and T. Eriksson, "Waveforms for the massive MIMO downlink: Amplifier efficiency, distortion, and performance," *IEEE Transactions on Communications*, vol. 64, no. 12, pp. 5050–5063, 2016.

[26] S. B. Weinstein, "The history of orthogonal frequency-division multiplexing [history of communications]," *IEEE Communications Magazine*, vol. 47, no. 11, pp. 26–35, 2009.

[27] R. W. Chang, "Synthesis of band-limited orthogonal signals for multichannel data transmission," *The Bell System Technical Journal*, vol. 45, no. 10, pp. 1775–1796, 1966.

[28] J. Vieira, F. Rusek, O. Edfors, S. Malkowsky, L. Liu, and F. Tufvesson, "Reciprocity calibration for massive MIMO: Proposal, modeling, and validation," *IEEE Transactions on Wireless Communications*, vol. 16, no. 5, pp. 3042–3056, 2017.

[29] H. Wei, D. Wang, H. Zhu, J. Wang, S. Sun, and X. You, "Mutual coupling calibration for multiuser massive MIMO systems," *IEEE Transactions on Wireless Communications*, vol. 15, no. 1, pp. 606–619, 2015.

[30] Z. Jiang, A. F. Molisch, G. Caire, and Z. Niu, "Achievable rates of FDD massive MIMO systems with spatial channel correlation," *IEEE Transactions on Wireless Communications*, vol. 14, no. 5, pp. 2868–2882, 2015.

[31] A. Sheikhi, S. M. Razavizadeh, and I. Lee, "A comparison of TDD and FDD massive MIMO systems against smart jamming," *IEEE Access*, vol. 8, pp. 72 068–72 077, 2020.

[32] J. Flordelis, F. Rusek, F. Tufvesson, E. G. Larsson, and O. Edfors, "Massive MIMO performance—TDD versus FDD: What do measurements say?" *IEEE Transactions on Wireless Communications*, vol. 17, no. 4, pp. 2247–2261, 2018.

[33] M. Jokinen, O. Kursu, N. Tervo, A. Pärssinen, and M. E. Leinonen, "Over-the-air phase calibration methods for 5G mmW antenna array transceivers," *IEEE Access*, vol. 12, pp. 28 057–28 070, 2024.

[34] X. Jiang et al., "A framework for over-the-air reciprocity calibration for TDD massive MIMO systems," *IEEE Transactions on Wireless Communications*, vol. 17, no. 9, pp. 5975–5990, 2018.

[35] B. M. Lee, "Calibration for channel reciprocity in industrial massive MIMO antenna systems," *IEEE Transactions on Industrial Informatics*, vol. 14, no. 1, pp. 221–230, 2018.

[36] J. Vieira, F. Rusek, and F. Tufvesson, "Reciprocity calibration methods for massive MIMO based on antenna coupling," in *2014 IEEE Global Communications Conference*, 2014, pp. 3708–3712.

[37] S. Hu, F. Rusek, and O. Edfors, "The potential of using large antenna arrays on intelligent surfaces," in *2017 IEEE 85th Vehicular Technology Conference (VTC Spring)*, 2017, pp. 1–6.

[38] C. Huang et al., "Holographic MIMO surfaces for 6g wireless networks: Opportunities, challenges, and trends," *IEEE Wireless Communications*, vol. 27, no. 5, pp. 118–125, 2020.

[39] A. Pereira, F. Rusek, M. Gomes, and R. Dinis, "Deployment strategies for large intelligent surfaces," *IEEE Access*, vol. 10, pp. 61 753–61 768, 2022.

[40] B. Razavi, *RF Microelectronics (2nd Edition) (Prentice Hall Communications Engineering and Emerging Technologies Series)*, 2nd. USA: Prentice Hall Press, 2011.

[41] U. Gustavsson et al., "On the impact of hardware impairments on massive MIMO," in *2014 IEEE Globecom Workshops (GC Wkshps)*, 2014, pp. 294–300.

[42] E. Björnson, J. Hoydis, M. Kountouris, and M. Debbah, "Massive MIMO systems with non-ideal hardware: Energy efficiency, estimation, and capacity limits," *IEEE Transactions on Information Theory*, vol. 60, no. 11, pp. 7112–7139, 2014.

[43] M. Wenk, "MIMO-OFDM-testbed: Challenges, implementations, and measurement results: Challenges, implementations, and measurement results," Ph.D. dissertation, ETH Zurich, 2010.

[44] C. Studer, M. Wenk, and A. Burg, "MIMO transmission with residual transmit-RF impairments," in *2010 International ITG Workshop on Smart Antennas (WSA)*, 2010, pp. 189–196.

[45] P. Zetterberg, "Experimental investigation of TDD reciprocity-based zero-forcing transmit precoding," *EURASIP Journal on Advances in Signal Processing*, vol. 2011, pp. 1–10, 2011.

[46] D. Morgan, Z. Ma, J. Kim, M. Zierdt, and J. Pastalan, "A generalized memory polynomial model for digital predistortion of RF power amplifiers," *IEEE Transactions on Signal Processing*, vol. 54, no. 10, pp. 3852–3860, 2006.

[47] S. Amin, P. N. Landin, P. Händel, and D. Rönnow, "Behavioral modeling and linearization of crosstalk and memory effects in RF MIMO transmitters," *IEEE Transactions on Microwave Theory and Techniques*, vol. 62, no. 4, pp. 810–823, 2014.

[48] D. Saffar, N. Boulejfen, F. M. Ghannouchi, A. Gharsallah, and M. Helaoui, "Behavioral modeling of MIMO nonlinear systems with multivariable polynomials," *IEEE Transactions on Microwave Theory and Techniques*, vol. 59, no. 11, pp. 2994–3003, 2011.

[49] J. Kim and K. Konstantinou, "Digital predistortion of wideband signals based on power amplifier model with memory," *Electronics Letters*, vol. 37, no. 23, p. 1, 2001.

[50] K. Muhonen, M. Kavehrad, and R. Krishnamoorthy, "Look-up table techniques for adaptive digital predistortion: A development and comparison," *IEEE Transactions on Vehicular Technology*, vol. 49, no. 5, pp. 1995–2002, 2000.

[51] A. Katz, J. Wood, and D. Chokola, "The evolution of PA linearization: From classic feedforward and feedback through analog and digital predistortion," *IEEE Microwave Magazine*, vol. 17, no. 2, pp. 32–40, 2016.

[52] C. Eun and E. Powers, "A new volterra predistorter based on the indirect learning architecture," *IEEE Transactions on Signal Processing*, vol. 45, no. 1, pp. 223–227, 1997.

[53] F. Mkadem and S. Boumaiza, "Physically inspired neural network model for RF power amplifier behavioral modeling and digital predistortion," *IEEE Transactions on Microwave Theory and Techniques*, vol. 59, no. 4, pp. 913–923, 2011.

[54] P. Jaraut, M. Rawat, and F. M. Ghannouchi, "Composite neural network digital predistortion model for joint mitigation of crosstalk, I/Q imbalance, nonlinearity in MIMO transmitters," *IEEE Transactions on Microwave Theory and Techniques*, vol. 66, no. 11, pp. 5011–5020, 2018.

[55] Y. Wu, U. Gustavsson, A. G. I. Amat, and H. Wymeersch, "Low complexity joint impairment mitigation of I/Q modulator and PA using neural networks," *IEEE Journal on Selected Areas in Communications*, vol. 40, no. 1, pp. 54–64, 2022.

[56] H. Hemesi, A. Abdipour, and A. Mohammadi, "Analytical modeling of MIMO-OFDM system in the presence of nonlinear power amplifier with memory," *IEEE Transactions on Communications*, vol. 61, no. 1, pp. 155–163, 2013.

[57] "Further elaboration on PA models for NR," *document 3GPP TSG-RAN WG4, R4-165901, Ericsson, Stockholm, Sweden*, Aug. 2016.

[58] A. Sheikhi, O. Edfors, and J. V. Alegría, "Over-the-air DPD and reciprocity calibration in massive MIMO and beyond," *IEEE Wireless Communications Letters*, pp. 1–1, Aug. 2025.

[59] Z. Liu, X. Hu, W. Wang, and F. M. Ghannouchi, "A joint PAPR reduction and digital predistortion based on real-valued neural networks for OFDM systems," *IEEE Transactions on Broadcasting*, vol. 68, no. 1, pp. 223–231, 2022.

[60] R. Zayani, H. Shaiek, and D. Roviras, "PAPR-aware massive MIMO-OFDM downlink," *IEEE Access*, vol. 7, pp. 25 474–25 484, 2019.

[61] J. Minkoff, "The role of AM-to-PM conversion in memoryless nonlinear systems," *IEEE Transactions on Communications*, vol. 33, no. 2, pp. 139–144, 2003.

[62] O. T. Demir and E. Björnson, "The Bussgang decomposition of nonlinear systems: Basic theory and MIMO extensions [lecture notes]," *IEEE Signal Processing Magazine*, vol. 38, no. 1, pp. 131–136, 2021.

[63] O. T. Demir and E. Björnson, "Channel estimation in massive MIMO under hardware non-linearities: Bayesian methods versus deep learning," *IEEE Open Journal of the Communications Society*, vol. 1, pp. 109–124, 2020.

[64] J. J. Bussgang, "Crosscorrelation functions of amplitude-distorted gaussian signals," 1952.

[65] X. Gao, O. Edfors, F. Tufvesson, and E. G. Larsson, "Massive MIMO in real propagation environments: Do all antennas contribute equally?" *IEEE Transactions on Communications*, vol. 63, no. 11, pp. 3917–3928, 2015.

[66] A. Sheikhi, F. Rusek, and O. Edfors, "Massive MIMO with per-antenna digital predistortion size optimization: Does it help?" In *ICC 2021 - IEEE International Conference on Communications*, 2021, pp. 1–6.

[67] A. Sheikhi and O. Edfors, "Machine learning based digital pre-distortion in massive MIMO systems: Complexity-performance trade-offs," in *2023 IEEE Wireless Communications and Networking Conference (WCNC)*, 2023, pp. 1–6.

[68] A. Sheikhi, J. V. Alegría, and O. Edfors, *Large intelligent surfaces with low-end receivers: From scaling to antenna and panel selection*, 2025. arXiv: `2411.04702 [eess.SP]`.

[69] A. Sheikhi, J. V. Alegría, and O. Edfors, "Hardware distortion modeling for panel selection in large intelligent surfaces," in *2024 58th Asilomar Conference on Signals, Systems, and Computers*, 2024, pp. 822–826.

Part II

Included Papers

Paper I

Massive MIMO with Per-Antenna Digital Predistortion Size Optimization: Does it Help?

In this paper, we study the effect of optimizing the per-antenna digital predistortion (DPD) sizes on the performance of the downlink massive MIMO system with residual hardware impairment. In particular, we first quantify the capacity after applying some per-antenna DPD with different numbers of coefficients at each antenna and then maximize the capacity by finding optimum values of the per-antenna DPD sizes under a constraint on the total number of DPD coefficients in the system. Two closed-form sub-optimal solutions are derived and numerical examples illustrate that their performance is very close to the optimal solution. It is shown that when the channel large-scale gains have high variation over the transmitter array, which is the case in practical scenarios, using our proposed optimized DPD sizes can improve the system capacity significantly. This allows us to scale down the massive MIMO system but still maintain performance. We also study the asymptotic behavior of the derived capacity and show that by using the optimized DPD sizes, the system performance can approach the asymptotic bound with a significantly smaller number of antennas.

1 Introduction

Massive multiple-input-multiple-output (MIMO) has emerged as a new technology to replace conventional multi-user MIMO systems in which the number of antennas at the base station (BS) scales up by one or more orders of magnitude [1]. This enhancement enables the system to exploit the spatial multiplexing and serve many user equipments (UEs) using the same time and frequency resources and improve the spectral efficiency by orders of magnitude. The success of massive MIMO technology to improve the system performance can be huge when fully digital beamforming is adopted at the BS, which requires one RF chain per antenna. When the number of antennas at the BS grows large, the digital beamforming complexity and RF chain power consumption also grow large which, in practice, limits the scaling [2], [3].

Massive MIMO is already commercialized and a significant number of prototypes and products labeled as massive MIMO are being produced. However, deploying a massive MIMO system with an arbitrarily large number of antennas introduces a lot of practical challenges to be resolved, which makes the achieved gains in the system performance by deploying massive MIMO to be far away from what theory suggests, mainly on the grounds of non-ideal effects of the hardware. There has been a body of work studying the effect of distortion caused by hardware impairment in massive MIMO systems. One of the main sources of distortion in a communication system is the non-linear behavior of amplifiers in the transceiver chains [4]. Digital predistortion (DPD) is widely known as an effective technique to mitigate the non-linear distortions in the output of amplifiers. In massive MIMO systems, due to the large number of antennas at the BS, adopting a MIMO DPD scheme results in high complexity and it will introduce a lot of challenges in the implementation [5]. Therefore, deploying per-antenna DPD is a more practical solution for massive MIMO. Being able to adjust the configuration and the DPD size, i.e. the number of DPD coefficients, can help the massive MIMO system to adapt to large-scale fluctuations in channel gains and signal power. Dynamic DPD model sizing is shown to be feasible with a low cost and many dynamic DPDs have been proposed in the literature, e.g. [6], [7], [8].

In this paper, we study the performance of the downlink massive MIMO system with non-ideal hardware when optimizing the per-antenna DPD sizes at the BS transmitter. Based on the measurements in realistic environments with implemented massive MIMO systems [9], we know that the contribution of each antenna to the system capacity is not equal and the large-scale variations have a high variation over the array. We also know that DPD power consumption grows linearly with total available number of coefficients [10]. Therefore, we propose to distribute the available DPD coefficients across the antennas based on their large-scale fading conditions to make sure that the antennas with more contribution to the system experience less hardware distortion.

We first select a model to characterize the residual impairment after applying the DPD with an arbitrary number of coefficients at each antenna in Section II and quantify the capacity by finding an upper bound in Section III. Then, we define an optimization problem in Section IV to maximize the capacity over the per-antenna DPD sizes which can be converted to a convex optimization problem and solved numerically with low complexity. Two sub-optimal closed-form solutions are also presented and the numerical results in Section VI show that the sub-optimal solutions deliver very close performance to the optimal numerical solutions. It is illustrated that a considerable gain in the capacity can be achieved by optimizing the per-antenna DPD sizes based on the channel gain variations compared to the case of using uniform DPD sizes. In Section V we do an asymptotic analysis to see how using optimized DPD the system capacity approaches its asymptotic bounds with a smaller number of antennas at the BS. Numerical results in Section VI verifies that adopting the optimized DPD sizes enables us to scale down the system significantly while still maintaining performance.

Throughout the paper, boldface uppercase, boldface lowercase, and italic letters, are used to denote matrices, vectors, and scalars, respectively. For a matrix $\boldsymbol{A}$, $\mathrm{tr}(\boldsymbol{A})$, $\boldsymbol{A}^T$, $\boldsymbol{A}^*$, and A_{ii} represent trace, transpose, conjugate, and the i'th element on the main diagonal of $\boldsymbol{A}$. We indicate circularly symmetric complex Gaussian random vectors with covariance matrix $\boldsymbol{C}$ as $\boldsymbol{a} \sim \mathcal{CN}(0, \boldsymbol{C})$ and the expectation of a random variable by $\mathbb{E}\{\cdot\}$. We denote a diagonal matrix with elements $a_1, ..., a_N$ on its main diagonal by $\mathrm{diag}\,(a_1, ..., a_N)$.

2 System and channel model

We consider the downlink of a massive MIMO system with an M-antenna BS serving a single-antenna UE in the presence of additive interference coming from other links and hardware distortion at both BS and UE sides. Although we have, for the sake of analytical clarity, focused on the performance of a single link under arbitrary interference conditions, the same methodology can be used for a multi-user scenario with inter-user interference at the cost of more complex derivations. The fading channel from the BS to the UE $\boldsymbol{h} \in \mathbb{C}^{M\times 1}$ changes independently in each coherence period according to a zero-mean complex Gaussian distribution $\boldsymbol{h} \sim \mathcal{CN}(0, \boldsymbol{R})$ with covariance matrix $\boldsymbol{R}$.

2.1 System Model

We consider the system model adopted in [11] where the received signal at the UE is modeled as

$$y = \boldsymbol{h}^T(\boldsymbol{s} + \boldsymbol{d}^{\mathrm{BS}}) + d^{\mathrm{UE}} + n_{\mathrm{interf}} + n_{\mathrm{noise}}. \tag{1}$$

where $\boldsymbol{s}$ is the transmitted signal from the BS after precoding, with covariance matrix $\boldsymbol{W}$ and the average power $\mathrm{tr}(\boldsymbol{W}) = \mathrm{P}_T$. The additive distortion resulting from BS and UE non-ideal hardware are denoted by $\boldsymbol{d}^{\mathrm{BS}}$ and d^{UE}, respectively, which are characterized in the next section. The interference from other transmissions is denoted by n_{interf} and $n_{\mathrm{noise}} \sim \mathcal{CN}(0, \sigma^2)$ models the additive noise at the UE receiver.

2.2 Hardware Impairment Model

We assume a fully digital system where each antenna is connected to an RF chain with non-ideal hardware components and a DPD block with n_m^{DPD} coefficients is paired with the m'th antenna RF chain. The UE is also assumed to have non-ideal hardware in its receiver. It is known by experimental verification that the distortion level at the output of each RF chain is proportional to the signal power at input of this RF chain [12], [13]. The proportionality factor for the m'th RF chain distortion power which can also be interpreted as the level of residual impairment is denoted by κ_m^{BS}. The residual hardware impairment proportionality factor at the UE receiver is also denoted by κ^{UE}. The distribution of additive hardware distortion terms $\boldsymbol{d}^{\mathrm{BS}}$ and d^{UE} are also known both theoretically and through experiments to be $\boldsymbol{d}^{\mathrm{BS}} \sim \mathcal{CN}(0, \boldsymbol{Q}^{\mathrm{BS}})$ and $d^{\mathrm{UE}} \sim \mathcal{CN}(0, q^{\mathrm{UE}})$ in each channel coherence period [13].

The level of residual impairment in each RF chain depends on the performance of its corresponding DPD block. It has been shown by experiments on power amplifiers that the performance of the DPD block in terms of removing the distortion is in the form of a decreasing homographic function of the number of the DPD coefficients [14], which also agrees with intuition as we know that there is a decreasing gain from adding more coefficients to the DPD after applying a DPD with a certain number of coefficients. Therefore, we assume the following model for evaluating the level of residual impairment in each RF chain after applying the DPD

$$\kappa_m^{\mathrm{BS}} = \frac{\kappa^{\mathrm{BS}}}{n_m^{\mathrm{DPD}}}, \tag{2}$$

where κ^{BS} is a constant which represents the basic hardware impairment level in each RF chain when there is no DPD or a reference-level DPD on each antenna RF chain. This constant depends on the DPD architecture and characteristics

of the deployed hardware such as the non-linearity of power amplifiers and can be found through similar measurements as in [14].

By exploiting the above models and definitions, for a given signal covariance matrix $\boldsymbol{W}$ and channel vector $\boldsymbol{h}$, the additive distortion distributions after performing per antenna DPD at the BS are characterized by

$$\boldsymbol{Q}^{\mathrm{BS}} = \kappa^{\mathrm{BS}} \mathrm{diag}\left(\frac{W_{11}}{n_1^{\mathrm{DPD}}}, ..., \frac{W_{MM}}{n_M^{\mathrm{DPD}}}\right), \tag{3}$$

and

$$q^{\mathrm{UE}} = \kappa^{\mathrm{UE}} \boldsymbol{h}^T \boldsymbol{W} \boldsymbol{h}^*. \tag{4}$$

In the next section, we find the downlink capacity of the system under the above hardware impairment model with given fixed per-antenna DPD sizes $\left\{n_1^{\mathrm{DPD}}, ..., n_M^{\mathrm{DPD}}\right\}$.

3 Downlink Capacity with per-antenna DPD

To characterize the system capacity with the hardware impairment model and per antenna DPD sizes introduced in the previous section, we can exploit the upper bounding technique adopted in [11], where by assuming perfect interference cancellation, and perfect channel state information at the BS and the UE, an upper bound on the downlink channel capacity can be found as

$$C^{\mathrm{UB}} = \log_2\left(1 + \frac{G^{\mathrm{DL}}}{1 + \kappa^{\mathrm{UE}} G^{\mathrm{DL}}}\right), \tag{5}$$

where

$$G^{\mathrm{DL}} = \sum_{m=1}^{M} \mathbb{E}\left[\frac{|h_m|^2}{\frac{\kappa^{\mathrm{BS}}|h_m|^2}{n_m^{\mathrm{DPD}}} + \frac{\sigma^2}{P_T}}\right]. \tag{6}$$

By exploiting the techniques introduced in appendices A and C of [11], for a given channel distribution $\boldsymbol{h} \sim CN(0, \boldsymbol{R})$, the BS distortion related term G^{DL} in the capacity upper bound can be computed as

$$G^{\mathrm{DL}} = \frac{1}{\kappa^{\mathrm{BS}}} \sum_{m=1}^{M} n_m^{\mathrm{DPD}} \left[1 - \tau_m e^{\tau_m} E_1(\tau_m)\right], \tag{7}$$

where $\tau_m = \frac{\sigma^2 n_m^{\mathrm{DPD}}}{\kappa^{\mathrm{BS}} P_T R_{mm}}$ and $E_1(x) = \int_1^\infty \frac{e^{-tx}}{t} dt$ is the exponential integral. In the next section, we are interested in maximizing this capacity upper bound to

find the optimum values of n_m^{DPD}.

Due to the exponential integral in $\boldsymbol{G}^{\mathrm{DL}}$, it is not easy to maximize the capacity in the current form. Therefore, we use the logarithmic approximation for the exponential integral [15] and find a new upper bound

$$\tilde{C}^{\mathrm{UB}} = \log_2 \left(1 + \frac{\tilde{G}^{\mathrm{DL}}}{1 + \kappa^{\mathrm{UE}} \tilde{G}^{\mathrm{DL}}} \right), \tag{8}$$

where

$$\tilde{G}^{\mathrm{DL}} = \frac{1}{\kappa^{\mathrm{BS}}} \sum_{m=1}^{M} n_m^{\mathrm{DPD}} \left[1 - \frac{1}{2} \tau_m \ln(1 + \frac{2}{\tau_m}) \right]. \tag{9}$$

The capacity upper bound in (8) is adopted in the next section to optimize the per-antenna DPD size at the BS. Numerical results show that using $\tilde{C}^{\mathrm{UB}}$ instead of C^{UB} for optimization and capacity evaluation, gives very close results and $\tilde{C}^{\mathrm{UB}}$ is an appropriate bound for our purpose.

4 per-antenna DPD size Optimization

It has been shown that in a massive MIMO system, the contribution of each antenna to the system performance has a huge variation over the array and only a portion of the antennas with stronger large-scale fading in their channels determines the system performance. Measurements in realistic environments with implemented massive MIMO systems have verified that even in wide-band multi-user scenarios, this property holds [9]. In a fully digital system, there is one RF chain per antenna, which demands a high power consumption in the analog front ends if all the RF chains have to meet the demanded linearity constraints. On the other hand, performing a DPD with the same number of coefficients on each RF chain to mitigate the non-linearity distortion, which is usually designed for the worst-case scenarios, also results in a huge leap in the digital circuit power consumption. Therefore, in order to increase the energy efficiency and reduce power consumption, we propose to adapt the level of RF chains non-linearity distortion to the channel gain variations by optimizing their corresponding number of DPD coefficients.

To quantify the achievable gain by performing this adaptation, we assume that there is a limited number of maximum DPD coefficients $n_{\max}^{\mathrm{DPD}}$, that can be used by the RF chains in the system. This number can also be interpreted as a power constraint as it is shown that the DPD power consumption grows linearly with the number of DPD coefficients [10]. By leveraging the derived upper bound in (8) and given the facts that log(.) is an increasing concave function and $\frac{\tilde{G}^{\mathrm{DL}}}{1+\kappa^{\mathrm{UE}}\tilde{G}^{\mathrm{DL}}}$ is an increasing function of $\tilde{G}^{\mathrm{DL}}$, we define the optimization

problem

$$\begin{aligned} \max_{n_m^{\mathrm{DPD}}} \ & \frac{1}{\kappa^{\mathrm{BS}}} \sum_{m=1}^{M} n_m^{\mathrm{DPD}} \left[1 - \frac{1}{2}\tau_m \ln(1 + \frac{2}{\tau_m})\right] \\ \text{s.t.} \ & n_m^{\mathrm{DPD}} \geq 1 \qquad m = 1, 2, ..., M \\ & \sum_{m=1}^{M} n_m^{\mathrm{DPD}} \leq n_{\max}^{\mathrm{DPD}} \\ & n_m^{\mathrm{DPD}} \in \mathbb{N} \qquad m = 1, 2, ..., M \end{aligned} \tag{10}$$

to optimize the per-antenna DPD sizes n_m^{DPD}. The objective function of this problem is a concave function of $\left\{n_1^{\mathrm{DPD}}, ..., n_M^{\mathrm{DPD}}\right\}$. Also the first and second constraints include convex and affine functions of $\left\{n_1^{\mathrm{DPD}}, ..., n_M^{\mathrm{DPD}}\right\}$. However, the last constraint makes the problem infeasible to solve in the current form. One way to deal with this optimization problem is to relax this constraint and find the non-integer solutions, and round them up to the closest integer at the end. By using this technique, the relaxed optimization problem is now a standard convex one [16] and can be solved efficiently using available numerical tools, e.g. CVX [17]. In the following subsections, we introduce two sub-optimal solutions in closed form.

4.1 Sub-optimal Solution I: max-SNDR

In this subsection, we propose a sub-optimal solution for n_m^{DPD} in a closed form. For this purpose, instead of maximizing the BS distortion related term G^{DL}, we maximize the summation of each BS antenna contribution in received signal to-noise-plus-distortion-ratio (SNDR) as

$$\begin{aligned} \max_{n_m^{\mathrm{DPD}}} \ & \sum_{m=1}^{M} \frac{R_{mm}}{\frac{\kappa^{\mathrm{BS}} R_{mm}}{n_m^{\mathrm{DPD}}} + \frac{\sigma^2}{P_T}} \\ \text{s.t.} \ & n_m^{\mathrm{DPD}} \geq 1 \qquad m = 1, 2, ..., M \\ & \sum_{m=1}^{M} n_m^{\mathrm{DPD}} \leq n_{\max}^{\mathrm{DPD}} \end{aligned} \tag{11}$$

This optimization problem is also convex can be solved by leveraging the KKT conditions [16] for the optimal solution. The following lemma gives the solution to this problem.

Lemma 1 *The optimal value* $\hat{n}_m^{\mathrm{DPD}}$ *for the above optimization problem satisfies*

$$\hat{n}_m^{\mathrm{DPD}} = \max\left\{1, \left\lceil R_{mm}\frac{-\kappa^{\mathrm{BS}}\sqrt{\nu} \pm \sqrt{\kappa^{\mathrm{BS}}}}{\sqrt{\nu}\frac{\sigma^2}{P_T}}\right\rceil\right\}, \tag{12}$$

and

$$\sum_{m=1}^{M} \max\left\{1, \left\lceil R_{mm}\frac{-\kappa^{\mathrm{BS}}\sqrt{\nu} \pm \sqrt{\kappa^{\mathrm{BS}}}}{\sqrt{\nu}\frac{\sigma^2}{P_T}}\right\rceil\right\} \leq n_{\max}^{\mathrm{DPD}}, \tag{13}$$

where ν *is the Lagrangian multiplier for the equality constraint. A simple closed form solution can be found for a large enough* $n_{\max}^{\mathrm{DPD}}$ *as*

$$\hat{n}_m^{\mathrm{DPD}} = \left\lceil \frac{R_{mm}}{\sum_{m=1}^{M} R_{mm}} n_{\max}^{\mathrm{DPD}} \right\rceil. \tag{14}$$

Proof *By formulating the KKT conditions for the above problem and solving for the inequality Lagrangian constraints, one can derive* (12) *and* (13)*. For a large enough* $n_{\max}^{\mathrm{DPD}}$ *even the antennas with weakest channel gain will have* $\hat{n}_m^{\mathrm{DPD}} > 1$ *which results in* (14) *after solving* (12) *and* (13) *under this condition.* □

4.2 Sub-optimal Solution II: min-Distortion

Another sub-optimal solution can be found analytically by minimizing the summation of each BS antenna contribution to the distortion power at the UE by solving the optimization problem

$$\begin{aligned} \min_{n_m^{\mathrm{DPD}}} \quad & \sum_{m=1}^{M} \frac{R_{mm}}{n_m^{\mathrm{DPD}}} \\ \text{s.t.} \quad & n_m^{\mathrm{DPD}} \geq 1 \qquad m = 1, 2, ..., M \\ & \sum_{m=1}^{M} n_m^{\mathrm{DPD}} \leq n_{\max}^{\mathrm{DPD}} \end{aligned} \tag{15}$$

This problem is convex as well can be solved using the following lemma.

Lemma 2 *The optimal value* $\hat{n}_m^{\mathrm{DPD}}$ *for the above optimization problem satisfies*

$$\hat{n}_m^{\mathrm{DPD}} = \max\left\{1, \left\lceil \sqrt{\frac{R_{mm}}{\nu}} \right\rceil\right\}, \tag{16}$$

and

$$\sum_{m=1}^{M} \max\left\{1, \left\lceil \sqrt{\frac{R_{mm}}{\nu}} \right\rceil \right\} \leq n_{\max}^{\mathrm{DPD}}, \tag{17}$$

where ν is the Lagrangian multiplier for the equality constraint. A simple closed form solution can be found for a large enough $n_{\max}^{\mathrm{DPD}}$ as

$$\hat{n}_m^{\mathrm{DPD}} = \left\lceil \frac{\sqrt{R_{mm}}}{\sum_{m=1}^{M} \sqrt{R_{mm}}} n_{\max}^{\mathrm{DPD}} \right\rceil. \tag{18}$$

Proof *Similar to the previous Lemma we can formulate the KKT conditions for and solve for the inequality Lagrangian constraints to derive* (16) *and* (17). *Also for the same reason as in previous Lemma, when $n_{\max}^{\mathrm{DPD}}$ is large enough, we have $\hat{n}_m^{\mathrm{DPD}} > 1$ which results in* (18). □

Simulation results illustrate that by using the above sub-optimal solutions for adjusting the per-antenna DPD size, the achieved performance is very close to the optimal solutions of (10). In the next section, we analyze the asymptotic behavior of the capacity when the proposed optimized DPD size selection is adopted at the BS.

5 Asymptotic Analysis

In this section, we analyze the system performance in the asymptotic bounds of very large number of antennas and very high SNR. By considering the capacity upper bound in (5), it can be seen that

$$\lim_{P_T \to +\infty} C^{\mathrm{UB}} = \log_2\left(1 + \frac{n_{\mathrm{avg}}^{\mathrm{DPD}} M}{\kappa^{\mathrm{BS}} + \kappa^{\mathrm{UE}} n_{\mathrm{avg}}^{\mathrm{DPD}} M}\right), \tag{19}$$

and

$$\lim_{M \to +\infty} C^{\mathrm{UB}} = \log_2\left(1 + \frac{1}{\kappa^{\mathrm{UE}}}\right), \tag{20}$$

where $n_{\mathrm{avg}}^{\mathrm{DPD}} = \frac{\sum_{m=1}^{M} n_m^{\mathrm{DPD}}}{M}$ is the average size of the per-antenna DPD. As we see, these bounds are independent of how the DPD coefficients are distribute across antennas. However, we show that optimizing the per-antenna DPD size can cause the capacity to approach the asymptotic bound much faster, i.e. for a smaller number of antennas. We are interested to find the minimum number

of antennas to achieve a certain fraction of the asymptotic bound when using optimized DPD size selection and compare it to the uniform size selection case.

The dependency of the capacity on M arises from G^{DL}. Therefore, we consider the ratio $\frac{G^{\mathrm{DL}}}{1+\kappa^{\mathrm{UE}}G^{\mathrm{DL}}}$ as the performance metric which means that the asymptotic bound of the performance is $\frac{1}{\kappa^{\mathrm{UE}}}$. We try to find the minimum number of antennas so that $\frac{G^{\mathrm{DL}}}{1+\kappa^{\mathrm{UE}}G^{\mathrm{DL}}} = \frac{\beta}{\kappa^{\mathrm{UE}}}$ where $0 \leq \beta \leq 1$. In order to be able to compare the asymptotic behavior of the uniform and optimized DPD size selections analytically, we use SNDR approximation which was also used for the first sub-optimal DPD size optimization. As it is stated in the previous section, and it is verified in the numerical results, such an approximation has a very close performance compared to the case of adopting the exact value of G^{DL}.

By selecting the max-SNDR as the optimal DPD size selection and $n_m^{\mathrm{DPD}} = \lceil \frac{n_{\max}^{\mathrm{DPD}}}{M} \rceil$ as the uniform DPD size selection, the minimum number of antennas, $M_{\min}^{\mathrm{opt}}$ and $M_{\min}^{\mathrm{uni}}$ to have $\frac{G^{\mathrm{DL}}}{1+\kappa^{\mathrm{UE}}G^{\mathrm{DL}}} = \frac{\beta}{\kappa^{\mathrm{UE}}}$, for the optimal and uniform cases, respectively, can be calculated as follows. To make the results easier to interpret, we assume that the channel large-scale gain from each antenna to the UE has two possible levels, $R_{mm} = R_s$ for $\lceil \gamma M \rceil$ antennas, where $0 < \gamma < 1$, and $R_{mm} = R_w$ for the others. Under these conditions, we have:

$$M_{\min}^{\mathrm{opt}} = \left\lceil \frac{\frac{\beta}{\kappa^{\mathrm{UE}}(1-\beta)}}{\frac{n_{\mathrm{avg}}^{\mathrm{DPD}}(\gamma R_s+(1-\gamma)R_w)}{\kappa^{\mathrm{BS}}(\gamma R_s+(1-\gamma)R_w)+n_{\mathrm{avg}}^{\mathrm{DPD}}\frac{\sigma^2}{P_T}}} \right\rceil \tag{21}$$

and

$$M_{\min}^{\mathrm{uni}} = \left\lceil \frac{\frac{\beta}{\kappa^{\mathrm{UE}}(1-\beta)}}{\frac{n_{\mathrm{avg}}^{\mathrm{DPD}}\gamma R_s}{\kappa^{\mathrm{BS}}R_s+n_{\mathrm{avg}}^{\mathrm{DPD}}\frac{\sigma^2}{P_T}} + \frac{n_{\mathrm{avg}}^{\mathrm{DPD}}(1-\gamma)R_w}{\kappa^{\mathrm{BS}}R_w+n_{\mathrm{avg}}^{\mathrm{DPD}}\frac{\sigma^2}{P_T}}} \right\rceil . \tag{22}$$

In the next section, we illustrate by numerical examples that $M_{\min}^{\mathrm{opt}}$ is significantly smaller than $M_{\min}^{\mathrm{uni}}$, which implies that by adopting the optimized DPD size selection, the system performance can approach the asymptotic bounds much faster, and by leveraging this effect, we can reduce the number of antennas and still get the same performance.

6 Numerical Results

In this section, the performance of the proposed DPD size optimizations is studied and the possible gains in the downlink spectral efficiency by adjusting

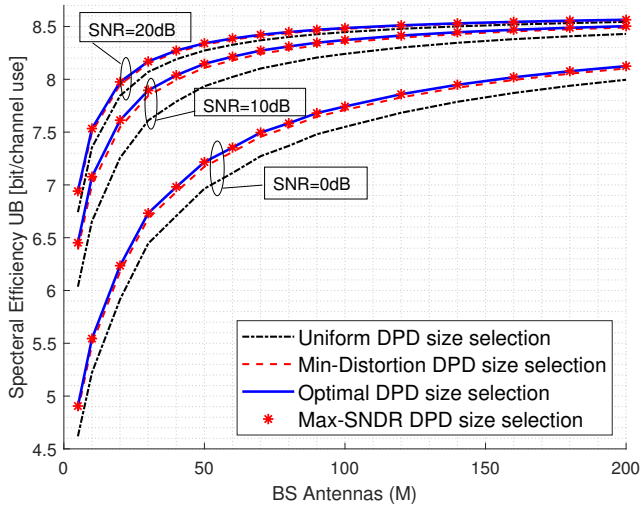

Figure 1: Spectral efficiency vs number of BS antennas for different values of SNR when $n_{\text{avg}}^{\text{DPD}} = 20$, $R_s = 10$, and $R_w = 1$.

the per-antenna DPD size is illustrated for different scenarios. We assume that the channel large-scale gain from each antenna to the UE has two possible levels, $R_{mm} = R_s$ for $\lceil \gamma M \rceil$ antennas, where $\gamma = 0.20$, and $R_{mm} = R_w$ for the others. The basic hardware distortion factor before applying DPD at the BS is $\kappa^{\text{BS}} = 0.5$ and for UE $\kappa^{\text{UE}} = 0.05^2$. CVX [17] is used to solve convex optimization problems numerically when needed.

Fig. 1 compares the downlink spectral efficiency of the system when adopting different DPD size selection strategies. As it can be seen from the figure, the max-SNDR and min-distortion sub-optimal solutions performance is very close to the optimal solution. Also, we can see a significant improvement in SE compared to the uniform DPD size selection case, which implies that in a massive MIMO system with fairly large number of antennas, we can mitigate the distortion more efficiently by adopting our proposed solutions. The performance gain reduces in very high SNR scenarios and when the number of BS antennas is very large.

Fig. 2 illustrates the downlink spectral efficiency of the system when adopting different DPD size selection strategies with changing the available number of DPD coefficients. We can see that for small to fairly large number of DPD size, adopting the optimal DPD size selection can improve the performance of the system significantly for both small and large number of antennas.

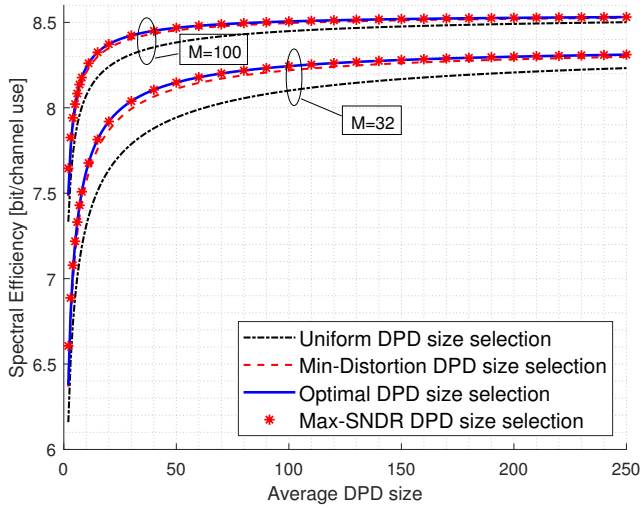

Figure 2: Spectral Efficiency vs average DPD size for different number of BS antennas when SNR $= 10dB$, $R_s = 10$ and $R_w = 1$.

In order to see the effect of variations in antennas channel large-scale gain, Fig. 3 shows the downlink spectral efficiency of the system for different ratios between the strong and week channels defined as $r = \frac{R_s}{R_w}$. As it can be seen from the figure, the capacity improvement relies significantly on the channel gain variation. Exploiting this channel gain variation by adopting the optimal DPD size selection can make a huge impact on the performance. For example, if the channel gain variation is high and the optimal size selection is adopted, the spectral efficiency for $M = 64$ antennas with DPD size optimization can approach the case with $M = 128$ antennas without the DPD size optimization.

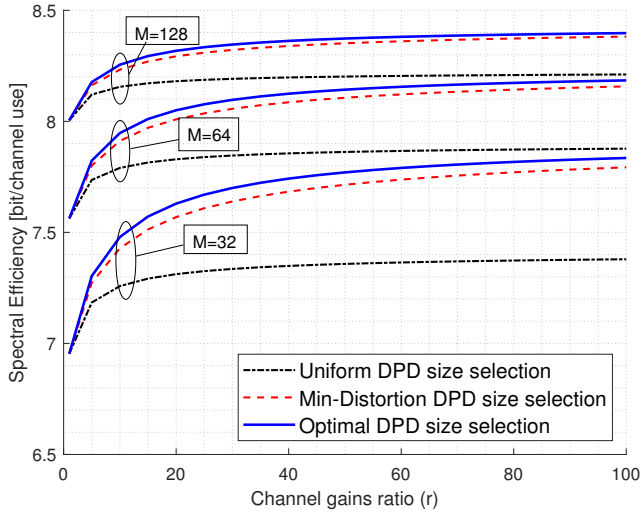

Figure 3: Spectral Efficiency vs the channel gains ratio ($r = \frac{R_s}{R_w}$) for different number of antennas when SNR $= 10dB$ and $n_{\text{avg}}^{\text{DPD}} = 20$

Fig. 4 illustrates the spectra efficiency with the proposed optimal DPD size selection when the basic hardware impairment level $\kappa^{\text{BS}} = 0.5$ increases from 0 to 100%. The reference lines illustrate the spectral efficiency when uniform DPD size selection is used and κ^{BS} is fixed at 0.5. Interestingly, when using the DPD size optimization, we can increase the basic distortion level around 40% depending on the number of antennas and still maintain performance which enables massive MIMO to be deployed using cheaper hardware without a significant loss in performance.

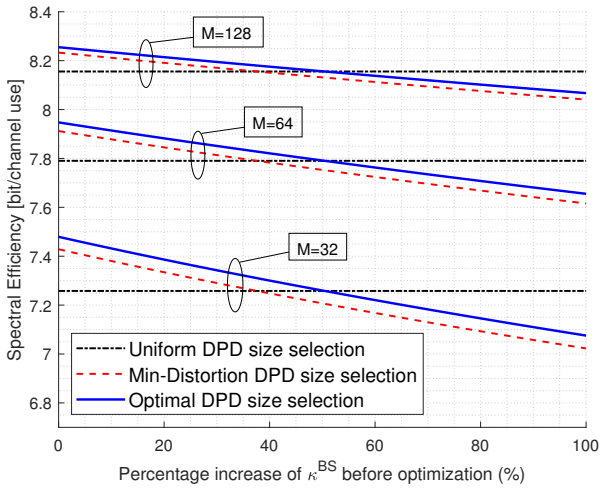

Figure 4: Spectral Efficiency vs the percentage increase of the basic impairment level κ^{BS} for different number of BS antennas when SNR $= 10dB$, $n_{\mathrm{avg}}^{\mathrm{DPD}} = 20$, $R_s = 10$, and $R_w = 1$.

To illustrate the asymptotic behavior of capacity which was discussed in Section V, Fig. 5 illustrates the percentage decrease in $M_{\mathrm{min}}^{\mathrm{opt}}$ compared to $M_{\mathrm{min}}^{\mathrm{uni}}$ for $\beta = 0.9$, which basically shows the available room for scaling down the system and still achieve 90% of the asymptotic performance by adopting the proposed DPD size selection. As it can be seen from the figures, for average values of channel gain variation, moderate SNR values, fairly small κ^{BS}, and fairly large average DPD size, the system can scale down by 20% and even 30% in some cases.

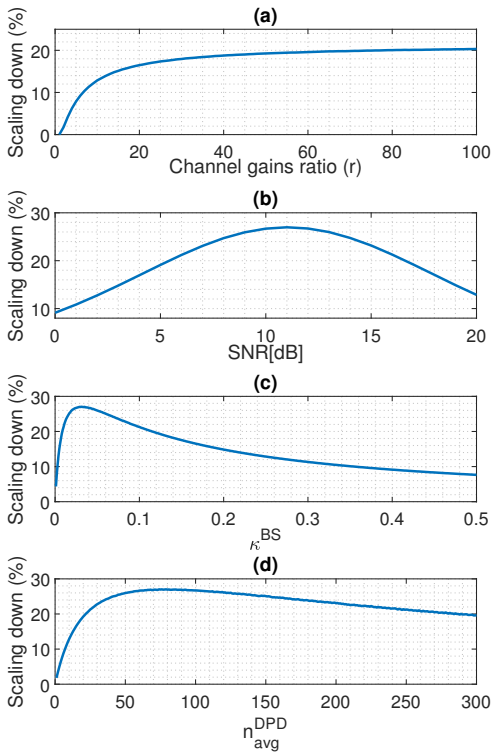

Figure 5: Possible Scaling down in the number of antennas to achieve 90% of the asymptotic performance. (a): SNR $= 20dB$ and $n_{\text{avg}}^{\text{DPD}} = 10$. (b): $n_{\text{avg}}^{\text{DPD}} = 10$, $R_s = 10$, and $R_w = 1$. (c): SNR $= 20dB$, $n_{\text{avg}}^{\text{DPD}} = 10$, $R_s = 10$, and $R_w = 1$. (d) SNR $= 20dB$, $R_s = 10$, and $R_w = 1$.

7 Conclusion

In this paper, we show that as the contribution of the antennas is not the same in massive MIMO systems, one can improve the system performance by optimizing the number of coefficients used in the per-antenna DPD based on the channel gain variations over the array. We quantify the capacity for given DPD sizes and maximize it by finding the optimal DPD sizes with convex optimization and two sub-optimal solutions. Numerical results show that when there is a high variation in large-scale gains over the array which is the case in practical scenarios, by adopting the optimized DPD sizes the massive MIMO performance can be improved significantly compared to a uniform size selection

scenario. We also study the asymptotic bound on the performance and show that if one adopts the optimized DPD sizes, the capacity can approach the asymptotic value with a smaller number of antennas, which enables us to reduce the system cost and still maintain performance.

References

[1] E. G. Larsson, O. Edfors, F. Tufvesson, and T. L. Marzetta, "Massive MIMO for next generation wireless systems," *IEEE Communications Magazine*, vol. 52, no. 2, pp. 186–195, 2014.

[2] F. Rusek et al., "Scaling up MIMO: Opportunities and challenges with very large arrays," *IEEE Signal Processing Magazine*, vol. 30, no. 1, pp. 40–60, 2013.

[3] J. Zhang, E. Björnson, M. Matthaiou, D. W. K. Ng, H. Yang, and D. J. Love, "Prospective multiple antenna technologies for beyond 5G," *IEEE Journal on Selected Areas in Communications*, vol. 38, no. 8, pp. 1637–1660, 2020.

[4] B. Razavi, *RF Microelectronics (2nd Edition) (Prentice Hall Communications Engineering and Emerging Technologies Series)*, 2nd. USA: Prentice Hall Press, 2011.

[5] K. Hausmair, P. N. Landin, U. Gustavsson, C. Fager, and T. Eriksson, "Digital predistortion for multi-antenna transmitters affected by antenna crosstalk," *IEEE Transactions on Microwave Theory and Techniques*, vol. 66, no. 3, pp. 1524–1535, 2018.

[6] Y. Li and A. Zhu, "On-demand real-time optimizable dynamic model sizing for digital predistortion of broadband RF power amplifiers," *IEEE Transactions on Microwave Theory and Techniques*, vol. 68, no. 7, pp. 2891–2901, 2020.

[7] C. Crespo-Cadenas, M. J. Madero-Ayora, J. Reina-Tosina, and J. A. Becerra-González, "Transmitter linearization adaptable to power-varying operation," *IEEE Transactions on Microwave Theory and Techniques*, vol. 65, no. 10, pp. 3624–3632, 2017.

[8] Y. Guo, C. Yu, and A. Zhu, "Power adaptive digital predistortion for wideband RF power amplifiers with dynamic power transmission," *IEEE Transactions on Microwave Theory and Techniques*, vol. 63, no. 11, pp. 3595–3607, 2015.

[9] X. Gao, O. Edfors, F. Tufvesson, and E. G. Larsson, "Massive MIMO in real propagation environments: Do all antennas contribute equally?" *IEEE Transactions on Communications*, vol. 63, no. 11, pp. 3917–3928, 2015.

[10] J. Wood, "System-level design considerations for digital pre-distortion of wireless base station transmitters," *IEEE Transactions on Microwave Theory and Techniques*, vol. 65, no. 5, pp. 1880–1890, 2017.

[11] E. Björnson, J. Hoydis, M. Kountouris, and M. Debbah, "Massive MIMO systems with non-ideal hardware: Energy efficiency, estimation, and capacity limits," *IEEE Transactions on Information Theory*, vol. 60, no. 11, pp. 7112–7139, 2014.

[12] C. Studer, M. Wenk, and A. Burg, "MIMO transmission with residual transmit-RF impairments," in *2010 International ITG Workshop on Smart Antennas (WSA)*, 2010, pp. 189–196.

[13] M. Wenk, "MIMO-OFDM-testbed: Challenges, implementations, and measurement results: Challenges, implementations, and measurement results," Ph.D. dissertation, ETH Zurich, 2010.

[14] S. Wang, M. Roger, J. Sarrazin, and C. Lelandais-Perrault, "An efficient method to study the tradeoff between power amplifier efficiency and digital predistortion complexity," *IEEE Microwave and Wireless Components Letters*, vol. 29, no. 11, pp. 741–744, 2019.

[15] M. Abramowitz, I. A. Stegun, and R. H. Romer, *Handbook of mathematical functions with formulas, graphs, and mathematical tables*, 1988.

[16] S. Boyd, S. P. Boyd, and L. Vandenberghe, *Convex optimization*. Cambridge university press, 2004.

[17] M. Grant and S. Boyd, *CVX: Matlab software for disciplined convex programming, version 2.1*, `http://cvxr.com/cvx`, Mar. 2014.

Paper II

Machine Learning Based Digital Pre-Distortion in Massive MIMO Systems: Complexity-Performance Trade-offs

In this paper, we study the trade-off between complexity and performance in massive MIMO systems with NN-DPD blocks at the base station. In particular, we consider a multi-user massive MIMO system with per-antenna NN-DPDs, each with an adjustable NN architecture in terms of the size and the number of NN hidden layers. We first analyze the system performance in terms of compensation of the non-linear hardware distortion for different levels of NN-DPD complexity and the number of antennas. We illustrate the required level of complexity in the trained NN-DPD blocks to approach the performance of an ideal conventional DPD. The statistics of the signal to interference and noise plus distortion ratio for a randomly located UE are selected as the performance metrics. We then assume a limited total digital computation power to be allocated among the NN-DPD blocks and propose to select the NN-DPD architecture of each TX branch based on the channel conditions of its corresponding antenna. To illustrate the importance of such a smart DPD resource allocation, we have analyzed the performance of a massive MIMO system with different NN-DPD architecture selection strategies. Numerical results indicate that by adopting the smart NN-DPD resource allocation, a significant boost in the system performance can be achieved, making room for reducing the overall system cost when scaling a massive MIMO system.

Ashkan Sheikhi and Ove Edfors
"Machine Learning Based Digital Pre-Distortion in Massive MIMO Systems: Complexity-Performance Trade-offs,"
in *2023 IEEE Wireless Communications and Networking Conference (WCNC)*, Glasgow, United Kingdom, 2023, pp. 1-6.

1 Introduction

MIMO communications with large antenna arrays, widely known as massive MIMO, has secured its place as one of the main physical layer technologies in the fifth generation (5G) and future wireless communications networks. It has been proven in both theory and practice that massive MIMO can provide a significant capacity boost in the communication network, which helps the system designers and the operators to meet the network requirements in 5G and beyond applications. Although in theory a massive MIMO system with arbitrarily large arrays suggests huge gains in system capacity, implementation challenges and system power consumption are important limiting factors to achieve such gains in commercial deployments of massive MIMO systems [1], [2], [3].

Implementing a massive MIMO system in practice introduces non-ideal hardware-related effects, commonly known as hardware impairments, which can significantly affect the overall performance of the system. For example, hardware impairment sources such as non-linear amplifiers and low-resolution analogue to digital converters (ADCs) can hinder the massive MIMO capacity to grow arbitrarily with increasing the number of antennas [4]. On the other hand, deploying a fully digital massive MIMO system with with fairly high-quality hardware components can increase the total system costs drastically, which is not favorable for commercial deployments of massive MIMO in 5G and beyond. Non-linearity in analogue fronts ends (AFEs), has been shown to be one of the main limiting hardware impairment sources in designing transceivers for a communication system [5]. It has been shown that pushing the AFEs requirements toward the linear ideal case can result in a significant leap in the system power consumption [6], which is not favorable from the cost efficiency point of view. Digital pre-distortion (DPD) is widely known as a practical method to compensate the non-linearity effects in transceivers, enabling the system designer to relax the linearity requirements of the analogue hardware components [7], [8], [9], [10]. Although this can reduce the power consumption of the AFE by relaxing its linearity requirements, the DPD itself can consume a significant share of the system power budget depending on the DPD design complexity and performance requirements.

DPDs are mainly designed based on the Volterra series and memory polynomial models. Another class of DPDs, gaining more interest in recent years due to the new wave of machine learning applications, is the neural-network based DPDs (NN-DPDs). It has been shown that a well-designed and well-trained NN-DPD can outperform the conventional DPDs at the same level of complexity and power consumption [11], [12], [13]. Most of the works in this regard are focusing on designing a novel low-complexity design of an NN-DPD for a single transceiver chain.

In this paper, we study the trade-off between complexity and performance

of per-antenna NN-DPDs in a massive MIMO system. In particular, we analyze the massive MIMO system performance in terms of compensation of the non-linear hardware distortion for different levels of NN-DPD complexity and the number of antennas. We exploit this analysis to illustrate the minimum level of complexity in the trained NN-DPD blocks to approach the performance of an ideal DPD. In [14] the authors have illustrated the advantages of optimizing the number of coefficients in conventional per-antenna DPDs for a massive MIMO systems. The main reasoning behind the importance of such optimization is the significant variance of antennas contribution in a massive MIMO array which has been verified by measurement setups [15]. Therefore, we define a problem of selecting the complexity of each per-antenna NN-DPD in a massive MIMO system, under limited computation power allocated for DPD, and show that how selecting the NN-DPDs complexity based on the average fading conditions of the antennas can benefit the system level performance metrics such as the signal to interference and noise plus distortion ratio (SINDR) at the user equipments (UEs) side. In particular, such smart selection will allow the system designer to reduce the overall DPD block complexity and power consumption while maintaining the same level of performance. On the other hand, having a more energy efficient DPD can make room for selecting more non-linear and cheaper hardware blocks in the AFEs, which is favorable for the scaling of massive MIMO system in 5G and beyond networks. In summary, the contributions of this paper are as followed:

- We have designed a per-antenna NN-DPD architecture for massive MIMO systems which enables us to analyze the relationship between NN-DPDs complexity and the performance of a multiple-user massive MIMO system in terms of SINDR.
- We have shown the potentials of selecting per-antenna NN-DPDs complexity based on the channel conditions of the corresponding antennas in a massive MIMO system where antennas contributions are not equal along the array.

Throughout the paper, boldface uppercase, boldface lowercase, and italic letters, are used to denote matrices, vectors, and scalars, respectively. For a matrix $\boldsymbol{A}$, $\mathrm{tr}(\boldsymbol{A})$, $\boldsymbol{A}^H$,$\boldsymbol{A}^T$, $\boldsymbol{A}^*$, $\boldsymbol{A}^{-1}$, and A_{ii} represent trace, conjugate transpose, transpose, conjugate, inverse, and the i'th element on the main diagonal of $\boldsymbol{A}$. We indicate circularly symmetric complex Gaussian random vectors with covariance matrix $\boldsymbol{C}$ as $\boldsymbol{a} \sim \mathcal{CN}(0, \boldsymbol{C})$ and the expectation of a random variable by $\mathbb{E}\{\cdot\}$. We denote a diagonal matrix with elements $a_1, ..., a_N$ on the main diagonal by $\mathrm{diag}\,(a_1, ..., a_N)$ and the $K \times K$ identity matrix is indicated by $\boldsymbol{I}_K$.

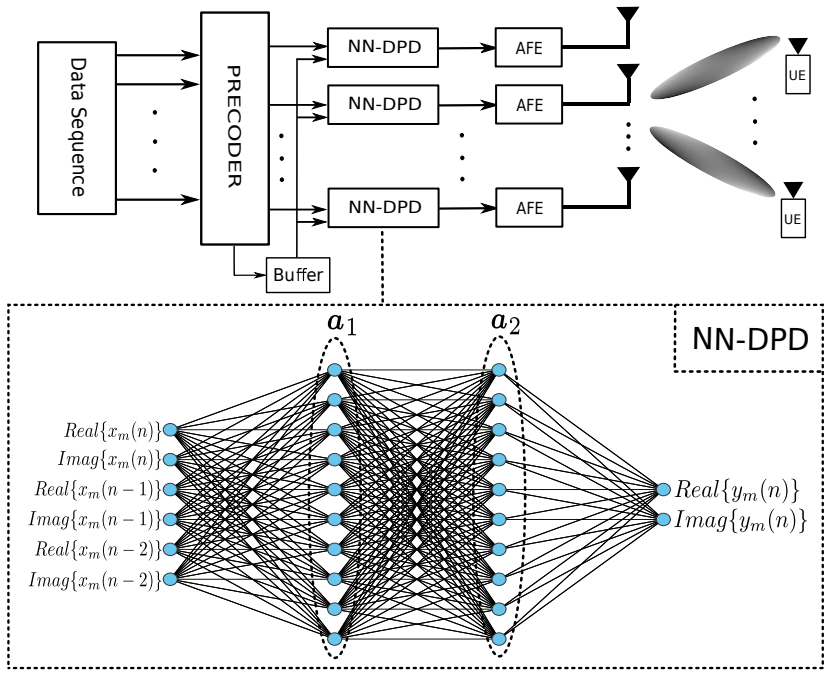

Figure 1: System Model with the architecture of an example NN-DPD.

2 System Model and General Considerations

We consider the downlink of a single-cell multi-user massive MIMO system with M antennas at the base station (BS) and K single-antenna UEs, randomly located in the cell area. The massive MIMO BS is assumed to be deployed with fully digital beamforming with M TX-chains, each having non-linear hardware components. The channel from BS to each UE is assumed to have a block fading model, meaning that the channel vector $\boldsymbol{h}_k \in \mathbb{C}_M$ is constant in each coherence block of the time-frequency plane, and changes independently between different blocks and it is therefore a stationary ergodic random process. Each of the channel vectors has an uncorrelated Rayleigh fading model with covariance matrix $\boldsymbol{R}_k$, which depends on the corresponding UE position in the cell. The covariance matrices are diagonal with different values on the main diagonal to model variant contributions of antennas along the array. To compensate for the non-linearity at the BS transceiver, we assume a per-antenna DPD block for each TX-chain, implemented as a neural network and trained as described in Section III.

The received signal at the UEs side after going through the DPDs, the

non-linear AFE, and the channel is

$$\boldsymbol{r} = \sqrt{G_0}\boldsymbol{H}^H f_{\text{AFE}}(f_{\text{DPD}}(\boldsymbol{W}\boldsymbol{s})) + \boldsymbol{n} \tag{1}$$

where G_0 is the power gain of the linearized ideal power amplifiers, $\boldsymbol{H} \in \mathbb{C}_{M\times K}$ is the channel matrix containing the channel vectors $\boldsymbol{h}_k$ from the BS to the UEs, $\boldsymbol{W} \in \mathbb{C}_{M\times K}$ is the precoder matrix with normalized unit-norm columns corresponding to each UE, $\boldsymbol{s} \in \mathbb{C}_{K\times 1}$ is the vector containing unit power data symbols corresponding to each UE, selected randomly and uniformly from a signal constellation, e.g. QPSK, and $\boldsymbol{n} \sim \mathcal{CN}(0, \sigma^2\boldsymbol{I}_K)$ indicates the additive white Gaussian noise at the UEs. The functions f_{AFE} and f_{DPD} model the base-band equivalent of the non-linear operations at the AFE and the DPD, respectively.

3 NN-DPD Architecture

Each of the TX chains are connected to an NN-DPD to compensate the non-linearity effects in their corresponding AFE blocks. Fig. 1 illustrates a schematic of the system model including an example architecture of an NN-DPD corresponding to the m'th TX chain. As it is depicted in the NN scheme, the output layer includes the real and imaginary parts of the corresponding TX chain which is be fed into the AFE. On the other side, the input layer includes the real and imaginary parts of the current and the last two input time samples of the corresponding TX chain which are stored in a buffer depending on memory concerns and complexity limitations. The complexity of the neural network architecture is limited by the total available resources allocated for DPD at the BS. Once the NN-DPD architectures are set, an indirect learning approach will be adopted to train the network parameters.

3.1 NN-DPD complexity

The NN-DPD complexity during the training and running is a major limiting factor that should be considered in the DPD system design. The training phase is performed mostly offline and it is not a concern, therefore most of the DPD works only focus on running complexity, which is a real-time cost and can limit the digital system overhead [13], [16]. In our proposed NN-DPD, depending on the available memory for storing the pre-trained coefficients of the NN-DPD, the system has different classes of pre-trained NN-DPDs and switch between the operating DPD classes depending on the system requirements and channel conditions. The number of floating point operations per second (FLOPs) is a commonly used measure that can accurately measure the operations complexity in NNs including additions, subtractions, and multiplications. Therefore,

the number of FLOPs used here has been widely selected as a measure of computational complexity in various types of NN-DPDs. The running complexity in a NN-DPD can be quantified by the number of multiplications and additions operated, where each real-valued multiplication or addition accounts for one FLOP [13], [16]. The computation power for performing the non-linear activation function is negligible compared to the other operations.

In a fully connected NN-DPD with $L-1$ hidden layers of size $n_l \times 1$, input layer of size $n_0 \times 1$, and output layer of size $n_L \times 1$, the total number of FLOPs for each use of the DPD during the running phase can be calculated as

$$F_{\mathrm{DPD}} = \sum_{i=1}^{L} 2n_i n_{i-1}, \tag{2}$$

derived by summing the total number of additions and multiplications in each layer, assuming the operation of each layer to be

$$\boldsymbol{a}_i = f_{\mathrm{act}}\left(\boldsymbol{C}_i \boldsymbol{a}_{i-1} + \boldsymbol{b}_i\right), \tag{3}$$

where $\boldsymbol{a}_i$ is the activation vector in i'th layer, $\boldsymbol{C}_i$ is the coefficients matrix, $\boldsymbol{b}_i$ is the bias vector, and $f_{\mathrm{act}}(.)$ indicates the non-linear activation function [17].

For a massive MIMO system with M TX-branches, each equipped with an NN-DPD, the total number of used FLOPs which can be related directly to the corresponding level of DPD power consumption is given by

$$F_{tot} = \sum_{m=1}^{M} \sum_{i=1}^{L_m} 2n_{m,i} n_{m,i-1}, \tag{4}$$

where subscript m indicates the NN-DPD parameters for the m'th TX branch. The total number of available FLOPs allocated for DPD is a design parameter that limits the system designer for selecting the NN-DPD size, i.e. the number of layers and their sizes.

3.2 NN-DPD training

Training data is generated and stored from the input-output data collected at the AFE. The number of training samples depends on the complexity of the NN-DPD architectures, i.e. if we have a complex NN with many layers, we need to generate and store a large number of training data. In an NN-DPD block, the NN models an inverse function of the non-linear input-output function of the non-ideal AFE. To find the inverse function, an Indirect Learning (IL) approach is adopted. The size of the input layer in the each NN-DPD depends on the concerns about the memory effects in the non-linear AFEs. If we consider a memory of length L_{mem}, the total number of neurons in the input layer of the

NN-DPD will be $2L_{\text{mem}}+2$, corresponding to the real and imaginary parts of the input values at the current sample time plus the L_{mem} previous sample. There will be two output neurons at the output layer of the NN-DPD which corresponds to the real and imaginary parts of the current AFE output. An example NN-DPD with fully connected architecture, $L=3$, and $L_{\text{mem}}=2$ is depicted in Fig. 1. The parameters to be trained are the weight matrices $\boldsymbol{C}_i$ and bias vectors $\boldsymbol{b}_i$ in (3).

3.3 System-Level performance of the NN-DPDs

The performance of DPD blocks in each TX-chain can be assessed by calculating the conventional performance metrics such as normalized mean square error (NMSE) and adjacent channel power ratio (ACPR) [13]. Since we are studying the trade-off between performance and complexity for the whole massive MIMO system with per-antenna DPD blocks at each TX-chain, we are more interested in system level performance metrics such as spectral efficiency or the signal to interference and noise plus distortion ratio (SINDR). Such a performance metric can give us insights on the importance of considering the trade-off between complexity and performance in a massive MIMO transmitter with NN-DPDs. We select the ergodic SINDR as the metric and calculate it as follows.

We assume the combination of the AFE and DPD non-linear functions, $f_{\text{AFE}}(.)$ and $f_{\text{DPD}}(.)$, as a general non-linear function $f(.)$ in the base-band. From (1), the received signal at the UEs side will be

$$\boldsymbol{r}=\sqrt{G_0}\boldsymbol{H}^H f(\boldsymbol{W}\boldsymbol{s})+\boldsymbol{n}, \tag{5}$$

where, for an ideal DPD, we have $f(\boldsymbol{W}\boldsymbol{s})=\boldsymbol{W}\boldsymbol{s}$. Therefore, we can expand the system model as

$$\boldsymbol{r}=\sqrt{G_0}\boldsymbol{H}^H\boldsymbol{W}\boldsymbol{s}+\sqrt{G_0}\boldsymbol{H}^H\left(f(\boldsymbol{W}\boldsymbol{s})-\boldsymbol{W}\boldsymbol{s}\right)+\boldsymbol{n}, \tag{6}$$

where the term $\boldsymbol{d}\triangleq f(\boldsymbol{W}\boldsymbol{s})-\boldsymbol{W}\boldsymbol{s}$, is the total residual distortion after applying DPDs to the AFEs. The k'th single-antenna UE receives

$$\begin{aligned} r_k=\sqrt{G_0}\boldsymbol{h}_k^H\boldsymbol{w}_k s_k+\sqrt{G_0}\sum_{i=1,i\neq k}^{K}\boldsymbol{h}_k^H\boldsymbol{w}_i s_i \\ +\sqrt{G_0}\boldsymbol{h}_k^H\boldsymbol{d}+n_k, \end{aligned} \tag{7}$$

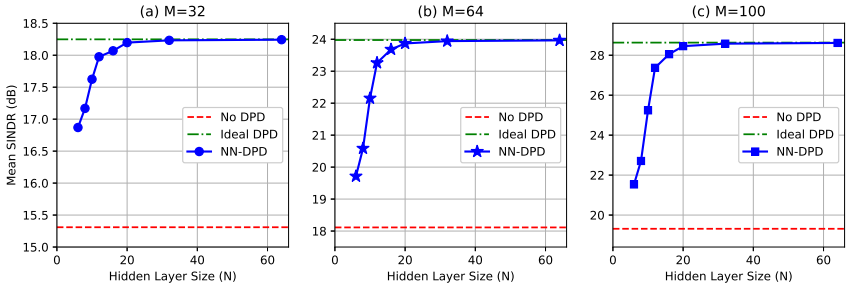

Figure 2: Mean of the SINDR (dB) at the UEs for $M = 32$ (a), $M = 64$ (b), and $M = 100$ (c) antennas at the BS with per-antenna NN-DPD with hidden layers size of N, no DPD, and ideal DPD.

and its corresponding SINDR can be calculated as

$$\rho_k = \frac{G_0 \mathbb{E}_{\boldsymbol{H}} \left[\left| \boldsymbol{h}_k^H \boldsymbol{w}_k \right|^2 \right]}{G_0 \sum_{i=1, i \neq k}^{K} \mathbb{E}_{\boldsymbol{H}} \left[\left| \boldsymbol{h}_k^H \boldsymbol{w}_i \right|^2 \right] + G_0 \mathbb{E}_{\boldsymbol{H},s} \left[\left| \boldsymbol{h}_k^H \boldsymbol{d} \right|^2 \right] + \sigma^2}. \tag{8}$$

If we use the zero-forcing precoder, we have $\boldsymbol{W} = \tilde{\boldsymbol{W}} \boldsymbol{G}_W$ where $\tilde{\boldsymbol{W}} = \boldsymbol{H}(\boldsymbol{H}^H \boldsymbol{H})^{-1}$ and

$$\boldsymbol{G}_W = \operatorname{diag}\left(\frac{1}{\|\tilde{\boldsymbol{w}}_1\|_2}, \frac{1}{\|\tilde{\boldsymbol{w}}_2\|_2}, ..., \frac{1}{\|\tilde{\boldsymbol{w}}_K\|_2} \right), \tag{9}$$

which is defined to normalize $\boldsymbol{W}$ such that each of its columns has a unit norm-2. By replacing this precoder scheme in (6) the SINDR in (8) is derived as

$$\rho_k = \frac{\frac{G_0}{\mathbb{E}_{\boldsymbol{H}} [\|\tilde{\boldsymbol{w}}_k\|_2]}}{G_0 \mathbb{E}_{\boldsymbol{H},s} \left[\left| \boldsymbol{h}_k^H \boldsymbol{d} \right|^2 \right] + \sigma^2}. \tag{10}$$

3.4 NN-DPD Size Selection

As mentioned in Section I, the massive MIMO system can benefit from the smart allocation of DPD resources among the per-antenna DPDs [14], which is the case because not all the antennas contribute equally [15]. In the current study on the trade-off between performance and complexity for an NN-DPD, we propose to have different classes of pre-trained NN-DPDs for each TX-chain and select the NN-DPD with the proper size based on the average channel conditions between each TX-chain and the UEs. To be able to perform this

size selection, there should be enough accessible memory to store the NN-DPDs pre-trained coefficients. For each of the NN-DPD classes, the total number of coefficients to be stored in memory for the M-antenna system described above can be calculated as

$$M_{\text{tot}} = \sum_{m=1}^{M} \sum_{i=1}^{L_m} n_{m,i} \left(n_{m,i-1} + 1 \right). \tag{11}$$

Depending on the total available memory and memory cell precision, the system designer can select the number of NN-DPD classes to be deployed in the proposed smart size selection of each TX-chain NN-DPD. To the best of our knowledge, it is not feasible to find an analytical relation between the NN-DPD complexity and its performance. Therefore, it is not possible to define an analytical optimization problem for selecting the NN-DPDs sizes. However, we propose to select the complexity of each NN-DPD class based on the memory limitations and add a size selection block that performs a heuristic search among the possible classes for the NN-DPD of each antenna and select the best combination by taking into account a decision criteria such as the proposed average SINDR in (8).

4 Performance Analysis

We analyze the performance of a multi-user massive MIMO transmitter for different NN-DPD architectures. We assume a massive MIMO system with M antennas at the BS and $K = 10$ single-antenna UEs. Each BS antenna has an NN-DPD to compensate for the non-ideal hardware effects at the corresponding transmitter chain. To have a better understanding of the performance comparison, we have also included two extreme cases in our results, one with no DPD (worst-case scenario), and the other with a perfect DPD (full compensation of hardware impairments). For other cases, we have deployed per-antenna NN-DPDs with different architectures. As explained in Section 3, the main constraint in selecting the architecture complexity is the total number of FLOPs to be allocated among the NN-DPDs.

To simplify the analysis and to alleviate the interpretation of the results, we have assumed a fully connected NN-DPD with two hidden layers ($L = 3$) of the same size, N, which is selected as the design parameter for the NN-DPDs. We also assume a memory-less model for the NN-DPD to reduce the complexity of the analysis, which means that the number of input and output neurons is set to 2. For each NN-DPD, there is a data set consisting of 2×10^5 input-output data samples. The data samples are generated using a memory polynomial model whose coefficients are extracted by curve-fitting to the AM/AM and AM/PM distortions of a measured GaN amplifier operating at 2.1 GHz [18].

We have added Gaussian noise to the data to account for possible errors during the measurements. The dataset is divided into three sets: 80% for training, 10% for validation, and 10% as a test set. The Rectified Linear Unit (ReLu) function, defined as $f_{\mathrm{ReLu}}(x) = max(0, x)$, is used as the activation function since it is easy to implement and has shown great performance in previous NN-DPD works [13]. The Adam Optimizer with an initial learning rate of 0.001 is adopted where the learning rate is decreased by a factor of 0.90 in each iteration of the training set. The batch size is set to 100 and the number of epochs is 5.

In Fig. 2, we study the performance of the system for different levels of NN-DPD complexity by adjusting the parameter N from 6 to 64 for each of the per-antenna NN-DPDs. The analysis is performed for three different number of antennas to illustrate the effect of scaling up a MIMO system. Firstly, we can see that by going from a low-power low-end NN-DPD ($N = 6$) to a power hungry high-end NN-DPD ($N = 64$), we can approach the performance of the case with an ideal DPD at each antenna. The performance is already close to its upper limit for $N = 20$. One should note that if the severity of the hardware non-linearity at the AFEs increases, the minimum NN-DPD complexity to approach the ideal case also increases which may not be feasible in practice where we have a limited DPD power budget. Nevertheless, this analysis implies that NN-DPDs are very powerful in compensation the non-linearity effect, even for a fairly simple NN architecture. Secondly, it is important to notice that the performance gain achieved by increasing the NN-DPD complexity is much more significant for larger arrays. In Fig. 3, the difference of the achieved performance gain by increasing the NN-DPD complexity can be seen more clearly. In fact, we can conclude that compared to a MIMO system with a low number of antennas, investing the system resources in implementing a well-trained NN-DPD with fairly high complexity pays off in a massive MIMO system.

In Fig. 4, the cumulative distribution function (CDF) of the SINDR is depicted for different architecture selection strategies of the NN-DPDs. Unlike the previous figures where we had assumed Rayleigh channels with the same fading conditions for all the antennas, we have now assumed that 20% of the antennas have $7dB$ higher channel gain compared to the others, which is based on the difference in antennas contribution in massive MIMO systems [15]. First of all, it can be seen that by adopting a high-end NN-DPD, with layer size $N = 16$, at each TX-branch we can have a performance fairly close to the optimal case, which implies the power of neural networks in performing the DPD tasks. However, one should note that having such high-end DPDs in a massive MIMO system with hundreds of Tx-branches is not practically feasible in scenarios with limited digital computation powers.

The two middle plots in Fig. 4 are the practical scenarios where the computation power limitation is taken into account. The uniform NN-DPD strategy

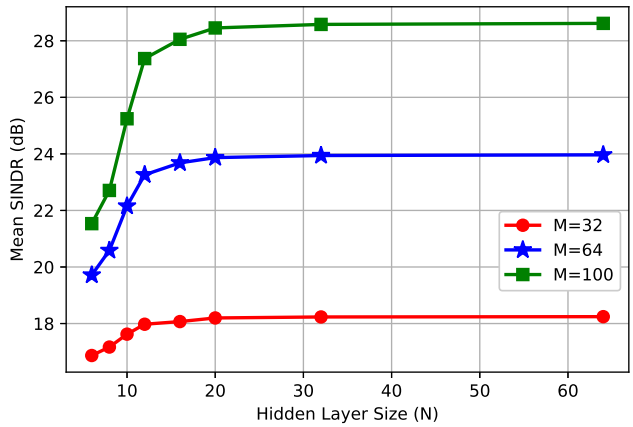

Figure 3: Mean of the SINDR (dB) at the UEs for $M = 32$ (a), $M = 64$ (b), and $M = 100$ (c) antennas at the BS with per-antenna NN-DPD with hidden layer size of N.

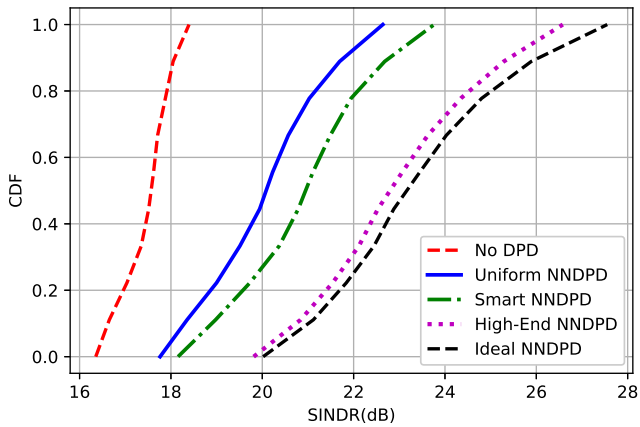

Figure 4: CDF of SINDR (dB) for a UE randomly located at the cell area.

assumes allocation of the total FLOPS uniformly among the TX-chains which corresponds to $N = 10$. The smart NN-DPD corresponds to adopting the low-end NN-DPD with $N = 8$ for 80% of the antennas and the high-end NN-DPD with $N = 16$ for the 20% antennas with higher contribution, which in total consumes the same number of FLOPs as the uniform strategy with $N = 10$. As it can bee seen in the figure, by adopting our proposed method, which is

namely selecting the NN-DPDs architectures based on their large-scale fading conditions, we can have a significant boost in the SINDR of a UE which is randomly allocated in the cell area, compared to the case with uniform allocation of the DPD resources. This performance gain allows the system designer to decrease the overall system cost, either by decreasing the total number of active TX-chains, or the linearity requirements of the hardware equipments adopted at the BS. Such cost reductions are crucial in massive MIMO and Large Intelligent Systems (LIS) where the number of antenna elements are in the range of hundreds to thousands.

5 Conclusion

In this paper we have studied the trade-off between complexity and performance in a massive MIMO system with per-antenna NN-DPDs. In particular, we have shown that by training multiple classes of NN-DPDs and selecting the class for each antenna based on the channel conditions of the massive MIMO array, we can improve the performance for the same level of total complexity in the DPD blocks. We also investigate the performance of the NN-DPDs for different levels of complexity in the neural networks architecture, which indicates that a well designed NN-DPD with fairly high complexity can have near-optimal performance in compensating the hardware non-linearity effects.

References

[1] E. Björnson, L. Sanguinetti, H. Wymeersch, J. Hoydis, and T. L. Marzetta, "Massive MIMO is a reality—what is next?: Five promising research directions for antenna arrays," *Digital Signal Processing*, vol. 94, pp. 3–20, 2019, Special Issue on Source Localization in Massive MIMO.

[2] E. G. Larsson, O. Edfors, F. Tufvesson, and T. L. Marzetta, "Massive MIMO for next generation wireless systems," *IEEE Communications Magazine*, vol. 52, no. 2, pp. 186–195, 2014.

[3] F. Rusek et al., "Scaling up MIMO: Opportunities and challenges with very large arrays," *IEEE Signal Processing Magazine*, vol. 30, no. 1, pp. 40–60, 2013.

[4] E. Björnson, M. Matthaiou, and M. Debbah, "Massive MIMO with non-ideal arbitrary arrays: Hardware scaling laws and circuit-aware design," *IEEE Transactions on Wireless Communications*, vol. 14, no. 8, pp. 4353–4368, 2015.

[5] B. Razavi, *RF Microelectronics (2nd Edition) (Prentice Hall Communications Engineering and Emerging Technologies Series)*, 2nd. USA: Prentice Hall Press, 2011.

[6] M. Sarajlić, A. Sheikhi, L. Liu, H. Sjöland, and O. Edfors, "Power scaling laws for radio receiver front ends," *IEEE Transactions on Circuits and Systems I: Regular Papers*, vol. 68, no. 5, pp. 2183–2195, 2021.

[7] D. Morgan, Z. Ma, J. Kim, M. Zierdt, and J. Pastalan, "A generalized memory polynomial model for digital predistortion of RF power amplifiers," *IEEE Transactions on Signal Processing*, vol. 54, no. 10, pp. 3852–3860, 2006.

[8] J. Kim and K. Konstantinou, "Digital predistortion of wideband signals based on power amplifier model with memory," *Electronics Letters*, vol. 37, no. 23, p. 1, 2001.

[9] K. Muhonen, M. Kavehrad, and R. Krishnamoorthy, "Look-up table techniques for adaptive digital predistortion: A development and comparison," *IEEE Transactions on Vehicular Technology*, vol. 49, no. 5, pp. 1995–2002, 2000.

[10] A. Katz, J. Wood, and D. Chokola, "The evolution of PA linearization: From classic feedforward and feedback through analog and digital predistortion," *IEEE Microwave Magazine*, vol. 17, no. 2, pp. 32–40, 2016.

[11] F. Mkadem and S. Boumaiza, "Physically inspired neural network model for RF power amplifier behavioral modeling and digital predistortion," *IEEE Transactions on Microwave Theory and Techniques*, vol. 59, no. 4, pp. 913–923, 2011.

[12] P. Jaraut, M. Rawat, and F. M. Ghannouchi, "Composite neural network digital predistortion model for joint mitigation of crosstalk, I/Q imbalance, nonlinearity in MIMO transmitters," *IEEE Transactions on Microwave Theory and Techniques*, vol. 66, no. 11, pp. 5011–5020, 2018.

[13] Y. Wu, U. Gustavsson, A. G. I. Amat, and H. Wymeersch, "Low complexity joint impairment mitigation of I/Q modulator and PA using neural networks," *IEEE Journal on Selected Areas in Communications*, vol. 40, no. 1, pp. 54–64, 2022.

[14] A. Sheikhi, F. Rusek, and O. Edfors, "Massive MIMO with per-antenna digital predistortion size optimization: Does it help?" In *ICC 2021 - IEEE International Conference on Communications*, 2021, pp. 1–6.

[15] X. Gao, O. Edfors, F. Tufvesson, and E. G. Larsson, "Massive MIMO in real propagation environments: Do all antennas contribute equally?" *IEEE Transactions on Communications*, vol. 63, no. 11, pp. 3917–3928, 2015.

[16] A. S. Tehrani, H. Cao, S. Afsardoost, T. Eriksson, M. Isaksson, and C. Fager, "A comparative analysis of the complexity/accuracy tradeoff in power amplifier behavioral models," *IEEE Transactions on Microwave Theory and Techniques*, vol. 58, no. 6, pp. 1510–1520, 2010.

[17] J. E. Dayhoff, *Neural Network Architectures: An Introduction*. USA: Van Nostrand Reinhold Co., 1990.

[18] "Further elaboration on PA models for NR," *document 3GPP TSG-RAN WG4, R4-165901, Ericsson, Stockholm, Sweden*, Aug. 2016.

Paper III

Large Intelligent Surfaces with Low-End Receivers: From Scaling to Antenna and Panel Selection

We analyze the performance of LIS with hardware distortion at its RX-chains. In particular, we consider the memory-less polynomial model for non-ideal hardware and derive analytical expressions for the signal to noise plus distortion ratio after applying MRC at the LIS. We also study the effect of back-off and automatic gain control on the RX-chains. The derived expressions enable us to evaluate the scalability of LIS when hardware impairments are present. We also study the cost of assuming ideal hardware by analyzing the minimum scaling required to achieve the same performance with a non-ideal hardware. Then, we exploit the analytical expressions to propose optimized antenna selection schemes for LIS and we show that such schemes can improve the performance significantly. In particular, the antenna selection schemes allow the LIS to have lower number of non-ideal RX-chains for signal reception while maintaining a good performance. We also consider a more practical case where the LIS is deployed as a grid of multi-antenna panels, and we propose panel selection schemes to optimize the complexity-performance trade-offs and improve the system overall efficiency.

Ashkan Sheikhi,, J. Vidal Alegría, Ove Edfors,
"Large Intelligent Surfaces with Low-End Receivers: From Scaling to Antenna and Panel Selection,"
Under revision for publication in *IEEE Transactions on Wireless Communications*, 2025.

1 Introduction

LISs have emerged as one of the next major steps in the future development of MIMO communication systems [1], [2], [3]. While LISs are sometimes considered to be a scaled up version of the widely known massive MIMO systems, they have some unique properties which distinguishes them from the massive MIMO systems. For instance, their physical size can be compared to the user-equipment (UE) distance to the LIS, which introduces near-field effects in the wireless channel. As a result, the common assumptions about the massive MIMO channels are no longer valid and new effects emerge. This requires different channel models, and more investigation into the already known facts about the transmit and receive schemes in massive MIMO systems [4].

The LIS technology was initially introduced in [1] as a large surface of electromagnetically active material in a line of sight (LOS) channel model. LIS was first proposed as a continuous model where any point of a continuous surface can transmit and receive signals. While this continuous model is useful to understand the concepts of a LIS system, it can not be implemented with current technology in the near future. Instead, a dense antenna array deployed throughout a large surface is more realistic which can also be interpreted as a sampled version of the continuous LIS model. It has been shown that, if sampling is dense enough, e.g half wavelength spatial sampling, the continuous and sampled versions of LIS have the same performance in terms of available spatial degrees of freedom due to the spatially-band-limited nature of the channels [1], [5]. More practical implementations of LIS consider dividing the LIS surface into dense multi-antenna panels with a lower number of antennas, which is a more flexible and scalable design with reduced system complexity [6]. What we refer to as LIS in this manuscript, corresponds to an active sampled-surface or panel-based array which should not be confused with a Reconfigurable Intelligent Surface (RIS) and an Intelligent Reflecting Surface (IRS).

The deployment of LISs is envisioned to be much more challenging because of the enormous leap in the number of transceiver chains, and the associated processing complexities. One important challenge is the cost efficiency of the whole system, where hundreds to thousands of transceiver chains are to be deployed, which may force systems designers to consider the use of inexpensive hardware components in each of these transceiver chains [7]. Therefore, it is of high importance to study and mitigate the effects of hardware distortion in transceiver chains when scaling up LIS to allow the use of cost-efficient transceiver chains. There has been previous works on the design and optimizing IRS and RIS based system with hardware impairment [8], [9], [10], [11]. However, these works have no direct applicability to our study due to the intrinsically different system model associated to passive reflective surfaces compared to active transceiver technologies which we refer to as LIS.

The vision for future antenna arrays in the next generation of wireless com-

munication systems highly depends on deploying arbitrarily large arrays due to the compelling gains in terms of multiplexing and beamforming performance through increasing spatial resolution [12]. With traditional design approaches, implementing such a huge array may not be economically favored for operators and vendors, since each antenna is typically equipped with an analog and a digital front-end (AFE and DFE) [6]. The requirements for each transceiver chain may lead to unreasonable implementation costs [13]. On the other hand, the power consumption of each transceiver can also become a bottleneck, especially if there are tight requirements on the non-linearity of amplifiers and the out-of-band emissions. AFEs are considered to be one of the main sources of hardware distortion in receivers [14], [15], [16]. Not only the non-linearity effect of AFEs are important to consider, but also the limitations in the total power consumption of the receiver chain is of great importance. Linearity requirements in the RX-chains can result in a huge leap in power consumption of the whole system [17], which is not favorable neither in terms of cost nor energy efficiency.

To deal with these challenges, we need to make the receiver design as efficient as possible, from a system perspective. In general, the path to follow is to optimize the signal processing schemes and system designs while maintaining the hardware quality at a minimum level. In other words, we want to get the most gain from each transceiver chain while limiting the implementation costs, e.g., by using inexpensive hardware components. In [18] and [19], we have proposed approaches to address such challenges in massive MIMO systems, mainly by optimizing the per-antenna digital pre-distortion (DPD) resources. Another approach is to perform antenna selection methods and only use a portion of the array for transmission and reception. By doing so, we only use antennas which have a significant contribution to the performance and thereby increase energy efficiency.

In this paper, we focus on optimizing the performance of LIS with non-ideal RX-chains. We first analyze the SNDR with the purpose of studying the scaling behavior and asymptotic limits of LIS with hardware distortion. Then, we propose receive antenna selection schemes for a LIS with non-ideal AFEs. Optimization problems are defined and solved to illustrate the importance of performing antenna selection when scaling up LIS. We show that selecting antennas with the strongest channels is not always the optimal solution. We then focus on more practical cases where the LIS is implemented as a grid of panels, and transform the antenna selection problem into a panel selection problem. Low-complexity closed-form sub-optimal solutions are proposed for the panel selection. We also show that, by adopting such antenna selection and panel selection schemes, we can improve the system performance significantly for a fixed receive-chain hardware quality.

1.1 Contributions

The contributions of this paper are listed as follows.

- We provide a framework to study the hardware distortion effect on LIS performance while considering high-complexity non-linear polynomial model at RX-chains.
- We derive close-form expressions for the SNDR of the LIS under polynomial hardware distortion model to enable scaling and asymptotic analysis.
- We introduce antenna selection problems in LIS with hardware distortion and illustrate the achievable gains of adopting optimal antenna selection. We also consider the the more practical case with a panel-based LIS and propose closed-form solutions for panel selection with hardware distortion effects.

1.2 Paper Outline

The rest of this paper is organized as follows. In Section 2, the system model is introduced, which includes the LIS deployment configurations, channel model, and hardware distortion model. In Section 3, we characterize the SNDR and propose closed-form expressions to evaluate the LIS performance, which is exploited for asymptotic and scaling analysis. Sections 4 and 5 introduce the antenna and panel selection problems, respectively, and some proposed solutions are presented for the corresponding LIS scenarios. In Section 6, numerical results are used to further illustrate the results from previous sections. Finally, Section 7 concludes the paper results.

1.3 Notation

Matrices, vectors, and scalars are denoted by boldface uppercase, boldface lowercase, and italic letters, respectively. For a vector $\boldsymbol{a}$, conjugate transpose, transpose, Euclidean norm, and the i'th element of $\boldsymbol{a}$ are represented by $\boldsymbol{a}^H$, $\boldsymbol{a}^T$, $\|\boldsymbol{a}\|$, and a_i, respectively. For a scalar a, the complex conjugate is denoted by $\bar{a}$. We indicate zero-mean circularly-symmetric complex Gaussian random vectors with covariance matrix $\boldsymbol{C}$ as $\boldsymbol{a} \sim \mathcal{CN}(\boldsymbol{0}, \boldsymbol{C})$ and the expectation of a random variable by $\mathbb{E}\{\cdot\}$. We denote a diagonal matrix with elements $a_1, ..., a_N$ on the main diagonal by $\text{diag}\,(a_1, ..., a_N)$ and the $N \times N$ identity matrix by $\boldsymbol{I}_N$.

2 System Model

We consider an uplink scenario where an active LIS consisting of $N \gg 1$ antenna elements serves a single-antenna UE, which transmits the complex base-

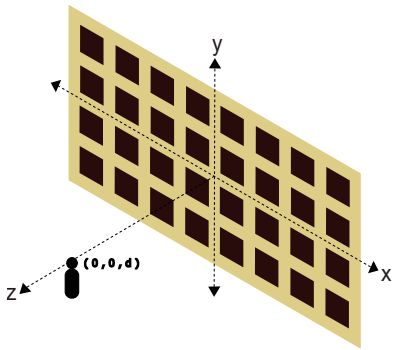

Figure 1: LIS and UE configuration. The LIS is centered around origin and the UE is on the bore-sight of the LIS.

band symbol $s \in \mathbb{C}$ with $\mathbb{E}\{|s|^2\} = P$, over a channel $\boldsymbol{h} \in \mathbb{C}^{N\times 1}$. Each receive antenna is equipped with a non-ideal RX-chain, introducing distortion into the received signal. The received signal after going through the RX-chains is expressed as

$$\boldsymbol{r} = f\left(\boldsymbol{h}s\right) + \boldsymbol{n}, \tag{1}$$

where $f(\cdot) : \mathcal{C}^{N\times 1} \to \mathcal{C}^{N\times 1}$ models the overall non-ideal effects at the receiver AFEs and DFEs of the LIS, and $\boldsymbol{n} \sim \mathcal{CN}(\boldsymbol{0}, \sigma^2 \boldsymbol{I}_N)$ is the additive noise.

The LIS is assumed to span the x-y plane with its center located at the origin, and the UE is assumed to be located at $(0, 0, d)$, where d denotes the distance of the UE to the center of the LIS. Fig. 1 illustrates the configuration of the LIS and the UE. The UE is assumed in the far-field region of each antenna element, i.e. $d > 2D_a^2/\lambda$, where D_a is the maximum length of individual antenna elements. However, since the number of antenna elements can grow extremely large, the UE may be enter the near-field region of the LIS [4], [20], i.e. $d < 2\bar{D}^2/\lambda$, where $\bar{D}$ is the largest distance between two antenna elements on the array. Therefore, it is important to consider both phase and amplitude variations across the array, and consider near-field effects in the channel model.

In, [4], the effect of considering near-field properties in the channel model is studied, including the variation of distance from each antenna element to the UE, different effective area, and different polarization losses due to different angle of arrivals. The results in [4] imply that only considering the first two effects or considering all the three effects , even if the number of antenna elements grows extremely large, have negligible difference. Therefore, we only consider the first two effects and adopt the near-field LOS channel model as considered in [1]. The narrow-band channel $h(x, y) = |h(x, y)| \exp\left(-j\phi(x, y)\right)$ between the UE and a point on the LIS with coordinates $(x, y, 0)$ has amplitude

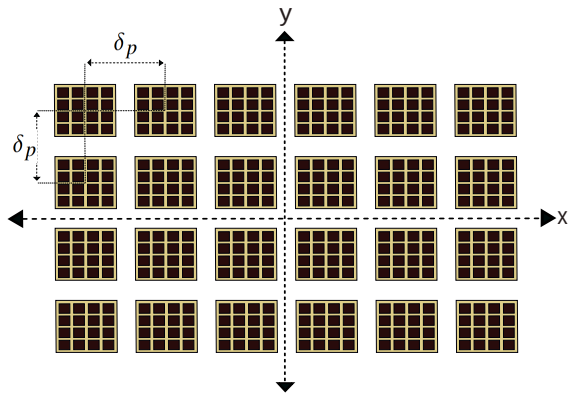

Figure 2: Panels configuration, the panel-based LIS is centered around origin with a fixed distance δ_p between adjacent panels.

given by

$$|h(x,y)| = \frac{\sqrt{d}}{2\sqrt{\pi}(d^2+x^2+y^2)^{3/4}}, \tag{2}$$

and the phase based on propagation delay as

$$\phi(x,y) = 2\pi\frac{\sqrt{d^2+x^2+y^2}}{\lambda}, \tag{3}$$

where λ is the wavelength. For the n'th antenna element, located at $(x_n, y_n, 0)$ with effective area A small enough such that $|h(x,y)|^2$ is almost fixed inside its effective area[1], the channel gain is $|h_n|^2 = A|h(x_n,y_n)|^2$.

While this form of deployment is a common vision for the LIS implementation in the future of wireless networks [21], it is not favorable with current technology from a practical point of view [22]. A potentially more favorable option, without losing practicality and cost efficiency is to implement the LIS as grid of panels, each equipped with some equally distanced antenna elements [6]. Fig. 2 illustrates an example of panel configuration of a LIS on the x-y plane.

2.1 Hardware distortion model

There are several models to opt for the distortion function $f(\cdot)$ in (1) and the model selection is always a trade-off between accuracy and analytical tractabil-

[1]This assumption is valid in most practical MIMO scenarios since the effective area is in the orders of $\frac{\lambda^2}{4}$ and the UE is in the far-field of each individual antenna element, i.e. $d \gg \frac{\lambda}{2}$.

ity. One of the common models in the literature is the memory-less polynomial, which has an high accuracy in most cases, at the cost of high complexity in the analytical results. We mainly focus on this model throughout this paper to guarantee the accuracy of the analysis. In this model, the input-output relation of an RX-chain for a complex input $x_{\text{in}} \in \mathbb{C}$ is given by

$$y_{\text{out}} = f(x_{\text{in}}) = \sum_{k=0}^{L-1} a_{2k+1}\ x_{\text{in}}|x_{\text{in}}|^{2k}, \tag{4}$$

where $a_{2k+1} \in \mathbb{C}$ are the model parameters, typically estimated based on input-output measurements on the RX-chains. This model only considers odd orders since they are the main source of in-band distortion [23]. For an ideal RX-chain, we have $L = 1$ and $a_1 = 1$.

Let us first analyze the distortion behavior for a single RX-chain. To isolate the distortion from the desired signal, we can rewrite (4) by using the LMMSE of y given x as

$$y_{\text{out}} = \frac{C_{y_{\text{out}}x_{\text{in}}}}{C_{x_{\text{in}}}} x_{\text{in}} + \eta, \tag{5}$$

where $C_{y_{\text{out}}x_{\text{in}}}$ is the covariance between y_{out} and x_{in}, $C_{x_{\text{in}}}$ is the auto-correlation of x_{in}, and η is the estimation error. Equation (5) also corresponds to the Bussgang decomposition, which is a popular tool in hardware distortion analysis [24]. By defining $g = C_{y_{\text{out}}x_{\text{in}}}/C_{x_{\text{in}}}$ as the Bussgang gain and noting that η is uncorrelated with x, the auto-correlation of η is given by

$$C_\eta = C_{y_{\text{out}}} - |g|^2 C_{x_{\text{in}}}, \tag{6}$$

which can be calculated using the following lemma.

Lemma 3 *Given the memory-less polynomial model in* (4)*, together with its Bussgang equivalent form, and assuming a Gaussian input distribution, i.e.* $x_{in} \sim \mathcal{CN}(0, P)$*, we can calculate the Bussgang gain as*

$$g = \frac{\mathbb{E}\left[y_{in}\bar{x}_{in}\right]}{\mathbb{E}\left[|x_{in}|^2\right]} = \sum_{k=0}^{L-1} a_{2k+1}(k+1)!P^k, \tag{7}$$

and the distortion power as

$$C_\eta = \mathbb{E}\left[|\eta|^2\right] = \sum_{k=1}^{2L-1} \left(k!P^k \sum_{i=1}^{k} a_{2i-1}\bar{a}_{2k-2i+1} \right) - |g|^2 P, \tag{8}$$

where $P = \mathbb{E}\left[|x_{in}|^2\right]$.

Proof *See Appendix 8.* □

In practice, the 3rd order non-linearity term, a_3, is the dominant source of RF-hardware distortions [23], [25]. For the special case of 3rd order non-linearity, i.e. $L = 2$, Lemma (3) gives

$$g = a_1 + 2a_3P, \tag{9}$$

and

$$C_\eta = 2|a_3|^2P^3. \tag{10}$$

2.2 AGC and back-off

As mentioned earlier, the model coefficients are estimated based on input-output measurements of the RX-chain. The results are usually reported for a normalized input with unit maximum amplitude [26]. Given the estimated parameters $\hat{a}_{2k+1}$, for the normalized input, if the actual input to the receiver has an amplitude range of $0 < |x| < V_{max}$, we can use the following conversion to adapt the normalization

$$a_{2k+1} = \frac{\hat{a}_{2k+1}}{(V_{\max}^2)^k}. \tag{11}$$

The value of $V_{\max}$ can be controlled in the receiver by applying back-off to its input, either by using attenuator or by performing gain control schemes in the RX-chain amplifiers. The back-off is applied to prevent clipping, which may cause severe hardware distortion at the receivers. In our system, we define $V_{\max}^2 = b_{\text{off}}P_{\max}$, where b_{off} is the fixed back-off factor and $P_{\max}$ depends on the gain control scheme at the receiver. In a typical LIS scenario, the received power at each antenna element can have a high dynamic range, which makes the interplay between the back-off, gain control, and hardware distortion of great importance.

The back-off value, b_{off}, is a design parameter which can be selected based on the dynamic range of the received power across the LIS. The gain control term, $P_{\max}$, on the other hand can be set either to a fixed value for all the antenna elements, or depending on the received power on each antenna, which may be achieved by introducing per-antenna AGC in the amplifiers. The latter case may be of less interest from a practical point of view in LIS scenarios since there are hundreds to thousands of RX-chains across the LIS, with a high variation of the received power. Therefore, having a perfect gain control unit on each antenna element can contribute to the already high complexity of the

whole system, apart from increasing implementation costs. On the other hand, applying a fixed gain control is simpler and less expensive to implement, but has the disadvantage of excessive gain reduction on some antennas, which can reduce the energy efficiency of the amplifiers. In this paper we study both cases and compare their performance.

If all RX-chains are capable of performing individual AGC, the per-antenna coefficients $a_{k,n}$ become

$$a_{2k+1,n} = \frac{\hat{a}_{2k+1}}{(b_{\text{off}} P \left|h_n\right|^2)^k}, \tag{12}$$

and, in this case, calculating the Bussgang parameters in Lemma 3 results in a fixed Bussgang gain

$$\tilde{g} = \sum_{k=0}^{L-1} \frac{\hat{a}_{2k+1}}{b_{\text{off}}^k} (k+1)! \tag{13}$$

for all antenna elements. The distortion power, on the other hand, is a linearly increasing function of the input power to the corresponding antenna, i.e. $C_n = \kappa \left|h_n\right|^2 P$, where

$$\kappa = \sum_{k=1}^{2L-1} \left(\frac{k!}{b_{\text{off}}^{k-1}} \sum_{i=1}^{k} \hat{a}_{2i-1} \bar{\hat{a}}_{2k-2i+1} \right) - \left|\tilde{g}\right|^2. \tag{14}$$

We may thus note that by assuming per-antenna perfect AGC, the Bussgang gain and the distortion growth rate are independent of the input power or the antenna index across the LIS.

As we will see in the next section, the assumption of per-antenna AGC can reduce the complexity of the analysis. Interestingly, the linear growth rate in (14) can be seen as a bridge from the memory-less polynomial model in (4) to the conventional additive linear distortion model, which is widely used in literature [27]. One should note that the additive linear distortion model is a rough and simple approach of modeling the hardware distortion, where the single parameter κ denotes the severeness of the hardware distortion and can be interpreted as a measure of RX-chain hardware quality. In general, perfect per-antenna AGC assumption and the additive linear model are not accurate. Such assumptions imply that, no matter what the input power is, the Bussgang gain, $\tilde{g}$, and the distortion growth rate, κ, are constants. Nevertheless, we consider both the case where per-antenna AGC is employed, as well as the case with fixed gain control, for completeness and to gain better understanding of the impact of such assumptions.

3 SNDR Characterization

By using the same technique as in (5) which is based on LMMSE or Bussgang decomposition, the received signal in (1) may be expressed as

$$\boldsymbol{r} = \boldsymbol{G}\boldsymbol{h}s + \boldsymbol{\eta} + \boldsymbol{n}, \tag{15}$$

where $\boldsymbol{G} = \text{diag}\,(g_1, \ldots, g_N)$, with g_n corresponding to the Busssgang gain for the n'th antenna as given in (7), and $\boldsymbol{\eta}$ is the vector containing additive distortion at the LIS, with covariance matrix $\boldsymbol{C}_{\boldsymbol{\eta}\boldsymbol{\eta}}$, which is a non-diagonal matrix in general. The distortion correlation effect among antennas can be neglected in some cases, resulting in over-estimating the SNDR, which is often considered in the literature [28]. The effect of disregarding the distortion correlation is studied in Section 6.3.

The LIS applies a combing vector $\boldsymbol{v}$ to the received signal $\boldsymbol{r}$ to equalize the transmitted signal. Maximum Ratio Combining (MRC) is an attractive option in LIS scenarios because of its simplicity and reasonable performance, since it still allows us to exploit the available spatial degrees of freedom[1]. In our scenario, the MRC vector may be expressed as $\boldsymbol{v}^T = \tilde{\boldsymbol{h}}^H/\|\tilde{\boldsymbol{h}}\|$ where $\tilde{\boldsymbol{h}} = \boldsymbol{G}\boldsymbol{h}$, can be interpreted as the effective channel, which includes the physical channel and the multiplicative hardware distortion effect. In fact, the LIS would only be able to estimate the effective channel $\tilde{\boldsymbol{h}}$ from the uplink UE pilots since the signals received during channel estimation are also affected by the hardware distortion. We assume that the LIS has a perfect estimate of $\tilde{\boldsymbol{h}}$ so that we can isolate the effect of hardware distortion from that of channel estimation imperfections. Note that the estimation error would only correspond to an uncorrelated additive term, which would effectively not affect our analysis on hardware distortion.

By applying the combining vector $\boldsymbol{v}^T = \tilde{\boldsymbol{h}}^H/\|\tilde{\boldsymbol{h}}\|$ to $\boldsymbol{r}$, we reach

$$\boldsymbol{v}^T\boldsymbol{r} = \frac{\tilde{\boldsymbol{h}}^H\tilde{\boldsymbol{h}}s + \tilde{\boldsymbol{h}}^H\boldsymbol{\eta} + \tilde{\boldsymbol{h}}^H\boldsymbol{n}}{\|\tilde{\boldsymbol{h}}\|}. \tag{16}$$

The signal, distortion, and noise power can be calculated from (16) considering that the distortion term is uncorrelated with the signal and has covariance $\boldsymbol{C}_{\boldsymbol{\eta}\boldsymbol{\eta}}$. The instantaneous SNDR is therefore given by

$$\gamma = \frac{P\tilde{\boldsymbol{h}}^H\tilde{\boldsymbol{h}}}{\frac{\tilde{\boldsymbol{h}}^H\boldsymbol{C}_{\boldsymbol{\eta}\boldsymbol{\eta}}\tilde{\boldsymbol{h}}}{\tilde{\boldsymbol{h}}^H\tilde{\boldsymbol{h}}} + \sigma^2}. \tag{17}$$

If we assume that the distortion correlation among the antennas are negligible, i.e., $\boldsymbol{C}_{\boldsymbol{\eta}\boldsymbol{\eta}}$ is diagonal, the instantaneous SNDR can be simplified, which results in more analytical tractability for studying the impact of hardware dis-

tortion on LIS systems. We analyze the effect of this assumption in Section 6.3 and show that it does not invalidate the conclusions drawn regarding scaling up of LIS systems with hardware distortion. Moreover, it leads to significant simplification of the proposed methods, at the cost of only a minor performance loss. Assuming diagonal $\boldsymbol{C}_{\boldsymbol{\eta\eta}}$ given by $\boldsymbol{C}_{\boldsymbol{\eta\eta}} = \mathrm{diag}\left(C_1, \ldots, C_N\right)$, where C_n corresponding the distortion power for the n'th antenna as given in (8), the instantaneous SNDR is simplified to

$$\gamma = \frac{P \sum_{n=1}^{N} \left|\tilde{h}_n\right|^2}{\frac{\sum_{n=1}^{N} C_n \left|\tilde{h}_n\right|^2}{\sum_{n=1}^{N} \left|\tilde{h}_n\right|^2} + \sigma^2}, \tag{18}$$

where $\left|\tilde{h}_n\right|^2$ and C_n may be calculated using Lemma 3. Noting that the input power to the n'th RX-chain is $P|h_n|^2$, we have

$$\left|\tilde{h}_n\right|^2 = |h_n|^2 \left| \sum_{k=0}^{L-1} a_{2k+1,n} (k+1)!\ P^k |h_n|^{2k} \right|^2, \tag{19}$$

and

$$C_n = \sum_{k=1}^{2L-1} \left(k!\ P^k |h_n|^{2k} \sum_{i=1}^{k} a_{2i-1,n} \bar{a}_{2k-2i+1,n} \right) - \left|\tilde{h}_n\right|^2 P, \tag{20}$$

where the variables $a_{k,n}$ indicate the coefficients for the n'th antenna RX-chain non-linear function in (4).

For the case with per-antenna AGC, since $\tilde{h}_n = \tilde{g} h_n$ and $C_n = \kappa \left|h_n\right|^2 P$, the SNDR in (18) is simplified to

$$\gamma = \frac{P|\tilde{g}|^2 \sum_{n=1}^{N} |h_n|^2}{\kappa P \frac{\sum_{n=1}^{N} |h_n|^4}{\sum_{n=1}^{N} |h_n|^2} + \sigma^2}. \tag{21}$$

We are now interested in finding closed-form approximations for the SNDR to facilitate the LIS scaling analysis. We assume the LIS and UE configuration as depicted in Fig. 1. This specific LIS-UE configuration is selected to reduce the complexity of the analytical derivations; however, this loss of generality has reduced impact when considering general scenarios with a large enough LIS [2].

If we assume that the LIS consists of $\sqrt{N} \times \sqrt{N}$ square antenna elements with effective area A, placed edge to edge such that the distance between adjacent antennas is $\sqrt{A}$, we can approximate the summations in (21) by using the Riemann Integral approximation [29]. Since $N \gg 1$ in LIS scenarios, we

can approximate the LIS surface as a disk with radius R, with the same area as the square-shaped LIS, i.e. $NA = \pi R^2$. Therefore, the N antenna elements are assumed in a disk-shaped region $\mathcal{S}$ with a distance smaller than R from the center of the LIS, i.e., the antennas with $x_n^2 + y_n^2 < R$. Numerical results show that this approximation results in negligible error in the summation approximations when $N \gg 1$. We have

$$\begin{aligned}\sum_{n=1}^{N} |h_n|^2 &\approx \iint_{\mathcal{S}} |h(x,y)|^2 dxdy \\ &= \int_{\phi=0}^{2\pi} \int_{r=0}^{R} |h(r)|^2 r dr d\phi, \end{aligned} \tag{22}$$

where $|h(r)|^2$ corresponds to the polar representation of the channel gain, with variable changes $x = r\cos\phi$, $y = r\sin\phi$. Similarly, we can approximate the other summation appearing in (21) by

$$\sum_{n=1}^{N} |h_n|^4 \approx A \int_{\phi=0}^{2\pi} \int_{r=0}^{R} |h(r)|^4 r dr d\phi. \tag{23}$$

The following lemma gives close-form approximations for these summations, which can be leveraged to further develop the SNDR expression in (21).

Lemma 4 *Assume we have a LIS with $N \gg 1$ antenna elements with $x_n^2 + y_n^2 < R$, each with effective area A. We can then approximate the summations in* (21) *by*

$$\sum_{n=1}^{N} |h_n|^2 \approx \frac{1}{2}\left(1 - \frac{d}{\sqrt{d^2 + R^2}}\right), \tag{24}$$

$$\sum_{n=1}^{N} |h_n|^4 \approx \frac{A}{32\pi}\left(\frac{1}{d^2} - \frac{d^2}{(d^2 + R^2)^2}\right), \tag{25}$$

and their ratio as

$$\frac{\sum_{n=1}^{N} |h_n|^4}{\sum_{n=1}^{N} |h_n|^2} \approx \frac{A}{16\pi}\left(1 + \frac{d}{\sqrt{d^2 + R^2}}\right)\left(\frac{1}{d^2} + \frac{1}{d^2 + R^2}\right). \tag{26}$$

Proof *See Appendix 8.* □

$$\gamma_{\mathrm{AGC}} \approx \frac{\frac{P}{2}\left|\sum_{k=0}^{L-1}\hat{a}_{2k+1}(k+1)!\right|^2\left(1-\frac{d}{\sqrt{d^2+R^2}}\right)}{P_{\mathrm{distortion}}+\sigma^2}, \tag{27}$$

$$P_{\mathrm{distortion}} = \frac{PA}{16\pi}\left[\sum_{k=1}^{2L-1}\left(k!\sum_{i=1}^{k}\hat{a}_{2i-1}\bar{\hat{a}}_{2k-2i+1}\right)-\left|\sum_{k=0}^{L-1}\hat{a}_{2k+1}(k+1)!\right|^2\right]$$
$$\left(1+\frac{d}{\sqrt{d^2+R^2}}\right)\left(\frac{1}{d^2}+\frac{1}{d^2+R^2}\right).$$

By adopting Lemma 4 and the Bussgang parameters in (13) and (14), we reach the SNDR approximate expression in (27) at the top of this page. This SNDR approximation also applies to the additive distortion model, widely used in the literature [27].

We can also exploit the derived expressions from Lemma 4 to perform an asymptotic analysis when the LIS size grows without bounds, leading to

$$\lim_{R\to\infty}\sum_{n=1}^{N}|h_n|^2 = \frac{1}{2}, \tag{28}$$

$$\lim_{R\to\infty}\frac{\sum_{n=1}^{N}|h_n|^4}{\sum_{n=1}^{N}|h_n|^2} = \frac{A}{16\pi d^2}, \tag{29}$$

and

$$\lim_{R\to\infty}\gamma_{\mathrm{AGC}} = \frac{\frac{1}{2}|\tilde{g}|^2P}{\frac{\kappa PA}{16\pi d^2}+\sigma^2}. \tag{30}$$

The asymptotic channel gain in (28) implies that, for an infinitely large LIS deployed as a plane in front on the UE, the channel gain approaches 0.5, i.e. half of the transmitted power is received by the LIS if there are no losses, in accordance with the law of conservation of energy since half of the space will be covered by an infinitely large LIS. The other two asymptotic results show that, even for an infinitely large LIS, the hardware distortion does not vanish completely. However, we shall see that the hardware distortion may be negligible in some cases, depending on hardware quality.

3.1 The cost of ideal-hardware assumption

In many analytical results and preliminary studies on LIS, e.g. [1], [2], [30], ideal hardware components are assumed. When the LIS is implemented, hard-

ware distortion and other non-ideal effects are unavoidable. However, the performance gap can generally be covered by scaling the LIS, which increases the array gain, allowing higher spatial multiplexing, and causes the uncorrelated hardware distortion to average out. To have a better understanding of the effects of hardware distortion when scaling the LIS, we can study the required number of receive antennas to achieve a minimum performance requirement. In particular, we consider a fixed number of receive antennas with ideal RX-chains and find the minimum number of antennas with non-ideal RX-chains to achieve the same performance. Such analysis may be useful to better understand how much one should scale the system when adopting real-world non-ideal hardware.

For analytical tractability, we mainly focus on the case with perfect per-antenna AGC in this part. Let us first define the ideal-hardware case as the reference point for the analysis. If all the RX-chains are equipped with ideal hardware, i.e. $\kappa = 0$, and the radius of the reception area is $R = R_0$, the SNDR becomes

$$\gamma_0 \approx \frac{P}{2\sigma^2}\left(1 - \frac{d}{\sqrt{d^2 + R_0^2}}\right). \tag{31}$$

We are interested in finding the minimum number of RX-chains, equivalent to the minimum reception radius R, with non-ideal hardware components, i.e. when $\kappa > 0$, to achieve the same level of SNDR as given in (31). From (27), we would like to find the minimum R fulfilling the following inequality

$$\frac{\frac{P|\tilde{g}|^2}{2}\left(1 - \frac{d}{\sqrt{d^2+R^2}}\right)}{\frac{\kappa PA}{16\pi}\left(1 + \frac{d}{\sqrt{d^2+R^2}}\right)\left(\frac{1}{d^2} + \frac{1}{d^2+R^2}\right) + \sigma^2} \geq \gamma_0. \tag{32}$$

Finding the minimum R is in general highly non-trivial. However, low complexity algorithms can effectively approximate the solution to this inequality. An algorithm to solve this problem numerically is introduced in Appendix 9.

Another approach is to define an approximate expression for (32) and find bounds on R. Let us define the distortion power, which is the denominator in (32) excluding the noise power, as

$$\beta = \frac{\kappa PA}{16\pi}\left(1 + \frac{d}{\sqrt{d^2 + R^2}}\right)\left(\frac{1}{d^2} + \frac{1}{d^2 + R^2}\right). \tag{33}$$

The distortion power β is a decreasing function of R, i.e. it reduces if we have more antennas for reception. The minimum and maximum of the distortion

power can be found for $R \to \infty$ and $R = 0$, respectively, as

$$\begin{aligned} \beta_{\min} &= \frac{\kappa P A}{16\pi d^2}, \\ \beta_{\max} &= \frac{\kappa P A}{4\pi d^2}. \end{aligned} \tag{34}$$

To find an upper bound on the minimum R for the inequality (32) to hold, we can consider the worst case scenario, i.e., $\beta = \beta_{\max}$, and rewrite the inequality as

$$\begin{aligned} \left(1 - \frac{d}{\sqrt{d^2 + R^2}}\right) &\geq \frac{\beta_{\max} + \sigma^2}{|\tilde{g}|^2 \sigma^2} \left(1 - \frac{d}{\sqrt{d^2 + R_0^2}}\right) \\ &= \delta_{\max} \left(1 - \Upsilon\right), \end{aligned} \tag{35}$$

where

$$\delta_{\max} = \frac{\beta_{\max} + \sigma^2}{|\tilde{g}|^2 \sigma^2} \tag{36}$$

and

$$\Upsilon = \frac{d}{\sqrt{d^2 + R_0^2}}. \tag{37}$$

The variable $\delta_{\max}$ is a factor containing all the imperfections, i.e., noise, gain compression, and distortion. The upper bound for the minimum R can be calculated as

$$R_{\text{ub}}^2 = d^2 \left(\frac{1}{(1 + \delta_{\max} \Upsilon - \delta_{\max})^2} - 1 \right), \tag{38}$$

which means any $R \geq R_{\text{ub}}$ guarantees that (32) holds.

Similarly, a lower bound on the minimum R can be found by substituting $\beta_{\max}$ for $\beta_{\min}$ in (35), where we can now define $\delta_{\min} = \frac{\beta_{\min} + \sigma^2}{|\tilde{g}|^2 \sigma^2}$ to find

$$R_{\text{lb}}^2 = d^2 \left(\frac{1}{(1 + \delta_{\min} \Upsilon - \delta_{\min})^2} - 1 \right). \tag{39}$$

An important detail to keep in mind in this analysis is the feasibility of fulfilling (32). As an example, imagine that the reference ideal point is selected too optimistic, i.e., $R \gg 0$; then, inequality (32) can not hold even if $R \to \infty$. To formulate feasibility condition, we evaluate (32) for $R \to \infty$, which results in the distortion power to be $\beta = \beta_{\min}$. Therefore, the feasibility of finding an

R to satisfy (32) is equivalent to the feasibility of finding an R that satisfies

$$\left(1 - \frac{d}{\sqrt{d^2 + R^2}}\right) \geq \delta_{\min}\left(1 - \Upsilon\right), \tag{40}$$

which is only possible if $\delta_{\min}\left(1 - \Upsilon\right) \leq 1$, resulting the following condition on R_0,

$$R_0^2 \leq d^2 \left(\frac{\delta_{\min}^2}{(\delta_{\min} - 1)^2} - 1\right). \tag{41}$$

The previous expression thus gives the maximum R_0 for which we can still guarantee the existence of an R fulfilling (32).

4 LIS Antenna Selection

The contribution of each antenna to the signal and distortion power depends on the received power to that individual antenna. Antennas receiving more power may contribute more to the useful signal power at the cost of introducing more distortion. In Section 3, we have seen how the receiver array size, given by the LIS radius, affects the performance of the whole system. We assumed that the area for signal reception was selected as a disk around the center of the array, assuming that UE was also aligned with the central perpendicular line. The question that arises here would be: Can we improve the signal reception performance, i.e. SNDR, by selecting the antennas from another region? In other words, can we get an improvement from considering a reception area with a different shape than a disk with a center aligned with the UE position? This question can be formulated as an antenna selection problem, where we consider a LIS with $N \gg 1$ elements, and a resource constraint which forces the LIS to only use $N_{\max}$ of the antenna elements for signal reception.

If the LIS is restricted to perform MRC on the received signals from the selected antennas, the optimization problem for antenna selection can be formulated as

$$\begin{aligned} \max_{z_1,\ldots,z_N} \quad & \frac{P\sum_{n=1}^{N} z_n \left|\tilde{h}_n\right|^2}{\frac{\sum_{n=1}^{N} z_n C_n \left|\tilde{h}_n\right|^2}{\sum_{n=1}^{N} z_n \left|\tilde{h}_n\right|^2} + \sigma^2}, \\ \text{s.t.} \quad & z_n \in \{0,1\} \quad \forall n \in \{1,\ldots,N\} \\ & \sum_{n=1}^{N} z_n \leq N_{\max}, \end{aligned} \tag{42}$$

where z_n is the binary antenna selection parameter. In general, this problem cannot be solved in closed-form. However, the LIS can perform a simple low-complexity heuristic search to find the optimal solution.

For the case with perfect AGC, we can simplify the optimization problem (42) by exploiting the SNDR approximations from Section 3. Let us consider the setup from Section 2 to simplify this problem. Since the transmitter is located at $(0, 0, d)$, i.e. on the boresight of the LIS, the antennas with the same distance from the center of the array have equal received power. Therefore, if an antenna is in the set of the selected antennas, all the antennas with the same distance from the center should also be in that set unless the maximum number of selected received antennas is reached. This implies that the optimal solution for the selected antennas is in general an annulus, i.e., the region between two concentric circles.

Let us define the set of selected antennas as $\mathcal{F} = \{i \in \mathbb{N} \mid r < x_i^2 + y_i^2 < R\}$. Therefore, we have $z_i = 1$ if $i \in \mathcal{F}$. By leveraging Lemma 4, the following approximation then holds for the numerator in (42),

$$\begin{aligned} P\sum_{n=1}^{N} z_n \left|\tilde{h}_n\right|^2 &= P\left|\tilde{g}\right|^2 \sum_{n\in\mathcal{F}} |h_n|^2 \\ &\approx \frac{Pd\left|\tilde{g}\right|^2}{2}\left(\frac{1}{\sqrt{d^2+r^2}} - \frac{1}{\sqrt{d^2+R^2}}\right), \end{aligned} \tag{43}$$

and for the denominator, we have

$$\begin{aligned} &\frac{\sum_{n=1}^{N} z_n C_n \left|\tilde{h}_n\right|^2}{\sum_{n=1}^{N} z_n \left|\tilde{h}_n\right|^2} = \frac{P\kappa \sum_{n\in\mathcal{F}} |h_n|^4}{\sum_{n\in\mathcal{F}} |h_n|^2} \\ &\approx \frac{P\kappa dA}{16\pi}\left(\frac{1}{\sqrt{d^2+r^2}} + \frac{1}{\sqrt{d^2+R^2}}\right)\left(\frac{1}{d^2+r^2} + \frac{1}{d^2+R^2}\right), \end{aligned} \tag{44}$$

where $\tilde{g}$ and κ are given in (13) and (14). By exploiting the above approximations, the optimization problem (42) converts to

$$\begin{aligned} \max_{r,R} \; & \frac{\frac{Pd|\tilde{g}|^2}{2}\left(\frac{1}{\sqrt{d^2+r^2}} - \frac{1}{\sqrt{d^2+R^2}}\right)}{\frac{P\kappa dA}{16\pi}\left(\frac{1}{\sqrt{d^2+r^2}} + \frac{1}{\sqrt{d^2+R^2}}\right)\left(\frac{1}{d^2+r^2} + \frac{1}{d^2+R^2}\right) + \sigma^2}, \\ \text{s.t.} \; & r, R \geq 0 \\ & \pi(R^2 - r^2) \leq N_{max} A \end{aligned} \tag{45}$$

which has the benefit of being a continuous function of only two variables, and

it has a reduced complexity over (42) when solved by numerical methods. An algorithm to solve this problem numerically is introduced in Appendix 9.

5 LIS Panel Selection

The analysis so far was based on the assumption that LISs are going to be implemented as very large surfaces with $N \gg 1$ antennas equally spaced on a plane, e.g., a wall or a ceiling of a building. As mentioned earlier, this is a common vision for LIS implementations in future wireless networks. However, it may be impractical when considering current base station technologies, e.g., massive MIMO. A more favorable option, without losing practicality and cost-efficiency, is to implement LIS as a grid of N_{p} distributed panels, each equipped with M uniformly spaced antennas. Therefore, we extend our previous results to a panel-based LIS scenario.

Let us assume that $M \ll N_{\mathrm{p}}$ and the UE is far enough to be the far-field for each panel such that the channel gain amplitude $|h_n|^2$ has a negligible variation for all the antenna elements on each panel, and the only significant change across the panel is carried in the phase. Therefore, the SNDR after applying MRC is given by

$$\gamma = \frac{PM \sum_{n=1}^{N_{\mathrm{p}}} |\tilde{h}_n|^2}{\frac{\sum_{n=1}^{N_{\mathrm{p}}} C_n |\tilde{h}_n|^2}{\sum_{n=1}^{N_{\mathrm{p}}} |\tilde{h}_n|^2} + \sigma^2}, \tag{46}$$

where $|\tilde{h}_n|$ and C_n correspond to the channel gain and the distortion power for all the antennas from the n'th panel. By comparing (46) and (18), we can see that they look the same except for the panel array-gain factor M. However, we should note that $|\tilde{h}_n|$ has a slightly different meaning now since it corresponds to the common channel gain of the whole panel instead of the channel gain for each antenna. Nevertheless, we expect a similar behavior in performance when scaling this type of LIS.

Taking into account (46), we can transform the antenna selection problem in (42) into a panel selection problem

$$\begin{aligned} \max_{z_n} \ & \frac{PM \sum_{n=1}^{N_p} z_n \left|\tilde{h}_n\right|^2}{\frac{\sum_{n=1}^{N_p} z_n C_n \left|\tilde{h}_n\right|^2}{\sum_{n=1}^{N_p} z_n \left|\tilde{h}_n\right|^2} + \sigma^2}, \\ & \text{s.t.} \quad z_n \in \{0,1\} \qquad n \in \{1,...,N\} \\ & \sum_{n=1}^{N_p} z_n \leq N_{\max} \end{aligned} \tag{47}$$

where the binary variable z_n determines if the n'th panel is active or not, and $N_{\max} \leq N_{\mathrm{p}}$ is the maximum number of panels that can be selected for signal decoding. This panel selection problem can also be interpreted as the original antenna selection problem after grouping the antenna elements on the LIS into a grid of rectangular panels.

While performing a heuristic search to solve (47) has reasonable complexity, it may still be beneficial, from a practical point of view, to consider closed-form sub-optimal solutions for specific cases. Such closed-form solutions can also provide some intuition about how to optimize the design of LIS architectures, e.g., for defining suitable panel placement strategies. For analytical tractability, we will focus on the 3rd order non-linear model, i.e., where the hardware model is given by (4), with $L = 2$, which retains much of the practicality since the 3rd order non-linearity is known to be the dominant source of in-band hardware distortion [23], [25]. Nevertheless, in case higher orders of non-linearity are of interest, one can fit the higher order model to a 3rd order model and adopt our proposed solution with the cost of a marginal deviation from the optimum.

Let us start with the case where only one panel is selected, i.e., $N_{\max} = 1$. In this case, the panel selection problem boils down to optimizing the input power for a SISO scenario. The reason is that we can find the optimum input power for the SISO scenario and select the panel with the closest input power to that optimum value. In the general case, where $N_{\max} \geq 1$, the LIS can simply select the $N_{\max}$ panels with the input power closest to the optimum value. Therefore, finding the optimum input power for the SISO case is of great importance. For a SISO scenario where a symbol $s \sim \mathcal{CN}(0, P)$ is transmitted over the channel $h \in \mathbb{C}$, the input to the RX-chain will be $x \sim \mathcal{CN}(0, \rho)$, where $\rho = P|h|^2$. If the receiver RX-chain has a 3rd order non-linearity as described above, from (9) and (10), the SNDR may be expressed as

$$\gamma_{\mathrm{SISO}} = \frac{|a_1 + 2a_3\rho|^2\rho}{2|a_3|^2\rho^3 + \sigma^2}. \tag{48}$$

As previously motivated, we are interested in solving the optimization problem

$$\begin{aligned} \max_{\rho} \ & \frac{|a_1 + 2a_3\rho|^2\rho}{2|a_3|^2\rho^3 + \sigma^2}, \\ \text{s.t.} \ \ & 0 < \rho < \rho_{\max} \end{aligned} \tag{49}$$

where $\rho_{\max}$ is the maximum expected received power, which is imposed by the specific scenario. Note that the optimization variable ρ can be altered either by adjusting P, e.g., via power control, or $|h|^2$, e.g., via UE movements or panel selection. Since we are interested in this problem only for the purpose of panel selection, the transmit power is assumed to be fixed, while $|h|^2$ can be

controlled by selecting different panels across the LIS.

The optimization problem (49) is concave and finding its optimal solution in the current format, involves solving a 5th order equation after taking the first derivative. However, we can try to find a suitable approximation for the numerator and simplify the objective function. For example, we can approximate the term $|a_1 + 2a_3\rho|^2$ in the numerator as a linear function of ρ, $\alpha + \beta\rho$, for $0 < \rho < \rho_{\max}$. According to (11), we have $a_1 = \hat{a}_1$ and $a_3 = \hat{a}_3/\rho_{\max}$, which gives approximation parameters $\alpha = |\hat{a}_1|^2$ and

$$\beta = \frac{|\hat{a}_1 + 2\hat{a}_3|^2 - |\hat{a}_1|^2}{\rho_{\max}}. \tag{50}$$

Applying the above approximation and taking the first derivative of the approximate SNDR, we end up with the 4th order equation

$$2\beta|a_3|^2\rho^4 + 4\alpha|a_3|^2\rho^3 - 2\beta\sigma^2\rho - \alpha\sigma^2 = 0. \tag{51}$$

Considering amplifier characterizations from [26], we note that the factor $2\beta|\hat{a}_3|^2$ is much smaller than other factors in the equation. Therefore, we approximate (51) by

$$\rho^3 - \frac{\beta\sigma^2}{2\alpha|a_3|^2}\rho - \frac{\sigma^2}{4|a_3|^2} = 0, \tag{52}$$

which is a depressed cubic equation $\rho^3 + c_1\rho + c_0 = 0$ with

$$c_0 = -\frac{\sigma^2}{4|a_3|^2} \tag{53}$$

and

$$c_1 = -\frac{\beta\sigma^2}{2\alpha|a_3|^2}. \tag{54}$$

According to Cardano's formula [31], and since $\Delta = c_0^2/4 + c_1^3/27$ is positive, this equation has only one real solution given by

$$\rho_{\text{opt}} = \sqrt[3]{-\frac{c_0}{2} + \sqrt{\Delta}} + \sqrt[3]{-\frac{c_0}{2} - \sqrt{\Delta}}. \tag{55}$$

The numerical results in Section 6 indicate a high accuracy in the approximation. Hence, (55) provides a suitable closed-form approximate solution to the panel selection problem.

6 Numerical Results

In this section, we provide numerical examples to gain more insights about the aforementioned methods and derivations. As performance metric, we consider a lower bound on the spectral efficiency given by $R_{\mathrm{a}} = \log_2(1+\gamma)$, which corresponds to an achievable rate. This achievable rate comes from assuming a Gaussian additive distortion term in the Bussgang decomposition, corresponding to the worst case scenario [32]. The UE is assumed to be at distance $d = 25\lambda$ from the center of LIS transmitting with transmit power P such that SNR$= 10dB$ at the center of LIS. The gray areas in all the figures in this section illustrate the range of parameters for which the UE is in far-field of the LIS. For the hardware distortion model, we use the measurements from one of the 3GPP reports [26], which also estimates the parameters for the memory-less polynomial model (4) based on real-world RF hardware at different frequencies and bandwidths. To have a better understanding of the difference in hardware distortion effects for different RF components, we have employed (13) and (14) to calculate $\tilde{g}$ and κ based on a range of measurements in [26], which have been performed at the frequencies 2.1 GHz and 28 GHz, for GaA, CMOS, and GaN amplifiers. Table 1 summarizes the results. Note that, for ideal hardware, we would have $|\tilde{g}|^2 = 1$ and $\kappa = 0$.

Type	Freq.	BW	BO	κ	$\lvert\tilde{g}\rvert^2$
GaA	2.1 GHz	40 MHz	10 dB	0.208	0.937
CMOS	28 GHz	400 MHz	10 dB	0.252	0.894
GaN	2.1 GHz	40 MHz	8 dB	0.035	0.811
GaN	28 GHz	400 MHz	8 dB	0.132	0.884

Table 1: Examples of Hardware Distortion Parameters in (13) and (14) for different amplifier types at specific frequencies, bandwidth(BW), and back-off (BO).

6.1 Scaling Analysis Example

We begin with studying the scaling performance of LISs for different levels of hardware distortion. Let us consider the model based on a Gallium Nitride (GaN) amplifier designed for operation at 2.1 GHz as a case study, where the model parameters have been estimated from input-output measurements at a sample rate of 200 MHz and a signal bandwidth of 40 MHz. We would have similar results and conclusions if we select another data set from [26] and table 1. The report provides the coefficients for normalized inputs, i.e., $\hat{a}_{2k+1}$ in (11) and (12), for 3rd, 5th, 7th, and 9th order non-linearity. We consider a discrete LIS with antenna elements separated by $\lambda/2$ on a rectangular grid.

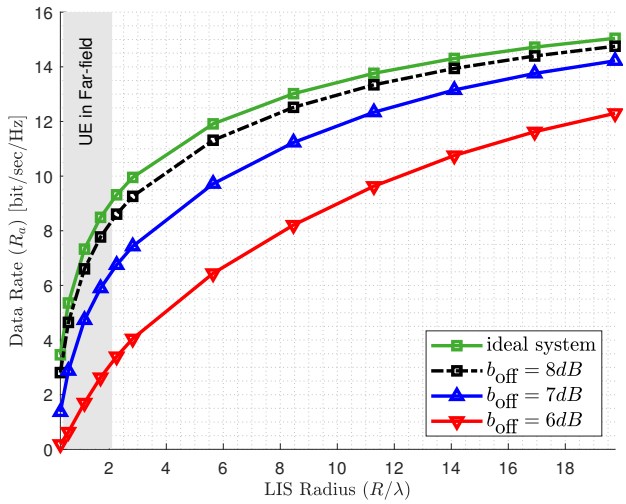

Figure 3: Achievable data rate vs LIS radius in terms of λ. The UE is at distance $d = 25\lambda$ from the center of LIS.

In Fig. 3, we illustrate the achievable rate R_{a} for different levels of back-off in (11). By comparing our results to the performance of an ideal system, we can see that the hardware distortion can degrade the system performance significantly even if we use 7 dB of back-off, which is a typical value for low-power receivers. One should also note that for a sufficiently large back-off, e.g. 8 dB or higher, the performance approaches the ideal case at the cost of low energy efficiency in the RF amplifiers, which is not favorable, especially in LIS scenarios. Since the case with 8 dB has a similar performance to the ideal case, we only focus on the lower back-off values from now on.

In Fig. 4 we consider the case with perfect per-antenna AGC, where we plot the achievable rate for different levels of back-off. So as to evaluate the approximation error for the proposed close-form expressions, we consider both the closed-form expression and the exact numerical values. Firstly, we can see that the close-form approximations overlap closely with the numerical values, which means the approximations are valid and can be used for analytical results with very low approximation error. Secondly, we can see that similar to Fig. 3 which was without per-antenna perfect AGC, the hardware distortion degrades the system performance significantly, which implies that hardware distortion may potentially limit the performance in LIS scenarios no matter if we have perfect AGC or not.

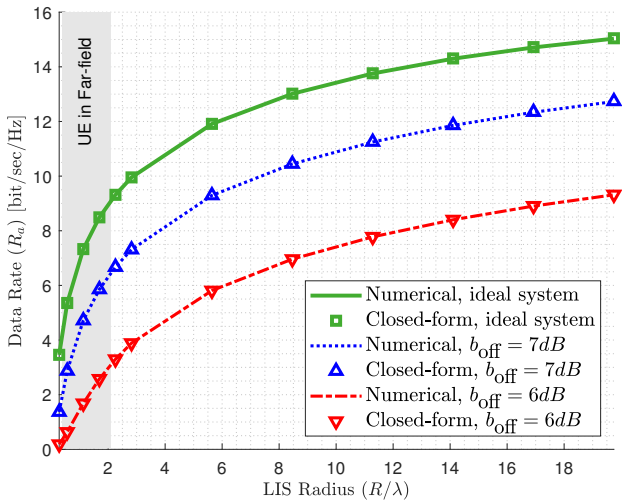

Figure 4: Numerical and Closed-form achievable data rate with perfect AGC vs LIS radius in terms of λ. The UE is at distance $d = 25\lambda$ from the center of LIS.

6.2 Antenna and Panel selection

In Fig. 5, the performance of using the proposed optimal antenna selection in comparison to using the dominant antennas, i.e. antennas with highest received power, is illustrated. We have used the 9th order distortion model for a GaN amplifier at 2.1 GHz, as described in the previous section, with a 7 dB of back-off. The UE transmit power is again selected such that the SNR at the center of LIS reaches 10 dB, which corresponds to the respective value of $P_{\max}$ in (11). We also assume that $N_{\max} = \lceil 0.1N \rceil$ is selected as the antenna selection constraint. As we can see in Fig. 5, adopting the optimal antenna selection can improve the system performance significantly for medium to large LIS radius. We can also see that the gain from adopting antenna selection is negligible if the UE is in the far-field of the LIS.

In Fig. 6 we have illustrated the performance of panel-based LIS when adopting the proposed optimal panel selection versus the baseline approach corresponding to performing dominant panel selection, for different number of panels. The panel selection constraint in (47) is set to $N_{\max} = \lceil 0.1N \rceil$. We also assume that each panel consists of $M = 16$ antennas with $\lambda/2$ spacing, and the distance between the centers of adjacent panels is set to $\delta_p = 5\lambda$. The same distortion model as in Fig. 5 is used for each antenna element of the LIS panels. We can see that there is a significant gain from applying the proposed optimal panel selection. In comparison to the results from Fig. 5 for antenna selection, the achievable performance gains are much higher, which implies that in the practical case of panel-based LIS deployment, it is even more important

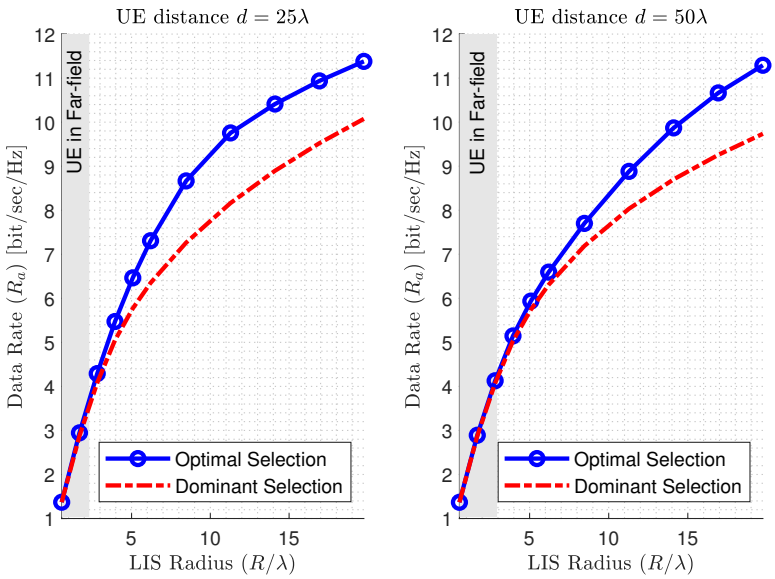

Figure 5: Achievable data rate with perfect AGC vs LIS radius in terms of λ with fixed back-off for optimal antenna selection solved from (42) and dominant antenna selection where the antennas with highest received power are selected.

to consider the panel selection schemes in the presence of hardware distortion.

For panel-based LIS and as previously mentioned, we have assumed that the UE is in the far-field of each panel such that we can simplify the panel selection problem into (46). To illustrate the validity of this assumption in this section, we need to compare the distance between the closest and furthest antenna elements on each panel to the UE, which are denoted by d_1 and d_2 respectively. In Fig. 7, we have compared the maximum ratio of these distances for the panel-based LIS scenario as described above. We can see that the far-field assumption for individual panels holds for $d = 25\lambda$ and beyond, which is the case we have considered in this section.

In Fig. 8, we have evaluated the performance of the approximate closed-form solution to the panel selection problem in comparison to the numerical optimal solution and the dominant panel selection. We have used the 3rd order non-linearity model for the hardware distortion as motivated in section 5. The panel selection constraint and panel placement is the same as in Fig. 6. As we see, the optimal panel selection and closed-form panel selection outperform the dominant panel selection significantly, and the close-form panel selection performance is very close to the numerical optimal method, which implies that the proposed close-form solution is accurate enough to use in LIS panel selection

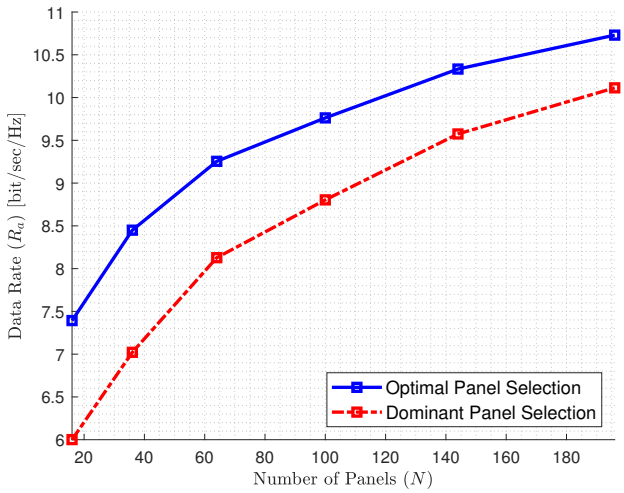

Figure 6: Achievable data rate with perfect AGC vs number of panels with fixed back-off for optimal panel selection solved from (47) and dominant panel selection. The UE is at distance $d = 25\lambda$ from the center of LIS, the panel selection constraint in (47) is $N_{\max} = \lceil 0.1N \rceil$, and Each panel consists of $M = 16$ antennas with $\lambda/2$ spacing. The distance between the centers of adjacent panels is $\delta_p = 5\lambda$.

problems with hardware distortion. In Fig. 9, we compare the performance gain of adopting such schemes for 3 different distance of the UE. We can see that the gain is higher if the UE is more into the near-field of the LIS, and it is still significant if the UE is placed at further distances. The results from Fig. 5, 6, 8, and 9 show that we can improve the system performance by performing the proposed antenna and panel selection without using more resources in terms of extra antennas and panels. This implies that the proposed selection methods can improve the system energy efficiency (EE) which is favorable when scaling up LIS systems for future generations of wireless networks.

To have a better understanding of the importance of panel selection in LIS applications, we simulate a practical panel-based LIS deployment scenario where a panel-based LIS consisting of 4×4 panels covers the ceiling of a $7m\times7m$ room. The carrier frequency is set to 2.1 GHz to match the hardware distortion measurements for the GaN amplifier from [26]. The distance between panels is 5λ, the antenna spacing is $\lambda/2$, and the panel selection constraint is set to $N_{\max} = \lceil 0.1N \rceil$. With these setup parameters, there are in total $N = 81$ panels covering the ceiling and the selection schemes allocate $N_{\max} = 9$ panels to serve the UE, which is randomly located at the bottom of the room. We consider three different room heights, $3.57m$, $7.14m$ and $10.71m$, corresponding to perpendicular distance of 25λ, 50λ, and 75λ, between the UE and LIS, respectively. In Fig. 10, we compare the CDF of the achievable rate for the

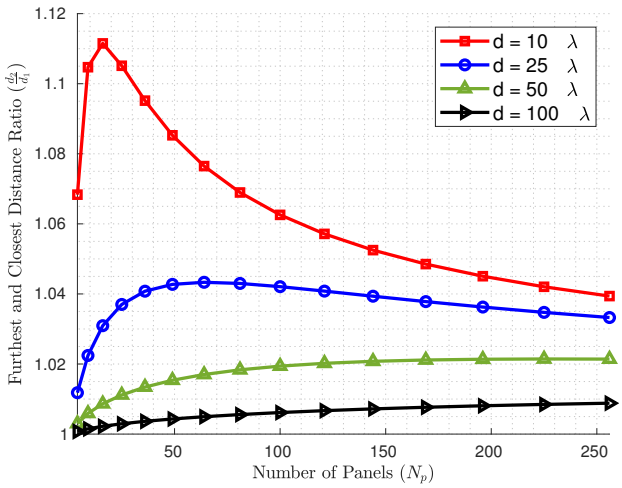

Figure 7: The maximum ratio between the furthest and closest antenna element on each panel to the UE vs the number of panels, for different distances of the UE to the center of LIS.

case where the proposed optimal panel selection is adopted in comparison to the case where the dominant panels are assigned to the UE. We can see that for this scenario with typical setup parameters of a LIS indoor application, the gain from adopting the proposed panel selection is significant, and the LIS can provide a higher data rate with high probability just by adopting our proposed panel selection. We can also see that the data rate becomes worse in buildings with higher ceiling if the dominant panel selection is used, while the proposed panel selection can make the data rate more stable and higher, no matter if the ceiling is high or low.

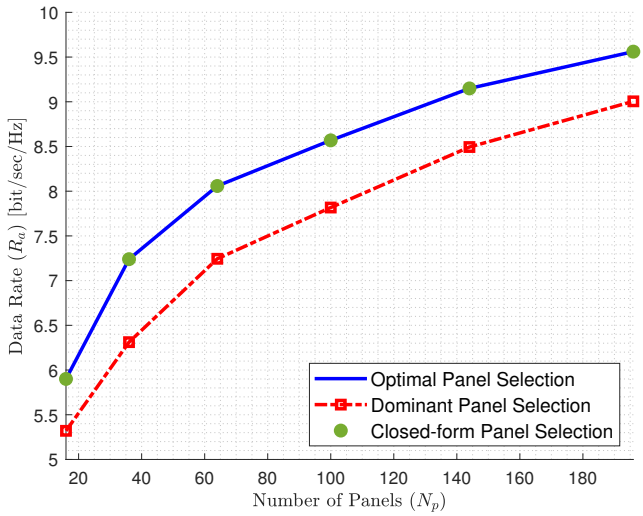

Figure 8: Achievable data rate vs number of panels with fixed back-off for optimal panel selection solved from (47), close-form panel selection in (55), and dominant panel selection. The setup parameters are the same as Fig. 6.

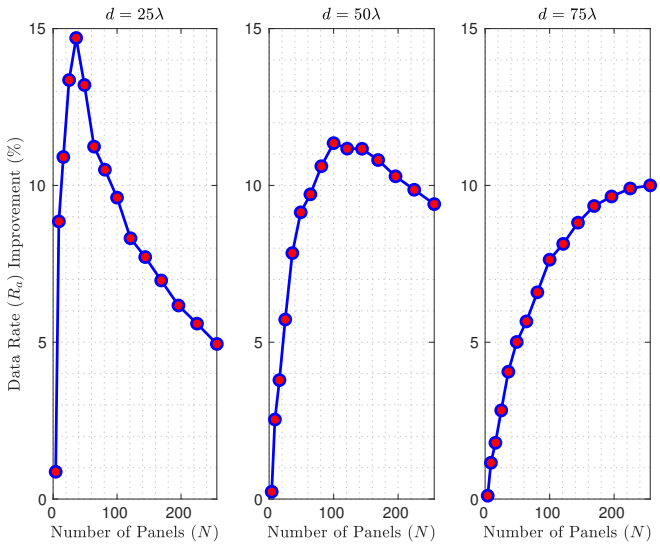

Figure 9: Percentage achievable data rate improvement for different UE distances with fixed back-off for optimal panel selection and dominant panel selection. The setup parameters are the same as Fig. 6.

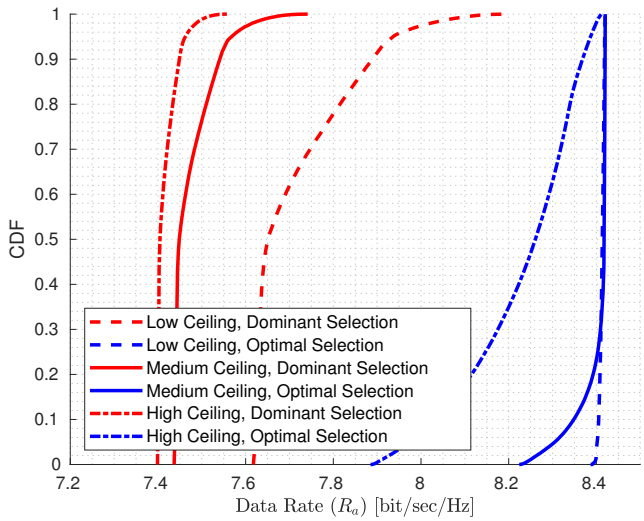

Figure 10: CDF of achievable data rate with fixed back-off for optimal panel selection and dominant panel selection for randomly located UE in a $7m \times 7m$ room with different ceiling heights. Low, medium, and high ceiling, corresponding to perpendicular distance of 25λ, 50λ, and 75λ, between the UE and LIS, respectively. Other setup parameters are the same as Fig. 6.

6.3 Distortion Correlation

As remarked in Section 3, the distortion covariance matrix $\boldsymbol{C}_{\boldsymbol{\eta\eta}}$ is in general non-diagonal, and assuming it diagonal, i.e., disregarding the correlation, results in an over-estimation of the SNDR. In this section, we study the impact of disregarding the distortion correlation on the scaling behavior and on the performance of the panel selection schemes. Assuming a 3rd order non-linearity model, i.e. $L = 2$, for the non-linearity model in (4), the non-diagonal distortion covariance matrix elements are given by

$$[\boldsymbol{C}_{\boldsymbol{\eta\eta}}]_{ij} = 2a_{3,i}\bar{a}_{3,j}|\rho_{ij}|^2\rho_{ij}, \tag{56}$$

where $\rho_{ij} = \mathbb{E}\{x_i\bar{x}_j\}$, and x_i is the input signal to the i'th antenna. While characterizing the non-diagonal elements of $\boldsymbol{C}_{\boldsymbol{\eta\eta}}$ for higher order non-linearities is beyond the scope of this paper, we expect the 3rd order case to capture the main impact of disregarding distortion correlation.

In Fig. 11, we have analyzed the scaling behavior of LIS by comparing the achievable rate R_{a} for different levels of back-off, both with and without considering the distortion correlation. The transmit power is selected such that SNR = 0 dB at the center of the LIS. We can see that as we scale up the LIS, the impact of disregarding the distortion grows progressively. However,

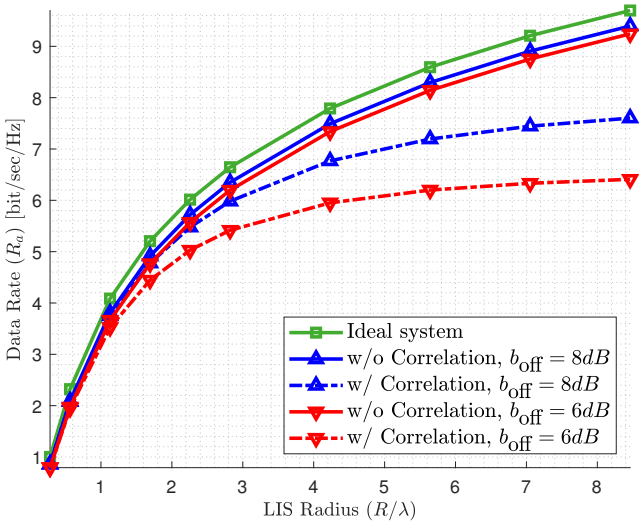

Figure 11: Achievable data rate vs LIS radius in terms of λ, with and without considering distortion correlation. The UE is at distance $d = 25\lambda$ from the center of LIS.

for reasonably large LISs, the impact is still quite limited. On the other hand, taking into account the distortion correlation will only strengthen the important finding that hardware distortion has a significant impact on the performance of scaled-up LIS systems.

In Fig. 12 we analyze the performance of the panel selection schemes when these are either aware or unaware of the distortion correlation. For that purpose, we have plotted the achievable data rate with hardware distortion correlation for three cases: dominant panel selection, sub-optimal panel selection which performs the panel selection unaware of the distortion correlation, and the optimal panel selection which takes into account the distortion correlation for panel selection. All the simulation parameters are the same as in Fig. 8. We can see that, although Fig. 11 shows that disregarding distortion correlation can result in considerable over-estimation of the data rate, this approximation can be leveraged for low-complexity panel selection, still resulting in close-to-optimum performance and significant gain compared to the baseline approach.

7 Conclusion

In this paper, we have studied the impact of hardware distortion when considering LIS implementations with non-ideal RX-chains. We have derived analytical

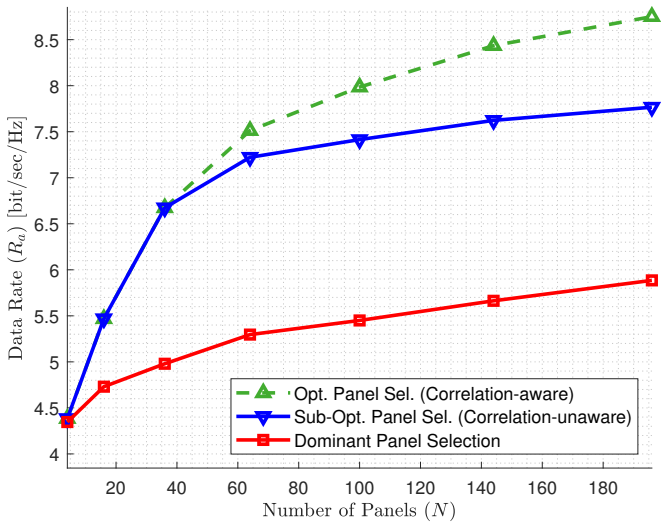

Figure 12: Achievable data rate with distortion correlation vs number of panels. The UE is at distance $d = 25\lambda$ from the center of LIS, the panel selection constraint in (47) is $N_{\max} = \lceil 0.1N \rceil$, and Each panel consists of $M = 16$ antennas with $\lambda/2$ spacing. The distance between the centers of adjacent panels is $\delta_p = 5\lambda$.

expressions for the SNDR considering the memory-less polynomial model for non-ideal hardware at the RX-chains. Such expressions enabled us to evaluate the performance of the LIS with hardware distortion when scaling up the system. We observe that the hardware quality can effectively limit the system performance even for extremely large LISs. We have also proposed antenna selection schemes for LIS and we have shown that adopting such schemes can improve the performance significantly. We also consider a more practical case where the LIS is deployed as a grid of multi-antenna panels, and define panel selection problems to improve the system performance. For the special case of 3rd-order nonlinear model, we have introduced a close-form panels selection solution, which can be exploited to efficiently switch panels with near-optimum performance.

8 Proof of Lemmas

Proof of Lemma 3

Considering the memory-less polynomial model (4) with $x_{\text{in}} \sim \mathcal{CN}(0, P)$, we first calculate $\mathbb{E}\left[y_{\text{out}}\bar{x}_{\text{in}}\right]$ as

$$\begin{aligned}\mathbb{E}\left[y_{\text{out}}\bar{x}_{\text{in}}\right] &= \mathbb{E}\left[\sum_{k=0}^{L-1} a_{2k+1}x_{\text{in}}|x_{\text{in}}|^{2k}\bar{x}\right] \\ &= \sum_{k=0}^{L-1} a_{2k+1}\mathbb{E}\left[|x_{\text{in}}|^{2(k+1)}\right], \end{aligned} \tag{57}$$

where the term $|x_{\text{in}}|^2$ is a Rayleigh variable, with $\mathbb{E}|x_{\text{in}}|^2 = P$. The $(k+1)$'th moment of this Rayleigh variable is given by

$$\mathbb{E}\left[|x_{\text{in}}|^{2(k+1)}\right] = P^{k+1}\Gamma\left[1+(k+1)\right] = P^{k+1}(k+1)!, \tag{58}$$

which can be replaced in (57) to find g as

$$g = \frac{\mathbb{E}\left[y_{\text{out}}\bar{x}_{\text{in}}\right]}{\mathbb{E}\left[|x_{\text{in}}|^2\right]} = \sum_{k=0}^{L-1} a_{2k+1}(k+1)!\ P^k. \tag{59}$$

In order to find C_η, we need to calculate $C_{y_{\text{out}}}$, which is given by

$$\mathbb{E}\left[y_{\text{out}}\bar{y}_{\text{out}}\right] = \mathbb{E}\left[\sum_{m=0}^{L-1} a_{2m+1}x_{\text{in}}|x_{\text{in}}|^{2m}\sum_{n=0}^{L-1}\bar{a}_{2n+1}\bar{x}_{\text{in}}|x_{\text{in}}|^{2n}\right]. \tag{60}$$

We can simplify it using a change of variable and considering the moments of a Rayleigh variable to get

$$\mathbb{E}\left[y_{\text{out}}\bar{y}_{\text{out}}\right] = \sum_{k=1}^{2L-1}\left(k!\ P^k\sum_{i=1}^{k} a_{2i-1}\bar{a}_{2k-2i+1}\right). \tag{61}$$

Proof of Lemma 4

From (22) and (23), we need to calculate the following integrals,

$$\frac{d}{2}\int_{r=0}^{R}\frac{1}{(d^2+r^2)^{\frac{3}{2}}}rdr, \tag{62}$$

$$\frac{d^2}{8\pi}\int_{r=0}^{R}\frac{1}{(d^2+r^2)^{3}}rdr, \tag{63}$$

where we have simplified the phase part with a 2π factor before the integrals. By a change in variable as, $x = r^2$ and $rdr = \frac{1}{2}dx$, while using the following indefinite integral formulas,

$$\int\frac{1}{(d^2+x)^{\frac{3}{2}}}dx = \frac{-2}{\sqrt{d^2+x}}, \tag{64}$$

$$\int\frac{1}{(d^2+x)^{3}}dx = \frac{-\frac{1}{2}}{(d^2+x)^{2}}, \tag{65}$$

we can find the results in (24) and (25), and a simple factorization gives (26).

9 Algorithms

Algorithm 1 provides a simple low-complexity numerical method to solve (32), where the accuracy of the solution depends on the number of iterations, T.

Algorithm 1 Numerical Method to solve (32)

Define: $R_{\text{ub}} = (38)$, $R_{\text{lb}} = (39)$, $\Delta = R_{\text{ub}} - R_{\text{lb}}$, $R_{\text{opt}} = R_{\text{lb}}$, $R_{\text{new}} = R_{\text{lb}}$, $T \in \mathcal{N}$ where $T >> 1$.

for $t = 1$ to T:
  Calculate γ from (32) for $R = R_{\text{new}}$
  if $\gamma \geq \gamma_0$:
    $R_{\text{opt}} = R_{\text{new}}$
    break
  else:
    $R_{\text{new}} = R_{\text{lb}} + \frac{t}{T}\Delta$
  endif
endfor

Algorithm 2 can be used to find a sub-optimal solution to the optimization problem (45). By selecting a sufficiently large value for T, the sub-optimal solution from this algorithm can approach the optimal solution.

Algorithm 2 Sub-Optimal Solution to Problem (45)

Define: $\tilde{R} = NA/\pi$, $r_0 = 0$, $R_0 = \sqrt{N_{\max}A/\pi}$, $\gamma_0 = (27)$ with $R = R_0$, $r_{\text{opt}} = 0$, $R_{\text{opt}} = R_0$, $\gamma_{\text{opt}} = \gamma_0$, $T \in \mathcal{N}$ where $T >> 1$.

for $t = 1$ to T:

$r_{\text{new}} = \frac{t}{T}\sqrt{\tilde{R}^2 - N_{\max}A/pi}$,

$R_{\text{new}} = \sqrt{N_{\max}A/\pi + r_{\text{opt}}^2}$,

$\gamma_{\text{new}} = (45)$ with $r = r_{\text{new}}$ and $R = R_{\text{new}}$,

if $\gamma < \gamma_{\text{opt}}$:

break

else:

$r_{\text{opt}} = r_{\text{new}}$,

$R_{\text{opt}} = R_{\text{new}}$,

$\gamma_{\text{opt}} = \gamma_{\text{new}}$,

endif

endfor

References

[1] S. Hu, F. Rusek, and O. Edfors, "Beyond massive MIMO: The potential of data transmission with large intelligent surfaces," *IEEE Transactions on Signal Processing*, vol. 66, no. 10, pp. 2746–2758, 2018.

[2] S. Hu, F. Rusek, and O. Edfors, "Beyond massive MIMO: The potential of positioning with large intelligent surfaces," *IEEE Transactions on Signal Processing*, vol. 66, no. 7, pp. 1761–1774, 2018.

[3] C. Huang et al., "Holographic MIMO surfaces for 6g wireless networks: Opportunities, challenges, and trends," *IEEE Wireless Communications*, vol. 27, no. 5, pp. 118–125, 2020.

[4] E. Björnson and L. Sanguinetti, "Power scaling laws and near-field behaviors of massive MIMO and intelligent reflecting surfaces," *IEEE Open Journal of the Communications Society*, vol. 1, pp. 1306–1324, 2020.

[5] A. Pizzo, A. d. J. Torres, L. Sanguinetti, and T. L. Marzetta, "Nyquist sampling and degrees of freedom of electromagnetic fields," *IEEE Transactions on Signal Processing*, vol. 70, pp. 3935–3947, 2022.

[6] A. Pereira, F. Rusek, M. Gomes, and R. Dinis, "Deployment strategies for large intelligent surfaces," *IEEE Access*, vol. 10, pp. 61 753–61 768, 2022.

[7] J. V. Alegría and F. Rusek, "Achievable rate with correlated hardware impairments in large intelligent surfaces," in *2019 IEEE 8th International Workshop on Computational Advances in Multi-Sensor Adaptive Processing (CAMSAP)*, 2019, pp. 559–563.

[8] C. Pan et al., "An overview of signal processing techniques for RIS/IRS-aided wireless systems," *IEEE Journal of Selected Topics in Signal Processing*, vol. 16, no. 5, pp. 883–917, 2022.

[9] A. Papazafeiropoulos, C. Pan, P. Kourtessis, S. Chatzinotas, and J. M. Senior, "Intelligent reflecting surface-assisted MU-MISO systems with imperfect hardware: Channel estimation and beamforming design," *IEEE Transactions on Wireless Communications*, vol. 21, no. 3, pp. 2077–2092, 2022.

[10] Z. Xing, R. Wang, J. Wu, and E. Liu, "Achievable rate analysis and phase shift optimization on intelligent reflecting surface with hardware impairments," *IEEE Transactions on Wireless Communications*, vol. 20, no. 9, pp. 5514–5530, 2021.

[11] Z. Chu et al., "RIS assisted wireless powered IoT networks with phase shift error and transceiver hardware impairment," *IEEE Transactions on Communications*, vol. 70, no. 7, pp. 4910–4924, 2022.

[12] E. G. Larsson, O. Edfors, F. Tufvesson, and T. L. Marzetta, "Massive MIMO for next generation wireless systems," *IEEE Communications Magazine*, vol. 52, no. 2, pp. 186–195, 2014.

[13] F. Rusek et al., "Scaling up MIMO: Opportunities and challenges with very large arrays," *IEEE Signal Processing Magazine*, vol. 30, no. 1, pp. 40–60, 2013.

[14] C. Mollén, U. Gustavsson, T. Eriksson, and E. G. Larsson, "Impact of spatial filtering on distortion from low-noise amplifiers in massive MIMO base stations," *IEEE Transactions on Communications*, vol. 66, no. 12, pp. 6050–6067, 2018.

[15] H. Zhao, J. C. G. Diaz, and S. Hoyos, "Multi-channel receiver nonlinearity cancellation using channel speculation passing algorithm," *IEEE Transactions on Circuits and Systems II: Express Briefs*, vol. 69, no. 2, pp. 599–603, 2022.

[16] J. Marttila, M. Allén, M. Kosunen, K. Stadius, J. Ryynänen, and M. Valkama, "Reference receiver enhanced digital linearization of wideband direct-conversion receivers," *IEEE Transactions on Microwave Theory and Techniques*, vol. 65, no. 2, pp. 607–620, 2017.

[17] M. Sarajlić, A. Sheikhi, L. Liu, H. Sjöland, and O. Edfors, "Power scaling laws for radio receiver front ends," *IEEE Transactions on Circuits and Systems I: Regular Papers*, vol. 68, no. 5, pp. 2183–2195, 2021.

[18] A. Sheikhi, F. Rusek, and O. Edfors, "Massive MIMO with per-antenna digital predistortion size optimization: Does it help?" In *ICC 2021 - IEEE International Conference on Communications*, 2021, pp. 1–6.

[19] A. Sheikhi and O. Edfors, "Machine learning based digital pre-distortion in massive MIMO systems: Complexity-performance trade-offs," in *2023 IEEE Wireless Communications and Networking Conference (WCNC)*, 2023, pp. 1–6.

[20] S. Hu, H. Wang, and M. C. Ilter, "Design of near-field beamforming for large intelligent surfaces," *IEEE Transactions on Wireless Communications*, vol. 23, no. 1, pp. 762–774, 2024.

[21] H. Tataria, F. Tufvesson, and O. Edfors, "Real-time implementation aspects of large intelligent surfaces," in *ICASSP 2020 - 2020 IEEE International Conference on Acoustics, Speech and Signal Processing (ICASSP)*, 2020, pp. 9170–9174.

[22] J. Rodríguez Sánchez, F. Rusek, O. Edfors, and L. Liu, "Distributed and scalable uplink processing for LIS: Algorithm, architecture, and design trade-offs," *IEEE Transactions on Signal Processing*, vol. 70, pp. 2639–2653, 2022.

[23] O. T. Demir and E. Björnson, "Channel estimation in massive MIMO under hardware non-linearities: Bayesian methods versus deep learning," *IEEE Open Journal of the Communications Society*, vol. 1, pp. 109–124, 2020.

[24] O. T. Demir and E. Björnson, "The Bussgang decomposition of nonlinear systems: Basic theory and MIMO extensions [lecture notes]," *IEEE Signal Processing Magazine*, vol. 38, no. 1, pp. 131–136, 2021.

[25] T. Schenk, *RF imperfections in high-rate wireless systems: impact and digital compensation*. Springer Science & Business Media, 2008.

[26] "Further elaboration on PA models for NR," *document 3GPP TSG-RAN WG4, R4-165901, Ericsson, Stockholm, Sweden*, Aug. 2016.

[27] E. Björnson, J. Hoydis, M. Kountouris, and M. Debbah, "Massive MIMO systems with non-ideal hardware: Energy efficiency, estimation, and capacity limits," *IEEE Transactions on Information Theory*, vol. 60, no. 11, pp. 7112–7139, 2014.

[28] E. Björnson, L. Sanguinetti, and J. Hoydis, "Hardware distortion correlation has negligible impact on UL massive mimo spectral efficiency," *IEEE Transactions on Communications*, vol. 67, no. 2, pp. 1085–1098, 2019.

[29] M. Taylor, *Measure Theory and Integration* (Graduate studies in mathematics). American Mathematical Society, 2006.

[30] D. Dardari, "Communicating with large intelligent surfaces: Fundamental limits and models," *IEEE Journal on Selected Areas in Communications*, vol. 38, no. 11, pp. 2526–2537, 2020.

[31] G. Cardano, T. R. Witmer, and O. Ore, *The rules of algebra: Ars Magna*. Courier Corporation, 2007, vol. 685.

[32] B. Hassibi and B. Hochwald, "How much training is needed in multiple-antenna wireless links?" *IEEE Transactions on Information Theory*, vol. 49, no. 4, pp. 951–963, 2003.

Paper IV

Hardware Distortion Modeling for Panel Selection in Large Intelligent Surfaces

Hardware distortion in large intelligent surfaces (LISs) may limit their performance when scaling up such systems. It is of great importance to model the non-ideal effects in their transceivers to study the hardware distortions that can affect their performance. Therefore, we have focused on modeling and studying the effects of nonlinear RX-chains in LISs. We first derive expressions for SNDR of a LIS with a memory-less polynomial-based model at its RX-chains. Then we propose a simplified double-parameter exponential model for the distortion power and show that compared to the polynomial based model, the exponential model can improve the analytical tractability for SNDR optimization problems. In particular, we consider a panel selection optimization problems in a panel-based LIS scenario and show that the proposed model enables us to derive two closed-form sub-optimal solutions for panel selection, and can be a favorable alternative to high-order polynomial models in terms of computation complexity, especially for theoretical works on hardware distortion in MIMO and LIS systems. Numerical results show that the sub-optimal closed-form solutions have a near-optimal performance in terms of SNDR compared to the global optimum found by high-complexity heuristic search methods.

1 Introduction

The rapid increase in number of devices and quality of service demands within 5G and forthcoming 6G networks has led to a substantial escalation in overall network requirements. To address these demands, the development and implementation of novel physical layer technologies are essential for accommodating the heightened performance expectations and ensuring network reliability and efficiency. LISs are regarded as a pivotal advancement in the ongoing evolution of wireless communication networks. In theory, LISs have demonstrated significant potential to meet these expectations, primarily by offering greater degrees of freedom compared to conventional massive MIMO systems [1], [2], [3]. While the anticipated benefits of deploying LIS technology are promising, considerable debate persists regarding the feasibility and hardware implementation challenges associated with integrating LIS into future wireless networks. LISs are envisioned to have hundreds to thousands of active transceiver chains which can result in a huge leap in the implementation cost, power consumption, and overall processing complexity of the system [4].

Achieving the expected theoretical gains when implementing LISs in future wireless networks may only become feasible by deploying less expensive hardware components in the transceiver chains. The drawback from selecting these low-cost components are mainly the non-ideal effects that can introduce hardware distortion in the system, which can degrade the overall performance [5]. The inter-play between system performance, non-linearity, power consumption, and hardware complexity is one of the most important aspects in the design of future wireless transceivers [6], [7]. Mitigating non-ideal hardware distortion is expected to be an important subject when implementing LISs for future wireless networks.

In addition, to save on resources, we would also like to activate as few transceiver chains as possible. Full control of the activation of individual transceivers means full flexibility, but also lead to excessive system complexity. To limit complexity, we can arrange antennas in panels where all transceiver chains in a panel are switched on or off at the same time, which we call panel-based LIS. While there are many classic models and methods to model, study, and compensate the hardware distortion effects in MIMO transceivers [8], [9], [10], [11], applying them to LIS scenarios generally results in high-complexity problems when designing and optimizing the system. For example, while polynomial models are of great interest in the MIMO literature, employing them in a panel-selection optimization for a panel-based LIS, results in high complexity problems which can only be solved by heuristic methods [4]. Therefore, there is a need for more analytically favorable models for hardware distortion in LISs with negligible loss in the performance.

In this paper, we study the problem of receiver hardware distortion in LISs with non-linear RX-chains. We first analyze the distortion effect for the

memory-less polynomial (MLP) model and derive the SNDR for MRC scheme. Then, we propose a double-parameter exponential model for the hardware distortion power to reduce the complexity of the SNDR optimization problems. In particular, we formulate the problem of panel selection in panel-based LISs and show that with the MLP model, the panel selection problem can only be solved by heuristic search. On the other hand, the proposed model leads to more tractable optimization problems. We will show that the simplified panel selection problem can be approximated and solved into close-form sub-optimal solutions which can be adopted for the original panel selection problem, with near-optimum performance in terms of the SNDR.

2 System Model

We consider an uplink scenario where a single-antenna UE is served by a LIS through a narrow-band LOS channel[2]. The LIS consists of $N \gg 1$ antenna elements with non-linear RX-chains. The $N \times 1$ received vector at the LIS is

$$\boldsymbol{r} = f\left(\boldsymbol{h}s\right) + \boldsymbol{n}, \tag{1}$$

where $s \in \mathbb{C}$, with $\mathbb{E}\{|s|^2\} = P$, is the base-band (BB) symbol transmitted by the UE, and $\boldsymbol{h} \in \mathbb{C}^{N\times 1}$ is the LOS channel vector. The component-wise function $f(\cdot) : \mathbb{C}^{N\times 1} \to \mathbb{C}^{N\times 1}$ models the overall hardware distortion effects of the LIS non-linear RX-chains, and $\boldsymbol{n} \sim \mathcal{CN}(\boldsymbol{0}, \sigma^2 \boldsymbol{I}_N)$ models the receiver thermal noise.

2.1 RX-chain non-linearity

To analyze the effect of RX-chain hardware distortion, we can transform the RX-chain output $\boldsymbol{z} \triangleq f\left(\boldsymbol{h}s\right)$ into an additive form by leveraging the LMMSE of $\boldsymbol{z}$ given $\boldsymbol{x} \triangleq \boldsymbol{h}s$, which is

$$\boldsymbol{z} = \boldsymbol{C}_{\boldsymbol{z}\boldsymbol{x}}\boldsymbol{C}_{\boldsymbol{x}\boldsymbol{x}}^{-1}\boldsymbol{x} + \boldsymbol{\eta}, \tag{2}$$

where $\boldsymbol{\eta}$ is the estimation error. This is the same technique as applying the Bussgang theorem to the non-linearity function [12]. We can therefore re-write $\boldsymbol{r}$ as

$$\boldsymbol{r} = \boldsymbol{G}\boldsymbol{h}s + \boldsymbol{\eta} + \boldsymbol{n}, \tag{3}$$

[2]We have considered a single-user case to isolate the effect of hardware distortion at the LIS RX-chains from other non-ideal effects such as inter-user interference, since hardware distortion is the main focus of this work.

where $\boldsymbol{G} = \boldsymbol{C}_{\boldsymbol{zx}}\boldsymbol{C}_{\boldsymbol{xx}}^{-1}$. If we assume that the output of each RX-chain depends solely on its input and it is independent of other RX-chains, i.e., $\boldsymbol{z}_n$ only depends on $\boldsymbol{x}_n$, we have $\boldsymbol{G} = \text{diag}\{g_n\}$, $\boldsymbol{C}_{\boldsymbol{\eta\eta}} = \text{diag}\{C_n\}$, with g_n and C_n corresponding to the Busssgang gain compression and distortion power for the n'th antenna.

One of the most widely used models for non-linearities in wireless transceivers is the memory-less polynomial model [8], [13], given by

$$f(x_n) = \sum_{k=0}^{L-1} a_{2k+1}\ x_n|x_n|^{2k}, \tag{4}$$

where x_n is the input to one of the RX-chains of the LIS, and a_{2k+1} are the model parameters. The model coefficients can be calculated by curve fitting to input-output measurements data from transceivers [14] for a limited range of input amplitude. For a Gaussian input $x_n \sim \mathcal{CN}(0, \rho_n)$ which is a high peak-to-average signal, we need to normalize the model coefficients and consider a sufficient back-off at the RX-chains. The Bussgang parameters $\forall n \in \{1, \ldots, N\}$ can then be calculated as [4]

$$g_n = \sum_{k=0}^{L-1} a_{2k+1}(k+1)!\rho_n^k, \tag{5}$$

$$C_n = \sum_{k=1}^{2L-1} \left(k!\rho_n^k \sum_{i=1}^{k} a_{2i-1}\bar{a}_{2k-2i+1} \right) - |g_n|^2\rho_n, \tag{6}$$

which we will use to analyze the SNDR in the reminder of this paper.

2.2 SNDR for MRC

Let us assume that the LIS employs a combining vector $\boldsymbol{v}$ to equalize the received signal $\boldsymbol{r}$. It has been shown that MRC can leverage the available spatial degrees of freedom[2] effectively in LIS scenarios, and it is more favorable due to its reduced complexity. In our system model, we have an effective channel given by $\tilde{\boldsymbol{h}} = \boldsymbol{G}\boldsymbol{h}$. Therefore, the MRC vector is expressed as $\boldsymbol{v}^T = \tilde{\boldsymbol{h}}^H/\|\tilde{\boldsymbol{h}}\|$. This effective channel accounts for both the physical channel and the multiplicative hardware distortion effects. Since the signals used for channel estimation are also influenced by hardware distortion, the UL UE pilots would only allow the LIS to estimate the effective channel $\tilde{\boldsymbol{h}}$ [4]. For the purposes of this analysis, we assume that the LIS has a perfect estimate of $\tilde{\boldsymbol{h}}$.

By applying the MRC combining vector $\boldsymbol{v}^T = \tilde{\boldsymbol{h}}^H/\|\tilde{\boldsymbol{h}}\|$ to the received signal $\boldsymbol{r}$, while taking into account the Bussgang decomposition from (3), we

can calculate the SNDR as

$$\gamma = \frac{P\sum_{n=1}^{N}\left|\tilde{h}_n\right|^2}{\frac{\sum_{n=1}^{N} C_n\left|\tilde{h}_n\right|^2}{\sum_{n=1}^{N}\left|\tilde{h}_n\right|^2} + \sigma^2}. \tag{7}$$

For the memory-less polynomial model we have

$$\left|\tilde{h}_n\right|^2 = |h_n|^2 \left|\sum_{k=0}^{L-1} a_{2k+1,n}(k+1)!\ P^k|h_n|^{2k}\right|^2, \tag{8}$$

$$C_n = \sum_{k=1}^{2L-1}\left(k!\ P^k|h_n|^{2k}\sum_{i=1}^{k} a_{2i-1,n}\bar{a}_{2k-2i+1,n}\right) - \left|\tilde{h}_n\right|^2 P, \tag{9}$$

which are calculated according to (5) and (6).

2.3 Exponential Model for Distortion Power

While it is possible to derive closed-form expressions for SNDR with the memory-less polynomial model [4], a simplified model with fewer number of parameters is of fundamental interest, especially when dealing with optimization problems involving the SNDR. The model should be an increasing function of the input power, and follow the general form of the distortion power (6). Another downside with the distortion power function for memory-less polynomial model is that the distortion power may increase unboundedly when input power grows, an effect that can not occur in reality. In particular, when considering high peak-to-average power signals, such as Gaussian symbols, this can have a significant influence on the accuracy of the analysis. Therefore, the proposed model for the distortion power should not grow unboundedly with the input power.

With the given conditions on the model properties, we propose the following double-parameter exponential model for the distortion power

$$\tilde{C}_n = \rho\left(1 - e^{-\beta\rho^q}\right), \tag{10}$$

where $\beta > 0$ and $q > 2$ are the model parameters and are calculated by curve-fitting to hardware measurements, or potentially, to the distortion power of any other well-known model such as (6) for memory-less polynomial model. We will show that this model can be exploited as a tool to simplify the SNDR optimization problems for systems with hardware distortion. In particular, we will show an application of this model in the LIS panel selection problem in the next section.

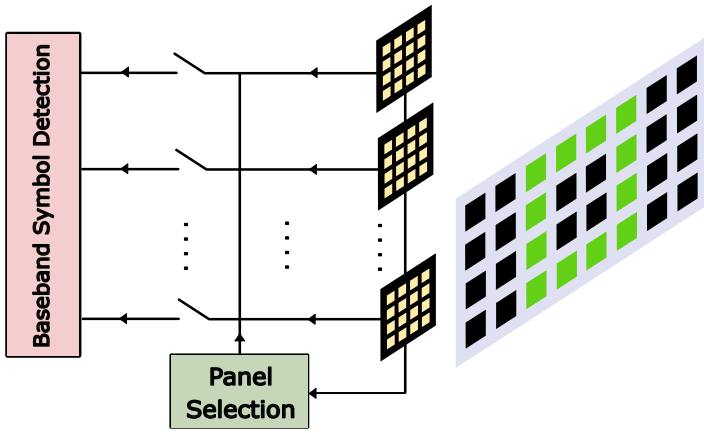

Figure 1: LIS configuration and Panel Selection. Each panel, represented by a square, has the same number of antennas and green squares indicate the active panels. Each antenna is equipped with a non-linear analogue front end (AFE).

3 Panel Selection in LIS

One of favorable approaches in terms of practicality for LIS deployment is to construct them as a grid of panels [15]. We consider a panel-based LIS with N_p panels each consisting of M antenna elements with non-linear RX-chains. We assume that there is a resource constraint in the system which forces the LIS to only use $N_{\max}$ panels for received signal combining. Fig. 1 illustrates an example system architecture with panel selection. We select the SNDR after MRC as the objective function and formulate a panel selection problem with the aim of finding the set of $N_{\max}$ panels to achieve the highest SNDR.

The panel selection problem can be translated into the following optimization problem

$$\begin{aligned} \max_{z_n} \; & \frac{PM \sum_{n=1}^{N_p} z_n \left|\tilde{h}_n\right|^2}{\frac{\sum_{n=1}^{N_p} z_n C_n \left|\tilde{h}_n\right|^2}{\sum_{n=1}^{N_p} \left|\tilde{h}_n\right|^2} + \sigma^2}, \\ \text{s.t.} \;\; & z_n \in \{0,1\} \qquad n = 1,2,...,N \\ & \sum_{n=1}^{N_p} z_n \leq N_{\max}, \end{aligned} \tag{11}$$

where z_n is the binary variable for panel selection, and $|\tilde{h}_n|^2$ is the effective channel gain between the antenna elements on the n'th panel and the UE. The considered formulation of the problem assumes that the distance between

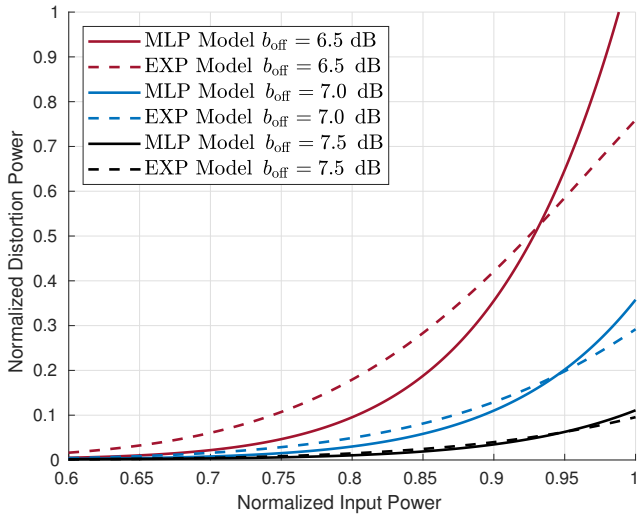

Figure 2: MLP and EXP Distortion Models.

antenna elements of each panel is negligible compared to the UE-LIS distance, which corresponds to having the users in the far-field of each LIS-panel, while they can still be in the near-field of the whole LIS. In general, we are able to solve this problem by heuristic search methods for any hardware distortion model.

An alternative approach, equivalent to a large extent to the original problem, is to consider a SISO case and find the optimum received power for maximum SNDR, and then select the $N_{\max}$ panels with the closest received power to that optimum value. For the memory-less polynomial model, the panel selection problem is reduced to

$$\max_{\rho} \frac{|\sum_{k=0}^{L-1} a_{2k+1}(k+1)!\rho^k|^2\rho}{\sum_{k=1}^{2L-1}\left(k!\rho^k\sum_{i=1}^{k} a_{2i-1}\bar{a}_{2k-2i+1}\right)-|g|^2\rho+\sigma^2} \quad \text{s.t.} \quad 0<\rho<\rho_{\max}, \tag{12}$$

which is still not analytically tractable. We are thus interested in approximating the objective function in this optimization problem to find effective closed-form solutions.

The panel selection problem defined above constitutes a good application of the proposed distortion model, which may help increasing tractability. We approximate the objective function in (12) by deploying the proposed exponential model in (10). We also neglect the gain compression parameter in the numerator since it has a negligible effect on SNDR compared to the distortion power

[3]. After applying these assumptions, we end-up with the following simplified problem.

$$\max_{\rho} \frac{\rho}{\rho\left(1-e^{-\beta\rho^{q}}\right)+\sigma^{2}} \quad \text{s.t. } 0<\rho<\rho_{\max}, \tag{13}$$

We will show that, unlike (12), this problem can be solved into closed-form approximated solutions with near-optimal performance.

Lemma 5 *The closed-form solution to the optimization problem* (13) *can be approximated by either of the following optimal values for* ρ_{opt} *with negligible error.*

$$\rho_{opt_1} \approx \left(\frac{1-\sqrt{1-\frac{4\sigma^2}{q}}}{2\beta}\right)^{1/(q+1)}, \tag{14}$$

$$\rho_{opt_2} \approx exp\left(\frac{Ln(\sigma^2)-Ln(q\beta)}{q+1}\right). \tag{15}$$

Proof *See Appendix 6.* □

We will study the performance of these approximated sub-optimal solutions and show that both have negligible error compared to the global optimum, while ρ_{opt_2} is generally more accurate. The LIS can thus exploit these closed-form results for efficient panel selection. Although this is a sub-optimal approach to deal with the original problem in (11), we will show that the performance is very close to the global optimal case achieved with heuristic search methods, which means that we can get a near-optimum solution with significantly lower computation complexity by adopting the proposed distortion model and approximated panel selection solutions.

4 Numerical Results

In this section, we analyze the hardware distortion in LISs for the memory-less polynomial model (MLP) and the proposed exponential model (EXP). For the RX-chains non-linearity model parameters, we have considered an 11-th order memory-less polynomial model based on [14] for a Gallium Nitride (GaN) amplifier operating at 2.1 GHz at a sample rate of 200 MHz and a

[3]We have studied and verified this numerically for the measurement data from [14]. We will also show that this assumption has negligible impact on the performance of the proposed sub-optimal solutions.

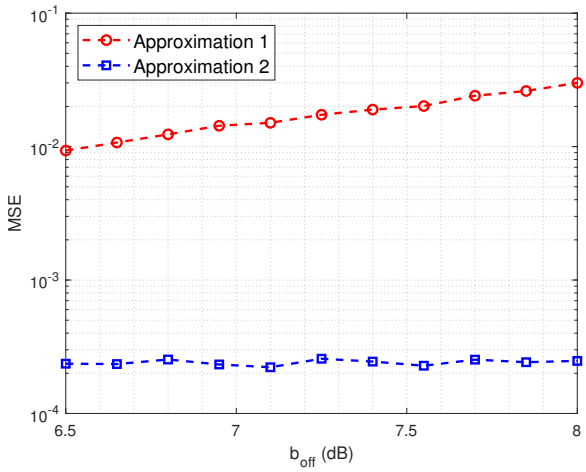

Figure 3: Mean square error (MSE) for optimum ρ approximations from lemma 5.

signal bandwidth of 40 MHz. Different levels of back-off are considered which adjust the severeness of the distortion as described in [4].

In Fig. 2 we have compared the approximated EXP distortion power (10) to the exact MLP distortion power (6) for the GaN amplifier with three different levels of back-off. The EXP model parameters β and q calculated with MATLAB curve fitting. We can see that the approximated EXP model follows the exact model closely, and the difference is lower for higher values of back-off. We will show that this difference has negligible effect on the performance of the proposed sub-optimal solutions for panel selection.

In Fig. 3 we illustrate the MSE of the proposed approximations in Lemma 5 with respect to the accurate optimum solution to problem (13), found by heuristic search. We can see that both approximations have very low MSE, while the second approximation performs better for all levels of back-off. Therefore, we focus on the second approximation for solving the approximate version of the panel selection problem (11).

Fig. 4 illustrates the performance of LIS, in terms of lower bound on spectral efficiency (SE), when adopting the proposed sub-optimal solution for panel selection compared to the global optimum case found by solving (11) with heuristic search. We have also included a base-line approach where the LIS only selects the panels with highest channel gain which is the optimal solution in ideal systems. Firstly, we can see that in the presence of RX-chain hardware distortion, panel selection can improve the system performance significantly. Secondly, we can see that the proposed sub-optimal solution based on the second approximated power level from Lemma (5) has near-perfect performance.

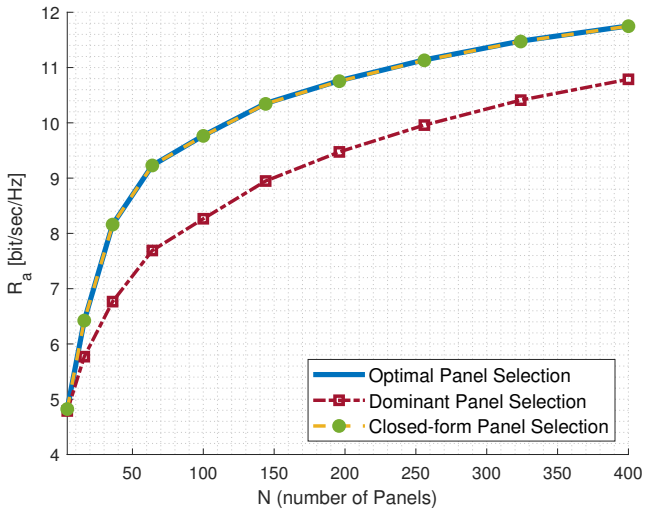

Figure 4: SE lower bound vs number of panels. The UE is at distance $d = 50\lambda$ from the center of LIS transmitting with power P such that SNR$= 10dB$ at the center of LIS. Each panel is equipped with $M = 16$ antenna elements with $\lambda/2$ spacing, $N_{\max} = \lceil 0.1N \rceil$, $b_{\text{off}} = 7dB$, and there is a distance of $\delta_p = 5\lambda$ between the center of adjacent panels.

5 Conclusion

In this paper, we have studied the hardware distortion effects in LISs with non-ideal RX-chains. Firstly, we considered the memory-less polynomial model and formulated the SNDR for the LIS. Although the SNDR can be characterized in closed-form this model, the resulting expression gives poor analytical tractability towards solving optimization problems such as LIS panel selection. Thus, we have proposed a double-parameter exponential model for the distortion power and employed it to characterize close-form approximate solutions to the LIS panels. The proposed methods attain close-to-optimum performance, essentially overlapping the performance achieved by global optimum solutions found through heuristic search.

Appendices 1 6 Proof of Approximations

To solve (13)*, we can show that the problem is convex*[4]*. We can therefore solve it by finding the roots of the first derivative of the objective function. The*

[4]The proof is not included but it is straightforward.

equation to find the roots can be simplified to

$$\sigma^2 - q\beta\rho^{q+1}e^{-\beta\rho^q} = 0. \tag{16}$$

By defining $x \triangleq \beta\rho^{q+1}$ *and approximating* $e^{-\beta\rho^q}$ *with* e^{-x}*, we have*

$$\sigma^2 - qxe^{-x} \approx 0. \tag{17}$$

Fitting the proposed exponential model to the measurement data from [14] shows that in all cases $\beta \ll 1$*, which results in* $x \ll 1$*. Therefore, we can use the Taylor approximation to write* $qxe^{-x} \approx x(1-x)$*. Replacing this in* (17) *results in a quadratic equation which gives the first approximated solution* ρ_{opt_1}*.*

The second approximation ρ_{opt_2} *can be found by taking the natural logarithm of* (16) *which results in*

$$Ln(\sigma^2) = (q+1)Ln(\rho) + Ln(q\beta) - \beta\rho^q. \tag{18}$$

As discussed above, $\beta\rho^q \ll 1$*, therefore we can neglect the last term, and solve the above equation for* ρ *which results in the closed form approximated solution* ρ_{opt_2}*.*

References

[1] S. Hu, F. Rusek, and O. Edfors, "The potential of using large antenna arrays on intelligent surfaces," in *2017 IEEE 85th Vehicular Technology Conference (VTC Spring)*, 2017, pp. 1–6.

[2] S. Hu, F. Rusek, and O. Edfors, "Beyond massive MIMO: The potential of data transmission with large intelligent surfaces," *IEEE Transactions on Signal Processing*, vol. 66, no. 10, pp. 2746–2758, 2018.

[3] D. Dardari, "Communicating with large intelligent surfaces: Fundamental limits and models," *IEEE Journal on Selected Areas in Communications*, vol. 38, no. 11, pp. 2526–2537, 2020.

[4] A. Sheikhi, J. V. Alegría, and O. Edfors, *Large intelligent surfaces with low-end receivers: From scaling to antenna and panel selection*, 2024. arXiv: `2411.04702 [eess.SP]`.

[5] J. V. Alegría and F. Rusek, "Achievable rate with correlated hardware impairments in large intelligent surfaces," in *2019 IEEE 8th International Workshop on Computational Advances in Multi-Sensor Adaptive Processing (CAMSAP)*, 2019, pp. 559–563.

[6] A. Sheikhi, F. Rusek, and O. Edfors, "Massive MIMO with per-antenna digital predistortion size optimization: Does it help?" In *ICC 2021 - IEEE International Conference on Communications*, 2021, pp. 1–6.

[7] M. Sarajlić, A. Sheikhi, L. Liu, H. Sjöland, and O. Edfors, "Power scaling laws for radio receiver front ends," *IEEE Transactions on Circuits and Systems I: Regular Papers*, vol. 68, no. 5, pp. 2183–2195, 2021.

[8] D. Morgan, Z. Ma, J. Kim, M. Zierdt, and J. Pastalan, "A generalized memory polynomial model for digital predistortion of RF power amplifiers," *IEEE Transactions on Signal Processing*, vol. 54, no. 10, pp. 3852–3860, 2006.

[9] A. S. Tehrani, H. Cao, S. Afsardoost, T. Eriksson, M. Isaksson, and C. Fager, "A comparative analysis of the complexity/accuracy tradeoff in power amplifier behavioral models," *IEEE Transactions on Microwave Theory and Techniques*, vol. 58, no. 6, pp. 1510–1520, 2010.

[10] A. Sheikhi, O. Edfors, and J. V. Alegría, *Over-the-air DPD and reciprocity calibration in massive MIMO and beyond*, 2024. arXiv: 2411.04689 [eess.SP].

[11] A. Sheikhi and O. Edfors, "Machine learning based digital pre-distortion in massive MIMO systems: Complexity-performance trade-offs," in *2023 IEEE Wireless Communications and Networking Conference (WCNC)*, 2023, pp. 1–6.

[12] O. T. Demir and E. Björnson, "The Bussgang decomposition of nonlinear systems: Basic theory and MIMO extensions [lecture notes]," *IEEE Signal Processing Magazine*, vol. 38, no. 1, pp. 131–136, 2021.

[13] B. Razavi, *RF Microelectronics (2nd Edition) (Prentice Hall Communications Engineering and Emerging Technologies Series)*, 2nd. USA: Prentice Hall Press, 2011.

[14] "Further elaboration on PA models for NR," *document 3GPP TSG-RAN WG4, R4-165901, Ericsson, Stockholm, Sweden*, Aug. 2016.

[15] A. Pereira, F. Rusek, M. Gomes, and R. Dinis, "Deployment strategies for large intelligent surfaces," *IEEE Access*, vol. 10, pp. 61 753–61 768, 2022.

Paper V

Over-the-Air DPD and Reciprocity Calibration in Massive MIMO and Beyond

Non-linear transceivers and non-reciprocity of downlink and uplink channels are two major challenges in the deployment of massive MIMO systems. We consider an OTA approach for DPD and reciprocity calibration to jointly address these issues. In particular, we consider a memory-less non-linearity model for the BS transmitters, and we propose a method to perform both linearization and reciprocity calibration based on mutual coupling OTA measurements between BS antennas. We show that, by using only the OTA-based data, we can linearize the transmitters and design the calibration to compensate for both the non-linearity and non-reciprocity of BS transceivers. This allows alleviating the requirement to have dedicated hardware modules for transceiver linearization. Moreover, the proposed reciprocity calibration method is solely based on closed-form linear transformations, achieving a significant complexity reduction over state-of-the-art reciprocity methods, which assume linear transceivers, and rely on iterative methods. Simulation results showcase the potential of our approach in terms of the calibration matrix estimation error and downlink data-rates when applying ZF precoding after using our OTA-based DPD and reciprocity calibration method.

1 Introduction

Massive MIMO has been one of the main technologies in the development of the fifth-generation (5G) of wireless networks, by enabling significant improvements in network capacity and reliability [1]. In the early stages of massive MIMO development, several proposals motivated the adoption of FDD in massive MIMO deployments. While some advantages may arise from considering FDD [2], the over-head in downlink channel estimation is an important drawback which limits the system scalability. Therefore, TDD is selected as the more viable approach for the deployment of massive MIMO in 5G and beyond, since it enables downlink channel estimation based on uplink channel state information (CSI) and channel reciprocity [3].

In ideal TDD systems, perfect channel reciprocity allows the BS to use the UL CSI for DL precoding. However, in practical deployments, the differences between TX and RX hardware may compromise this assumption [4]. To compensate the differences, reciprocity calibration methods are employed. There are several approaches for reciprocity calibration in massive MIMO. OTA-based reciprocity calibration methods relying on mutual-coupling measurements are specially promising since they do not require dedicated hardware for calibration [4], [5], [6], [7]. Another challenge in implementing massive MIMO systems is the non-linear response of the transceivers. There are several methods to compensate these non-linear effects, with per-antenna DPD being the most favorable option because of its effectiveness. To perform the DPD, many approaches rely on input-output measurements of the TX-chains with the aim of designing an inverse function for canceling the non-linear effects [8]. OTA-based DPD approaches, such as methods based on wireless links with near-field or far-field probes, have emerged as an efficient alternative to linearize the amplifiers [9]. To the best of our knowledge, no prior work has addressed the joint problem of reciprocity calibration and TX-chain linearization using OTA techniques. Specifically, existing literature does not explore approaches that unify DPD and reciprocity calibration within a shared framework, thereby reducing the need for dedicated DPD modules.

In this paper, we propose a method exploiting OTA measurements of inter-antenna mutual couplings at the BS to perform both the DPD and reciprocity calibration. The literature on reciprocity calibration has focused on the latter by assuming linearized transceivers [4], [5], [6], [7]. This assumption is not accurate in practical cases, especially when scaling up massive MIMO systems, which necessitates deploying less expensive non-linear components and non-ideal linearization techniques for cost-efficiency reasons. Therefore, we assume that the TX-chains in the BS are non-linear and we propose a method to linearize them based on mutual coupling measurements. Our approach relies on the same hardware available for OTA-based reciprocity calibration, which improves resource efficiency by eliminating the need for dedicated hardware to

perform per-antenna DPD. Considering the linearized transmitters after applying our OTA-based method, we derive a reciprocity calibration approach which depends only on linear closed-form transformations. Thus, the proposed reciprocity calibration allows for a significant complexity reduction over iterative methods focusing on the reciprocity calibration problem [4], [5], [6], [7]. Numerical results show that, even with the extra challenge of having to deal with non-linear TX-chain compensation, the calibration matrix estimation error approaches the Cramer-Rao Lower Bound (CRLB), which was derived in [5]. We also evaluate the system performance in downlink data transmission using ZF precoding and show that the proposed method can approach the perfect calibration performance even though we are considering non-linear TX-chains.

2 System Model

We consider a TDD multi-user-MIMO scenario where an M-antenna BS serves $K \leq M$ UEs through a narrow-band channel. For the UEs, we assume that the TX- and RX-chains are both operating in the linear regime. For the BS, we assume that the RX-chains are also operated in the linear regime, but the TX-chains exhibit non-linear response.[5]

2.1 Uplink

The $M \times 1$ vector of received symbols at the BS during an UL transmission may be expressed as

$$\boldsymbol{y}_{\mathrm{B}} = \boldsymbol{H}_{\mathrm{UL}} \boldsymbol{s}_{\mathrm{U}} + \boldsymbol{n}_{\mathrm{B}}, \tag{1}$$

where $\boldsymbol{s}_{\mathrm{U}}$ is the $K \times 1$ vector of input symbols to each UE TX-chain and $\boldsymbol{n}_{\mathrm{B}} \sim \mathcal{CN}(\boldsymbol{0}, N_{0,\mathrm{B}} \boldsymbol{I}_M)$ models the additive white Gaussian noise (AWGN) at the BS. The $M \times K$ channel matrix, is given by

$$\boldsymbol{H}_{\mathrm{UL}} = \boldsymbol{R}_{\mathrm{B}} \boldsymbol{H} \boldsymbol{T}_{\mathrm{U}}, \tag{2}$$

where $\boldsymbol{R}_{\mathrm{B}} = \mathrm{diag}(r_1^{\mathrm{B}}, \ldots, r_M^{\mathrm{B}})$ and $\boldsymbol{T}_{\mathrm{U}} = \mathrm{diag}(t_1^{\mathrm{U}}, \ldots, t_K^{\mathrm{U}})$ are associated with the linear response of the BS receivers and the UE transmitters, respectively, and $\boldsymbol{H}$ corresponds to the $M \times K$ reciprocal propagation channel matrix [5]. The UL channel in (2), which includes the effects of the UE transmitters and the BS receivers, can be estimated at the BS based on UL pilots transmitted by the UEs, allowing for effective implementation of linear processing techniques, e.g., ZF and MRC.

[5] Assuming non-linear behavior only in the BS TX-chains is reasonable taking into account that this is where the input power is significantly higher, pushing the power amplifiers to the non-linear regime [10]. For the UEs, this non-linearity may be compensated with a single DPD module per UE.

Note that, if the UEs transmitters had non-linear behavior, the term $\boldsymbol{T}_{\mathrm{U}}$ in the estimated UL channel would be substituted by a non-linear function of the pilot matrix. A thorough study of this case may be considered in future work, but the presented method would still be able to cope with the non-linearity and non-reciprocity originated at the BS side.

2.2 Downlink

During the DL transmission phase, the $K \times 1$ vector of symbols received at the UEs may be expressed as

$$\boldsymbol{y}_{\mathrm{U}} = \boldsymbol{R}_{\mathrm{U}} \boldsymbol{H}^{\mathrm{T}} \boldsymbol{f}(\boldsymbol{x}_{\mathrm{B}}) + \boldsymbol{n}_{\mathrm{U}}, \tag{3}$$

where $\boldsymbol{x}_{\mathrm{B}}$ is the $M \times 1$ vector of input symbols to each BS TX-chain, $\boldsymbol{n}_{\mathrm{U}} \sim \mathcal{CN}(\boldsymbol{0}, \mathrm{diag}(N_{0,\mathrm{U}_1}, \ldots, N_{0,\mathrm{U}_K}))$ models the AWGN at the UEs,
$\boldsymbol{R}_{\mathrm{U}} = \mathrm{diag}(r_1^{\mathrm{U}}, \ldots, r_K^{\mathrm{U}})$ is associated with the linear response of the UE receivers, and $\boldsymbol{f} : \mathbb{C}^{M\times 1} \to \mathbb{C}^{M\times 1}$ is a vector-valued function modeling the non-linear response of the BS TX-chains. We assume that the transmitted symbols are generated such that

$$\boldsymbol{x}_{\mathrm{B}} = \boldsymbol{g}(\boldsymbol{W}\boldsymbol{s}_{\mathrm{B}}), \tag{4}$$

where $\boldsymbol{s}_{\mathrm{B}}$ is the $K \times 1$ vector of symbols intended for the UEs, $\boldsymbol{W}$ is the $M \times K$ linear precoding matrix applied at the BS baseband unit (BBU), and $\boldsymbol{g} : \mathbb{C}^{M\times 1} \to \mathbb{C}^{M\times 1}$ is the non-linear vector-valued function associated to the DPD applied at each TX-chain.

Let us assume that the cross-talk between TX-chains is negligible so that $\boldsymbol{f}(\cdot)$, and correspondingly $\boldsymbol{g}(\cdot)$, are component-wise functions. Considering a third-order memory-less polynomial model [11], we have

$$f_m(\boldsymbol{x}) = t_m^{\mathrm{B}} x_m + \beta_m x_m |x_m|^2, \quad \forall m \in \{1, \ldots, M\}, \tag{5}$$

where t_m^{B} and β_m are two complex scalars characterizing the non-linear response of the m'th TX-chain at the BS. In general, the BS TX-chain and UEs RX-chain responses are unknown, which means that the non-linear parameters t_m^{B} and β_m, as well as the diagonal entries of $\boldsymbol{R}_{\mathrm{U}}$, are unknown at the BS. Note that, unlike state-of-the-art work on reciprocity calibration [4], [5], [6], [7], where $\boldsymbol{f}(\cdot)$ is associated to a linear transformation $\boldsymbol{T}_B = \mathrm{diag}(t_1^{\mathrm{B}}, \ldots, t_M^{\mathrm{B}})$, we cannot hereby define an aggregated DL channel matrix due to the non-linear nature of the TX-chains.

2.3 Background: OTA Reciprocity Calibration

As mentioned earlier, previous work has addressed the problem of reciprocity calibration in massive MIMO assuming BS TX-chains operating in linear regime

[4], [5], [6], [7]. Under such assumptions, we may define the DL channel matrix as

$$\boldsymbol{H}_{\mathrm{DL}} = \boldsymbol{R}_{\mathrm{U}} \boldsymbol{H}^{\mathrm{T}} \boldsymbol{T}_{\mathrm{B}}, \tag{6}$$

which may be also derived from the presented system model, assuming $\beta_m = 0$ in (5).[6] The main goal of reciprocity calibration methods is to estimate the reciprocity matrix,

$$\boldsymbol{C} = \boldsymbol{T}_{\mathrm{B}} \boldsymbol{R}_{\mathrm{B}}^{-1}. \tag{7}$$

The reason is that, if we have knowledge of $\boldsymbol{C}$, we can transform the estimated UL channel matrix into

$$\begin{aligned} \widetilde{\boldsymbol{H}}_{\mathrm{DL}} &= \left(\boldsymbol{C} \boldsymbol{H}_{\mathrm{UL}}\right)^{\mathrm{T}} \\ &= \boldsymbol{T}_{\mathrm{U}} \boldsymbol{H}^{\mathrm{T}} \boldsymbol{T}_{\mathrm{B}}. \end{aligned} \tag{8}$$

Note that $\widetilde{\boldsymbol{H}}_{\mathrm{DL}}$ corresponds to $\boldsymbol{H}_{\mathrm{DL}}$ up to an unknown $K \times K$ diagonal matrix, namely $\boldsymbol{D} = \boldsymbol{T}_{\mathrm{U}} \boldsymbol{R}_{\mathrm{U}}^{-1}$, multiplied from the left. Hence, $\widetilde{\boldsymbol{H}}_{\mathrm{DL}}$ can be effectively used for linear precoding, with the only caveat that the symbols received by the UEs would end up multiplied by an unknown scalar, which has negligible impact on system performance [12].[7] We may thus ignore the non-reciprocity associated to the UEs hardware, modeled by $\boldsymbol{R}_{\mathrm{U}}$ and $\boldsymbol{T}_{\mathrm{U}}$, and focus on characterizing the non-reciprocity associated to the BS. An important advantage of the OTA-based calibration methods which are based on mutual coupling measurements is that they avoid the need for dedicated hardware to characterize the linear response of each TX-chain, and can improve the cost-efficiency of massive MIMO systems [5]. Similarly, we can argue that having dedicated hardware to perform DPD may compromise the cost-efficiency of MIMO systems with increasing number of antennas, e.g., massive MIMO and beyond. Thus, we next propose a method to jointly characterize the non-linear response of the BS TX-chains, as well as the resulting reciprocity matrix, to suitably design $\boldsymbol{g}(\cdot)$ and $\boldsymbol{W}$ for effectively serving the UEs in the DL.

3 OTA DPD and reciprocity calibration

Our proposed method may be divided into three stages:

- First, the non-linear response of the BS TX-chains, associated to $\boldsymbol{f}(\cdot)$, is estimated based on OTA mutual coupling measurements.
- Second, the DPD, associated to $\boldsymbol{g}(\cdot)$, is designed based on the estimated non-linear response.

[6] Equivalently, reciprocity calibration problems in [4], [5], [6], [7] may be obtained by assuming perfect DPD up to unknown scalars, i.e., $\boldsymbol{f}(\boldsymbol{g}(\boldsymbol{x})) = \boldsymbol{T}_{\mathrm{B}} \boldsymbol{x}$.

[7] In practice, this issue is addressed by sending a DL pilot [5].

- Third, reciprocity calibration is performed based on the DPD-linearized BS TX-chains, after which effective DL precoding, associated to $\boldsymbol{W}$, becomes available at the BS.

3.1 OTA non-linearity characterization

In this stage each BS antenna transmits $N_{\text{dpd}} \geq 2$ inter-antenna pilot signals to estimate the non-linearity parameters. The signal received at the j'th antenna when the ℓ'th pilot, $\ell \in \{1, \ldots, N_{\text{dpd}}\}$, is transmitted by the i'th antenna may be expressed as

$$y_{ij,\ell} = h_{ij} r_j \left(t_i x_{i,\ell} + \beta_i x_{i,\ell} |x_{i,\ell}|^2 \right) + n_{ij,\ell}, \tag{9}$$

where h_{ij} is the mutual coupling gain between antennas i and j, which is assumed fixed and known at the BS,[8] $x_{i,\ell}$ is the ℓ'th pilot symbol transmitted by the i'th antenna, and $n_{ij,\ell} \sim \mathcal{CN}(0, N_0)$ models the measurement noise. Note that we have removed the superscript B from the parameters r_j and t_i for notation convenience since, as previously reasoned, we may focus on the non-reciprocity associated to the BS.

For each pair of non-linearity parameters associated to one TX-chain, there are $M-1$ relevant DPD measurements per pilot transmission, i.e., all of those originated in the same antenna, but received at different antennas. Thus, each of these measurements would share the same t_i and β_i in (5), but they would be related to a different complex gain r_j, associated to the linear response of the RX-chain from the respective receiving antenna. Since the complex gains r_j are unknown, it is not possible to directly estimate the non-linearity parameters t_i and β_i from this dataset. However, we may combine the $M-1$ measurements by averaging them after compensating for the known mutual coupling gains, so as to reduce the uncertainty, as well as the resulting noise. The combined measurements are then given by

$$\begin{aligned} \tilde{y}_{i,\ell} &= \frac{1}{M-1} \sum_{j \neq i} \frac{y_{ij,\ell}}{h_{ij}} \\ &= q_i (t_i x_{i,\ell} + \beta_i x_{i,\ell} |x_{i,\ell}|^2) + \tilde{n}_{i,\ell}, \end{aligned} \tag{10}$$

where the uncertainty is now captured in the unknown parameter q_i, given by

$$q_i = \frac{1}{M-1} \sum_{j \neq i} r_j. \tag{11}$$

[8]The coupling gains may be characterized with a single measurement of the antenna system using a network analyzer [5]. Thus, knowledge of these may be assumed in any MIMO-related scenario with co-located TX antennas.

Note that one could also explore alternative optimized combinations to the simple average in (6). For example, a weighted average could be optimized assuming a specific model for h_{ij} or a concrete probability distribution for r_j, but this is out of scope for this paper and may be considered in future work. On the other hand, explicit knowledge of h_{ij} could be avoided by absorbing it into q_i, as further remarked in Sec. 3.3.

The $N_{\text{dpd}} \times 1$ data vector $\tilde{\boldsymbol{y}}_i = [\tilde{y}_{i,1}, \ldots, \tilde{y}_{i,N_{\text{dpd}}}]^{\text{T}}$ may then be used to estimate the non-linearity parameters of each antenna up to the unknown factor q_i. Since our initial aim is to compensate the non-linear response of the TX-chains, this is still possible if we know the non-linear response up to an unknown linear factor, which would only have a linear effect after the non-linearity compensation. In this case, the DPD would be designed as if the non-linearity parameters are $\theta_{1i} = q_i t_i$ and $\theta_{2i} = q_i \beta_i$. We may thus rewrite the combined data vector as

$$\tilde{\boldsymbol{y}}_i = \boldsymbol{\Phi}_i \boldsymbol{\theta}_i + \tilde{\boldsymbol{n}}_i, \tag{12}$$

where $\boldsymbol{\theta}_i = [\theta_{1i}, \theta_{2i}]^{\text{T}}$ is the 2×1 vector of parameters to be estimated, $\boldsymbol{\Phi}_i$ is the $N_{\text{dpd}} \times 2$ known pilot matrix whose columns are given by $\boldsymbol{\Phi}_{i,1} = [x_{i,1}, \ldots, x_{i,N_{\text{dpd}}}]^{\text{T}}$ and $\boldsymbol{\Phi}_{i,2} = [x_{i,1}|x_{i,1}|^2, \ldots, x_{i,N_{\text{dpd}}}|x_{i,N_{\text{dpd}}}|^2]^{\text{T}}$, and $\tilde{\boldsymbol{n}}_i \sim \mathcal{CN}(\boldsymbol{0}, \varsigma_i \boldsymbol{I}_{N_{\text{dpd}}})$ is the resulting noise vector where

$$\varsigma_i = \frac{N_0}{(M-1)^2} \sum_{j \neq i} \frac{1}{|h_{ij}|^2}. \tag{13}$$

Since the noise vector is white i.i.d Gaussian, the least-squares (LS) estimator is also the minimum-variance unbiased (MVU) estimator [13], and can be used to estimate the scaled non-linearity parameters as

$$\hat{\boldsymbol{\theta}}_i = (\boldsymbol{\Phi}_i^H \boldsymbol{\Phi}_i)^{-1} \boldsymbol{\Phi}_i^H \tilde{\boldsymbol{y}}_i. \tag{14}$$

Note that, while we have presented our method for a 3rd order non-linearity model (5), which is the main source of inter-modulation terms falling within the operating frequencies, the method can be generalized for higher order non-linearity models as well. In case of considering non-linearity polynomial models of higher order, the vector $\boldsymbol{\theta}$ (correspondingly $\boldsymbol{\Phi}$) would include one term per polynomial coefficient and the presented method would still be applicable. Alternatively, one can fit any RF non-linear behavior to the 3rd order model, which should still capture its main impact [14].

3.2 DPD linearization

In this stage the non-linearity parameters estimated in the previous stage are used to linearize the output via DPD, i.e., by adjusting $\boldsymbol{g}(\cdot)$ in (3). The true

non-linearity to compensate is the nonlinear function given in (5). However, the estimated non-linearity parameters in (14), θ_{1i} and θ_{2i}, characterize a different component-wise function given by

$$\begin{aligned}\tilde{f}_m(\boldsymbol{x}) &= \theta_{1m}x_m + \theta_{2m}x_m|x_m|^2 \\ &= q_m f_m(\boldsymbol{x}).\end{aligned} \tag{15}$$

We may thus express

$$\boldsymbol{f}(\boldsymbol{x}) = \boldsymbol{Q}^{-1}\tilde{\boldsymbol{f}}(\boldsymbol{x}), \tag{16}$$

where $\boldsymbol{Q} = \text{diag}(q_1, \ldots, q_M)$.

Since the function $\tilde{\boldsymbol{f}}(\cdot)$ is fully characterized, we can find its inverse by using methods such as the postdistortion approach [15]. We may then select

$$\boldsymbol{g}(\cdot) = \tilde{\boldsymbol{f}}^{-1}(\cdot), \tag{17}$$

which is applied to the the transmitted symbols as described in (3). In practice, perfect DPD inversion may not be fully achievable, mainly due to limited DPD size and imperfect estimation of non-linearity parameters. We have considered imperfect inversion in the numerical results from Section 4.

The resulting symbols transmitted through the reciprocal channel, may then be expressed as

$$\begin{aligned}\boldsymbol{f}(\boldsymbol{x}_\text{B}) &= \boldsymbol{Q}^{-1}\tilde{\boldsymbol{f}}(\boldsymbol{g}(\boldsymbol{W}\boldsymbol{s}_\text{B})) \\ &= \boldsymbol{Q}^{-1}\boldsymbol{W}\boldsymbol{s}_\text{B}.\end{aligned} \tag{18}$$

Hence, applying the proposed OTA-DPD, results in an equivalent linear transmitter gain given by $\tilde{\boldsymbol{T}}_\text{B} = \boldsymbol{Q}^{-1}$. Now that the transmitter is linear, we can define a DL channel matrix equivalent to (6), but substituting $\boldsymbol{T}_\text{B}$ for $\tilde{\boldsymbol{T}}_\text{B}$, so that reciprocity calibration methods as those presented in [4], [5] are directly applicable. However, we will show that the reciprocity calibration can be performed without the need for complex iterative methods.

3.3 Reciprocity calibration

The last stage consists of performing OTA-based calibration considering the TX-chains previously linearized through the OTA-DPD stages. To this end, each BS antenna transmits pilots to other antennas. The received symbols at the j'th antenna from the i'th antenna may be expressed as

$$y_{ij} = h_{ij}r_j\tilde{t}_i x_{ij} + n_{ij}, \tag{19}$$

where the variables have direct correspondence with those defined in (5), but substituting t_i for $\tilde{t}_i = 1/q_i$ and having $\beta_i = 0$. The measurements defined in (16) can be directly employed to estimate the product of unknown parameters

$r_j\tilde{t}_i$. In fact, we may now use the trivial MVU estimator, given by

$$\widehat{r_j\tilde{t}_i} = \frac{1}{h_{ij}x_{ij}}y_{ij}. \tag{20}$$

However, in order to perform reciprocity calibration, we are actually interested in the reciprocity parameters, $c_m = \tilde{t}_m/r_m$, which define the adjusted reciprocity matrix entries from (7).

In [5], it was noted that multiplying all the reciprocity parameters by a common scalar does not compromise the effectiveness of the reciprocity calibration.[9] Thus, we may select one of the calibration parameters, e.g., c_1, and normalize all the rest by that value. The resulting scaled calibration parameters may then be expressed as

$$\tilde{c}_m \triangleq \frac{c_m}{c_1} = \frac{r_1\tilde{t}_m}{r_m\tilde{t}_1} \tag{21}$$

which corresponds to the ratio of $r_j\tilde{t}_i$ products appearing in (17) for $(i,j) \in \{(1,m),(m,1)\}$. Since each of these products can be estimated through (17), we can find estimates for the scaled calibration parameters by

$$\widehat{\tilde{c}_m} = \frac{\widehat{r_1\tilde{t}_m}}{\widehat{r_m\tilde{t}_1}}. \tag{22}$$

The estimation error of $\widehat{\tilde{c}_i}$ can be reduced by averaging several estimates of $r_1\tilde{t}_i$ and $r_i\tilde{t}_1$, which is possible if each BS antenna transmits $N_{\text{cal}} \geq 2$ pilots in (16). Note further that, assuming reciprocity of the mutual coupling coefficients, i.e. $h_{ij} = h_{ji}$, we could still estimate $\tilde{c}_m$ using (16) without explicit knowledge of h_{ij} since the coefficients would cancel each other in (19). The method does not rely on this assumption, since the coupling coefficients can be estimated in practice. Nevertheless, the coupling coefficients between antennas are reciprocal per definition since we are absorbing the non-reciprocity within our model.

We have thus shown that we can estimate all the entries of the calibration matrix up to a constant, i.e., we can estimate $\tilde{\boldsymbol{C}} = \frac{1}{c_1}\boldsymbol{C}$, by means of simple linear estimators. This allows achieving reciprocity without the need for high complexity iterative algorithms, such as the algorithms used in [5].

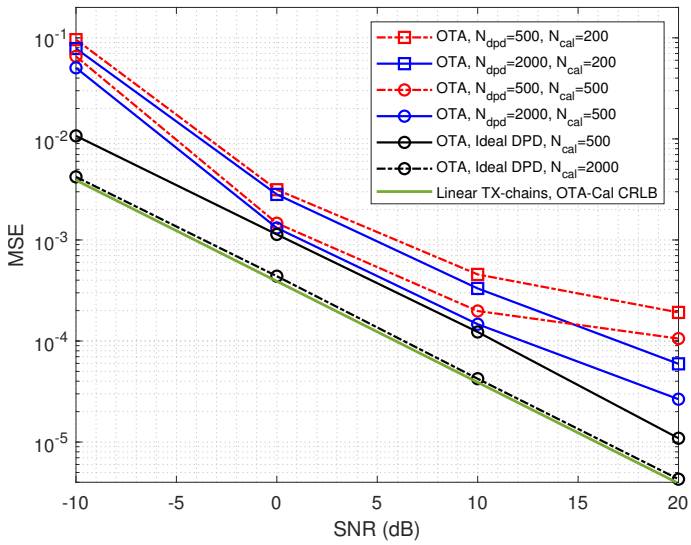

Figure 1: Average MSE of calibration matrix estimation using the proposed OTA DPD and reciprocity calibration.

4 Numerical results

In this section, we perform simulations to validate the feasibility and assess the performance of the proposed method. The number of BS antennas and the number of single-antenna UEs are $M = 100$ and $K = 10$, respectively. For the BS TX-chains non-linearity parameters in (5), we fit a 3rd order polynomial to the measurement data from [14] for a Gallium Nitride (GaN) amplifier operating at 2.1 GHz at a sample rate of 200 MHz and a signal bandwidth of 40 MHz. For the RX-chains complex gains, we use the values in [5] given by $r_m^B = 0.9 + 0.2\frac{M-m}{M}\exp(j2\pi m/M)$. To implement the imperfect inverse function in the DPD, we generate a look-up table based on the OTA data. For the mutual coupling channel gains in (5), we have used the linear LS fit based on the measurements in [5]. We also define the OTA link SNR as the receive SNR for the link between the antennas with least mutual coupling gain.

Fig. 1 illustrates the average MSE of the calibration matrix estimation with our proposed OTA-based method for different levels of SNR. The calibration matrix is estimated after performing the OTA-DPD, with $N_{\text{dpd}} = 500$ or 2000 OTA transmissions. In the calibration step, we have considered $N_{\text{cal}} = 200$, 500, or 2000 OTA transmissions. Note that transceiver characteristics are slowly-varying parameters, which means that even larger values of N_{dpd} and

[9]This constant scalar may be absorbed in the linear response of the UEs RX-chains, given by $\boldsymbol{R}_{\text{U}}$ in (3).

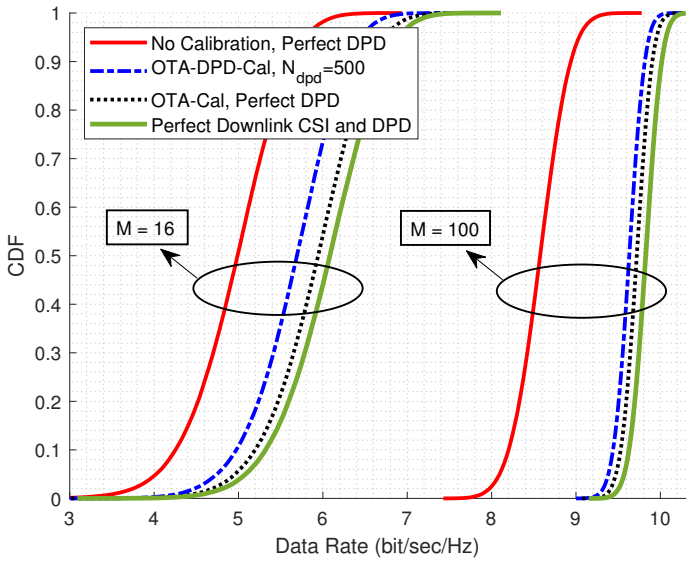

Figure 2: CDF of a UE DL data rate.

N_{cal} would still have a rather small impact on the total overhead. For comparison we have included an upper bound for the performance of the reciprocity calibration problem at hand, CRLB, derived in [5], which assumes linear TX-chains. We have also included the case with an ideal DPD followed by the OTA-based reciprocity calibration. Firstly, we can see that the performance of the OTA-based DPD and reciprocity calibration approaches the ideal DPD case. Secondly, we can see that the performance is fairly close to the CRLB, even though we have the extra challenge of dealing with non-linear TX-chains. Note that, in order to approach the CRLB, which is the ultimate performance bound for the reciprocity problem, [5] requires an iterative algorithm of considerable complexity. The reported complexity order in [5], which is considered state-of-the-art in massive MIMO reciprocity calibration [16], is given by $\mathcal{O}(M^2 N_{\text{ite}})$, where N_{ite} is the number of iterations of the algorithm. The complexity of our reciprocity calibration method is given by $\mathcal{O}(M N_{\text{cal}})$, since it requires averaging N_{cal} numbers where each of them is obtained by performing 2 multiplications for each of the $M-1$ antennas. Thus, for massive MIMO and beyond, where $M \gg 1$, our method may even attain significant complexity reduction, since reducing N_{cal} only has a minor impact on the calibration matrix MSE, as seen from Fig. 1. Other state-of-the-art reciprocity calibration methods require even higher complexity, while their performance is still limited by the CRLB. For example, the one in [7] for mm-Wave systems requires $\mathcal{O}(M^3)$ complexity to tackle the non-reciprocity problem with linear transceivers.

Fig. 2 illustrates the CDF of DL data rate under ZF precoding, where we

have generated 10^4 DL realizations of an i.i.d. Rayleigh fading channel, and the DL signal power for each UE is selected to achieve an average SNR of 10 dB at their receivers. We have selected $N_{\text{cal}} = 500$ for the OTA reciprocity calibration, OTA reference SNR of 0 dB, and OTA-DPD with $N_{\text{dpd}} = 500$. We have also performed the same reciprocity calibration for a case with perfect DPD. For comparison, we have included two extreme cases both with a perfect DPD, one with perfect DL CSI (ideal calibration), and one worst-case scenario with no calibration. We can observe that the limited-size DPD performs very close to the perfect DPD case, which further confirms the observations from Fig. 1. As for the calibration performance, we can see that the proposed OTA-DPD and reciprocity calibration approaches the ideal case with perfect DL CSI, without requiring high-complexity iterative algorithms, even-though we are dealing with the extra challenge of non-linear TX-chains. The gain from adopting the proposed OTA-case is more significant for higher number of antennas, i.e., massive MIMO and beyond, and the OTA-DPD performs closer to the ideal DPD case.

5 Conclusion

In this paper, we have proposed an OTA-based method for DPD and reciprocity calibration in massive MIMO and beyond. In particular, we considered a memory-less non-linearity model for the BS transmitters and proposed to perform the linearization and reciprocity calibration by using OTA measurements of the mutual coupling among the BS antennas. We showed that, by only using the OTA data, we can effectively linearize the transmitters and perform reciprocity calibration with reduced complexity over state-of-the-art. Simulation results showed promising performance of the proposed methodology, both in terms of the calibration matrix estimation error and the DL data-rates when applying ZF precoding after our OTA-based DPD and calibration method.

References

[1] E. G. Larsson, O. Edfors, F. Tufvesson, and T. L. Marzetta, "Massive MIMO for next generation wireless systems," *IEEE Communications Magazine*, vol. 52, no. 2, pp. 186–195, 2014.

[2] Z. Jiang, A. F. Molisch, G. Caire, and Z. Niu, "Achievable rates of FDD massive MIMO systems with spatial channel correlation," *IEEE Transactions on Wireless Communications*, vol. 14, no. 5, pp. 2868–2882, 2015.

[3] J. Flordelis, F. Rusek, F. Tufvesson, E. G. Larsson, and O. Edfors, "Massive MIMO performance—TDD versus FDD: What do measurements say?" *IEEE Transactions on Wireless Communications*, vol. 17, no. 4, pp. 2247–2261, 2018.

[4] H. Wei, D. Wang, H. Zhu, J. Wang, S. Sun, and X. You, "Mutual coupling calibration for multiuser massive MIMO systems," *IEEE Transactions on Wireless Communications*, vol. 15, no. 1, pp. 606–619, 2015.

[5] J. Vieira, F. Rusek, O. Edfors, S. Malkowsky, L. Liu, and F. Tufvesson, "Reciprocity calibration for massive MIMO: Proposal, modeling, and validation," *IEEE Transactions on Wireless Communications*, vol. 16, no. 5, pp. 3042–3056, 2017.

[6] M. Jokinen, O. Kursu, N. Tervo, A. Pärssinen, and M. E. Leinonen, "Over-the-air phase calibration methods for 5G mmW antenna array transceivers," *IEEE Access*, vol. 12, pp. 28 057–28 070, 2024.

[7] L. Chen, R. Nie, Y. Chen, and W. Wang, "Hierarchical-absolute reciprocity calibration for millimeter-wave hybrid beamforming systems," *IEEE Transactions on Wireless Communications*, vol. 22, no. 5, pp. 3570–3584, 2023.

[8] A. Katz, J. Wood, and D. Chokola, "The evolution of PA linearization: From classic feedforward and feedback through analog and digital predistortion," *IEEE Microwave Magazine*, vol. 17, no. 2, pp. 32–40, 2016.

[9] F. Rottenberg, T. Feys, and N. Tervo, *Optimal training design for over-the-air polynomial power amplifier model estimation*, 2024. arXiv: 2404.12830 [eess.SP].

[10] Y. Zou et al., "Impact of power amplifier nonlinearities in multi-user massive MIMO downlink," in *Proc. IEEE Globecom Workshops*, 2015, pp. 1–7.

[11] E. Björnson, L. Sanguinetti, and J. Hoydis, "Hardware distortion correlation has negligible impact on UL massive mimo spectral efficiency," *IEEE Transactions on Communications*, vol. 67, no. 2, pp. 1085–1098, 2019.

[12] F. Huang, J. Geng, Y. Wang, and D. Yang, "Performance analysis of antenna calibration in coordinated multi-point transmission system," in *2010 IEEE 71st Vehicular Technology Conference*, 2010, pp. 1–5.

[13] S. M. Kay, *Fundamentals of statistical signal processing: estimation theory*. USA: Prentice-Hall, Inc., 1993.

[14] "Further elaboration on PA models for NR," *document 3GPP TSG-RAN WG4, R4-165901, Ericsson, Stockholm, Sweden*, Aug. 2016.

[15] C. Eun and E. Powers, "A new volterra predistorter based on the indirect learning architecture," *IEEE Transactions on Signal Processing*, vol. 45, no. 1, pp. 223–227, 1997.

[16] Y. Xu, E. G. Larsson, E. A. Jorswieck, X. Li, S. Jin, and T.-H. Chang, "Distributed signal processing for extremely large-scale antenna array systems: State-of-the-art and future directions," *IEEE Journal of Selected Topics in Signal Processing*, vol. 19, no. 2, pp. 304–330, 2025.

Paper VI

Over-the-Air DPD and Reciprocity Calibration for Panel-based Large Intelligent Surfaces

We consider OTA-based approaches for joint DPD and reciprocity calibration in LIS systems. We build upon a state-of-the-art OTA-DPD and reciprocity calibration method, which we adapt for application in a LIS scenario, under non-linear transmitters modeled by a memory-less polynomial model of arbitrary order. While the OTA-based method can be effective for LIS systems in general, its performance may degrade under specific channel conditions, especially in panel-based LIS deployment, which is considered as a more practical implementation scheme for LISs. Therefore, we propose specific methods to improve the performance of the OTA-based calibration for panel-based LIS scenarios. We show that, under certain conditions, such as severe channel attenuation between certain panels, the performance of the original joint DPD and reciprocity calibration method can degrade substantially. To address this, we propose specific techniques to improve the performance under such conditions, mainly by exploiting intra-panel and inter-panel OTA transmissions separately, for DPD and calibration. Numerical results show that the proposed techniques significantly enhance the performance of OTA-based methods, effectively enabling the OTA-DPD and calibration for practical panel-based LIS systems.

Ashkan Sheikhi, Ove Edfors, J. Vidal Alegría,
"Over-the-Air DPD and Reciprocity Calibration for Panel-based Large Intelligent Surfaces, [Manuscript]"

1 Introduction

LISs have emerged as one of the promising technologies to enable the future advancements in wireless communication networks [1], [2]. While massive MIMO has already reached its maturity with the vision to meet the requirements of 5G networks, there is still significant gap between the initial visions and the practical deployments, and LISs are envisioned to potentially fill those gaps [3]. In theory LISs are proposed as continuous electromagnetically active surfaces, practical deployments are mostly leaning toward implementing the LIS as a dense array of antenna elements, or more practically, as a large number of multi-antenna panels [4]. In that sense, LIS is considered as scaled up massive MIMO systems, where the number of antenna elements grows even larger, enabling more exploitation of the spatial domain and near-field communication [5].

LISs are envisioned to work in TDD mode, same as massive MIMO, which means reciprocity calibration methods as the ones proposed for massive MIMO are needed to enable downlink precoding for LIS-based networks. Practical deployments and testbed have shown that OTA-based reciprocity calibration methods are very effective for massive MIMO systems [6], [7]. On the other hand, when scaling up massive MIMO systems, the necessity to deploy less-expensive non-ideal transmit and receive chains is of great importance. With a larger number of antenna elements, the linearization techniques can also cause an overhead in system complexity and overall power consumption. OTA-based DPD methods that jointly deal with non-linearity compensation and reciprocity calibration have been shown to be effective for massive MIMO scenarios with 3rd order non-linearity [8].

In this paper, we first formulate the OTA-based DPD and reciprocity calibration for a panel-based LIS scenario, and formalize the results to consider non-linearity memory-less polynomial models of arbitrary order. Then, we show that under specific conditions on the inter-antenna and inter-panel channels, the performance of state-of-the-art calibration methods can suffer from significant degradation. Therefore, specific techniques are needed to improve the OTA-based methods performance for the panel-based LIS. We present specific techniques to achieve this, mainly proposing to perform the OTA-based DPD and calibration in two steps by exploiting the inter-panel and inter-panel OTA links separately. Numerical results show that the OTA-based method is effective for DPD and calibration in LIS systems. Moreover, when the performance is degraded because of the channel conditions, the proposed techniques are effective to compensate that effect and improve the calibration performance.

2 System Model

We consider a DL TDD multi-user-MIMO scenario where a LIS serves K single-antenna UEs through a narrow-band channel. We assume imperfect transceivers at the LIS antenna elements, and uplink-downlink channel non-reciprocity due to different TX-chain and RX-chain hardware components at the LIS. The LIS consists of N panels, each equipped with M antenna elements. The i'th antenna RX-chain linear response is modeled by a complex gain, $r_i \in \mathbb{C}$, and the TX-chain non-linear response is given by

$$f_i(x_i) = \sum_{k=0}^{L-1} a_{2k+1,i}\ x_i|x_i|^{2k}, \tag{1}$$

where $x_i \in \mathbb{C}$ is the input signal and $a_{2k+1,i}$, $k \in \{1,\dots,L\}$, are the unknown model coefficients for the i'th TX-chain, with $i \in \{1,\dots,MN\}$ corresponding to the antenna element located at panel $n = \lceil \frac{i}{M} \rceil$ and antenna element $m = mod(i-1, M)+1$. For the UEs, we assume linear TX-chain and RX-chain gains t_k^{U} and r_k^{U}.

During the DL transmission phase, the $K \times 1$ vector of symbols received at the UEs may be expressed as

$$\boldsymbol{y}_{\mathrm{U}} = \boldsymbol{R}_{\mathrm{U}} \boldsymbol{H}^{\mathrm{T}} \boldsymbol{f}(\boldsymbol{x}_{\mathrm{L}}) + \boldsymbol{n}_{\mathrm{U}}, \tag{2}$$

where $\boldsymbol{x}_{\mathrm{L}}$ is the $MN \times 1$ vector of input symbols to each LIS TX-chain, $\boldsymbol{n}_{\mathrm{U}} \sim \mathcal{CN}(\boldsymbol{0}, \mathrm{diag}(N_{0,\mathrm{U}_1},\dots,N_{0,\mathrm{U}_K}))$ models the AWGN at the UEs, $\boldsymbol{R}_{\mathrm{U}} = \mathrm{diag}(r_1^{\mathrm{U}},\dots,r_K^{\mathrm{U}})$, and $\boldsymbol{f} : \mathbb{C}^{M\times 1} \to \mathbb{C}^{M\times 1}$ is a vector-valued function modeling the non-linear response of the LIS TX-chains. We assume that the transmitted symbols are generated as

$$\boldsymbol{x}_{\mathrm{L}} = \boldsymbol{g}(\boldsymbol{W}\boldsymbol{s}), \tag{3}$$

where $\boldsymbol{s}$ is the $K \times 1$ vector of symbols intended for the UEs, $\boldsymbol{W}$ is the $MN \times K$ linear precoding matrix applied at the LIS, and $\boldsymbol{g} : \mathbb{C}^{MN\times 1} \to \mathbb{C}^{MN\times 1}$ is the non-linear vector-valued function associated to the DPD applied at each TX-chain.

Let us assume that the cross-talk between the LIS TX-chains is negligible so that $\boldsymbol{f}(\cdot)$, and correspondingly $\boldsymbol{g}(\cdot)$, are component-wise functions. Therefore, the input-output relation for the i'th element of $\boldsymbol{f}$ is directly given by (1). In a TDD system, the LIS selects $\boldsymbol{W}$ based on the UL CSI. During the UL channel estimation phase, the linear response of the UEs TX-chains and the LIS RX-chains affect the CSI, which compromises the reciprocity between the DL and UL effective channels. The $MN \times K$ UL channel is given by

$$\boldsymbol{H}_{\mathrm{UL}} = \boldsymbol{R}_{\mathrm{L}} \boldsymbol{H} \boldsymbol{T}_{\mathrm{U}}, \tag{4}$$

where $\boldsymbol{R}_{\mathrm{L}} = \mathrm{diag}(r_1, \ldots, r_{MN})$ and $\boldsymbol{T}_{\mathrm{U}} = \mathrm{diag}(t_1^{\mathrm{U}}, \ldots, t_K^{\mathrm{U}})$, and $\boldsymbol{H}$ corresponds to the $MN \times K$ reciprocal propagation channel matrix [7].

3 OTA-DPD and reciprocity Calibration

In this section, we generalize the OTA-based DPD and calibration method proposed in [8] for a LIS system with non-linear transceivers of an arbitrary order. We formulate the OTA-based method for a panel-based LIS scenario in the general case with and without inter-coupling coefficients knowledge. Then, we show that, in common panels-based LIS scenarios, the OTA-based method performance can degrade significantly due to the increased path-loss between some of the LIS panels, for which we need specific techniques to compensate for this performance loss.

Let us start by formulating the original OTA-based DPD and reciprocity calibration method for a LIS scenario. The OTA-based solution may be divided into three stages:

- First, the non-linear response of the LIS TX-chains, associated to $\boldsymbol{f}(\cdot)$, is estimated based on OTA mutual coupling measurements between the LIS antennas.
- Second, the DPD, associated to $\boldsymbol{g}(\cdot)$, is designed based on the estimated non-linear response.
- Third, reciprocity calibration is performed based on the DPD-linearized LIS TX-chains, after which effective DL precoding, associated to $\boldsymbol{W}$, would become available at the LIS.

In the first stage, each antenna element from all the panels transmits $N_{\mathrm{dpd}} \geq 2$ inter-antenna pilot signals to other panels. The signal received at the j'th antenna when the ℓ'th pilot, $\ell \in \{1, \ldots, N_{\mathrm{dpd}}\}$, is transmitted by the i'th antenna may be expressed as

$$y_{ij,\ell} = h_{ij} r_j \left(\sum_{k=0}^{L-1} a_{2k+1,i} \; x_{i,\ell} |x_{i,\ell}|^{2k} \right) + n_{ij,\ell}, \tag{5}$$

where h_{ij} is the mutual coupling gain between antennas i and j, $x_{i,\ell}$ is the ℓ'th pilot symbol transmitted by the i'th antenna, and $n_{ij,\ell} \sim \mathcal{CN}(0, N_0)$ models the measurement noise. For the non-linearity parameters, $a_{2k+1,i}$, associated to one TX-chain, there are $NM - 1$ relevant DPD measurements per pilot transmission. Thus, each of these measurements would share the same $a_{2k+1,i}$, but they would be related to a different complex gain r_j, associated to the linear response of the RX-chain from the respective receiving antenna. Since the the

coupling gain h_{ij} and the complex gains r_j are unknown, it is not possible to directly estimate the non-linearity parameters from this dataset. However, we may combine the measurements and estimate and scaled version of the desired coefficients. In general, the combined measurements are given by

$$\begin{aligned}\tilde{y}_{i,\ell} &= \sum_{j\neq i} w_{ij} y_{ij,\ell} \\ &= q_i \left(\sum_{k=0}^{L-1} a_{2k+1,i}\ x_{i,\ell} |x_{i,\ell}|^{2k} \right) + \tilde{n}_{i,\ell},\end{aligned} \tag{6}$$

where w_{ij} is the combining weights, and the uncertainty is now captured in the unknown parameter q_i, given by

$$q_i = \sum_{j\neq i} w_{ij} h_{ij} r_j. \tag{7}$$

The $N_{\text{dpd}} \times 1$ data vector $\tilde{\boldsymbol{y}}_i = [\tilde{y}_{i,1}, \ldots, \tilde{y}_{i,N_{\text{dpd}}}]^{\text{T}}$ may then be used to estimate the non-linearity parameters of each antenna up to the unknown factor q_i. Since our initial aim is to compensate the non-linear response of the TX-chains, this is still possible if we know the non-linear response up to an unknown linear factor, which would only have a linear effect after the non-linearity compensation [8]. In this case, the DPD would be designed as if the non-linearity parameters are $\theta_{k+1,i} = q_i a_{2k+1,i}$ for $k = 0, 1, \ldots, L-1$. We may thus rewrite the combined data vector as

$$\tilde{\boldsymbol{y}}_i = \boldsymbol{\Phi}_i \boldsymbol{\theta}_i + \tilde{\boldsymbol{n}}_i, \tag{8}$$

where $\boldsymbol{\theta}_i = [\theta_{1i}, \theta_{2i}, \ldots, \theta_{Li}]^{\text{T}}$ is the $L \times 1$ vector of parameters to be estimated, $\boldsymbol{\Phi}_i$ is the $N_{\text{dpd}} \times L$ known pilot matrix whose k'th column is given by

$$\boldsymbol{\phi}_{i,k} = [x_{i,1}|x_{i,1}|^{2k}, \ldots, x_{i,N_{\text{dpd}}}|x_{i,N_{\text{dpd}}}|^{2k}]^{\text{T}}. \tag{9}$$

$\tilde{\boldsymbol{n}}_i \sim \mathcal{CN}(\boldsymbol{0}, \varsigma_i \boldsymbol{I}_{N_{\text{dpd}}})$ is the resulting noise vector where

$$\varsigma_i = N_0 \sum_{j\neq i} |w_{ij}|^2. \tag{10}$$

Since the noise vector is independent and identically distributed Gaussian, the LS estimator is also the MVU estimator [9], and can be used to estimate the scaled non-linearity parameters as

$$\hat{\boldsymbol{\theta}}_i = (\boldsymbol{\Phi}_i^H \boldsymbol{\Phi}_i)^{-1} \boldsymbol{\Phi}_i^H \tilde{\boldsymbol{y}}_i. \tag{11}$$

In the second stage, the non-linearity parameters estimated in the previous stage are used to linearize the output via DPD, i.e., by adjusting $\boldsymbol{g}(\cdot)$ in (3). For analytical tractability, let us assume for now that $\boldsymbol{\theta}_i$ has been perfectly estimated from (8). The actual non-linearty to compensate is the nonlinear function given in (1), while the estimated non-linearity parameters in (11) characterize a different component-wise function given by

$$\tilde{f}_i(\boldsymbol{x}) = q_i f_i(\boldsymbol{x}). \tag{12}$$

We may thus express

$$\boldsymbol{f}(\boldsymbol{x}) = \boldsymbol{Q}^{-1}\tilde{\boldsymbol{f}}(\boldsymbol{x}), \tag{13}$$

where $\boldsymbol{Q} = \mathrm{diag}(q_1, \ldots, q_{MN})$.

Since the function $\tilde{\boldsymbol{f}}(\cdot)$ is fully characterized, we can find its inverse by using methods such as the postdistortion approach [10]. We may then select

$$\boldsymbol{g}(\cdot) = \tilde{\boldsymbol{f}}^{-1}(\cdot), \tag{14}$$

which is applied to the the transmitted symbols as described in (3). We consider a perfect inverse function here while the effects of an imperfect inversion is studied in the numerical results. The symbols transmitted through the reciprocal channel are then given by

$$\begin{aligned} \boldsymbol{f}(\boldsymbol{x}_{\mathrm{B}}) &= \boldsymbol{Q}^{-1}\tilde{\boldsymbol{f}}(\boldsymbol{g}(\boldsymbol{W}\boldsymbol{s}_{\mathrm{B}})) \\ &= \boldsymbol{Q}^{-1}\boldsymbol{W}\boldsymbol{s}_{\mathrm{B}}. \end{aligned} \tag{15}$$

Hence, applying the proposed OTA-DPD, results in an equivalent linear transmitter gain given by $\tilde{\boldsymbol{T}}_{\mathrm{B}} = \boldsymbol{Q}^{-1}$. Now that the transmitter is linear with an unknown complex gain, we can define a DL channel matrix, but substituting $\boldsymbol{T}_{\mathrm{B}}$ for $\tilde{\boldsymbol{T}}_{\mathrm{B}}$, so that reciprocity calibration methods as those presented in [6], [7] are directly applicable. However, we will show that the reciprocity calibration can be performed without the need for complex iterative methods.

In the third stage, OTA-based reciprocity calibration is performed considering the TX-chains previously linearized through the DPD linearization stage. To this end, each LIS antenna transmits $N_{\mathrm{cal}} \geq 1$ inter-antenna pilots to other antennas. The received symbols at the j'th antenna from the i'th antenna may be expressed as

$$y_{ij} = h_{ij} r_j \tilde{t}_i x_{ij} + n_{ij}, \tag{16}$$

where the variables have direct correspondence with those defined in (5), but substituting $a_{1,i}$ for $a_{1,i} = 1/q_i$ and having all other coefficients $a_{2k+1,i} = 0$. The measurements defined in (16) can be directly employed to estimate a product of unknown parameters, given by $\tau_{ij} \triangleq h_{ij} r_j \tilde{t}_i$. In fact, we may now

use the trivial MVU estimator, given by

$$\widehat{\tau_{ij}} = \mathbb{E}\left[\frac{y_{ij}}{x_{ij}}\right]. \tag{17}$$

where the expectation is taken over the N_{cal} pilot transmission. We are interested in finding the calibration coefficients $c_m = \tilde{t}_m / r_m$ from the estimates $\widehat{\tau_{ij}}$. In [7], it was noted that multiplying all the reciprocity parameters by a common scalar does not compromise the effectiveness of the reciprocity calibration.[10] Thus, we may select one of the calibration parameters, e.g., c_1, and normalize all the rest by that value. The resulting scaled calibration parameters may then be expressed as

$$\tilde{c}_m \triangleq \frac{c_m}{c_1} = \frac{r_1 \tilde{t}_m}{r_m \tilde{t}_1}. \tag{18}$$

Since we are capturing the non-reciprocity in the unknown parameters, the mutual coupling coefficients will be reciprocal per definition, i.e., $h_{ij} = h_{ji}$. The term $\tilde{c}_m$ corresponds to the ratio of the parameters τ_{ij} for $(i,j) \in \{(1,m),(m,1)\}$. Therefore, we can estimate $\tilde{c}_m$ as

$$\widehat{\tilde{c}_m} = \frac{\widehat{\tau_{m1}}}{\widehat{\tau_{1m}}}. \tag{19}$$

We have thus shown that we can estimate all the entries of the calibration matrix up to a constant, i.e., we can estimate $\tilde{\boldsymbol{C}} = \frac{1}{c_1}\boldsymbol{C}$, by means of simple linear estimators. While this method can be effectively used for DPD and calibration in LIS, the performance may be degraded significantly under specific channel conditions. In particular, the calibration performance depends heavily on the channel between the reference antenna and the rest of the LIS. Numerical results in section 5 show that under specific channel conditions, such as when inter-panel channels suffer from severe attenuation or shadowing, the performance of the OTA-based method can degrade significantly. In the next section, we propose three different techniques to improve the performance of the OTA-based method for panel-based LIS.

4 OTA-based techniques for panel-based LIS

As remarked above, the OTA-based method performance may degrade significantly under specific conditions in of the channel gain between the reference

[10] Note that this constant may be absorbed in the linear response of the UEs RXs-chain, given by $\boldsymbol{R}_{\text{U}}$.

antenna and the rest of the LIS. In this section, we propose specific techniques to improve the performance under such conditions.

To reduce dependence of the calibration error on the channel between the reference antenna and a particular antenna element, we can use the estimations $\widehat{\tau_{ij}}$ from another antenna as follows. Let us assume that the antenna 1 located on panel 1 is the reference antenna, and we are estimating the calibration coefficient $\widehat{\tilde{c}_m}$ for antenna m on panel n. If the channel conditions between these two antennas are poor, but there is an atenna on another panel, for example antenna i, which has a more favorable channel conditions to the reference antenna and antenna m, we can estimate $\widehat{\tilde{c}_m}$ as follows.

$$\widehat{\tilde{c}_m} = \frac{\widehat{r_i \tilde{t}_m}\,\widehat{r_1 \tilde{t}_i}}{\widehat{r_i \tilde{t}_1}\,\widehat{r_m \tilde{t}_i}} = \frac{\widehat{\tau_{mi}}\,\widehat{\tau_{i1}}}{\widehat{\tau_{1i}}\,\widehat{\tau_{im}}} \tag{20}$$

Numerical results in section 5 shows the effectiveness of this technique to further improve the performance of calibration.

While the above technique is shown to be effective for improving the performance of the OTA-based calibration for panel-based LIS, it still relies on the channel conditions between a specific antenna element from another panel and the local panel, and if for some reason this channel exhibit high attenuation, the performance improvement would be negligible. Alternatively, we can exploit the fact that unlike mutual coupling channels between antennas at different LIS-panels, intra-panel mutual coupling links are less likely to suffer form poor channel conditions due to being co-located and less dependent on the changes in the environment. Therefore, we propose to divide the reciprocity calibration stage from the original OTA-based method method into two steps, where the first step focuses on intra-panel calibration, and the second step focuses on inter-panel calibration.

In the first step, each panel performs an intra-panel, i.e., local, OTA-based DPD and calibration, while selecting one of the antenna elements on each panel as the reference. This results in a linearized transmitter gain, $\tilde{\boldsymbol{T}}_n$, and a local calibration matrix

$$\tilde{\boldsymbol{C}}_n = \alpha_n \tilde{\boldsymbol{T}}_n \boldsymbol{R}_n^{-1}, \tag{21}$$

where α_n is the unknown scalar associated to the reference antenna in the n'th panel. Since there are several unknown scalars α_n, the LIS panels cannot coherently serve the UEs through a fully calibrated channel. Therefore, a second step exploiting the inter-panel transmissions is needed to find the ratio between α_ns, which can then be used to combine all the local calibration matrices $\tilde{\boldsymbol{C}}_n$ into an overall calibration matrix $\tilde{\boldsymbol{C}}$. To find the ratios between α_ns, we consider two options, time averaging and spatial averaging.

In the case of time averaging, one antenna from each panel, e.g., antenna element i, sequentially transmits inter-panel pilots. During each inter-panel

pilot transmission, the received signal on an antenna element, e.g., antenna element j, associated to another panel, i.e., $\lceil \frac{j}{M} \rceil \neq \lceil \frac{i}{M} \rceil$, is given by

$$y_j = r_j g_{ij} \tilde{t}_i w_i s + n_j, \tag{22}$$

where g_{ij} is the propagation channel between antenna i and j, s is a pilot symbol (which can be selected as unity), and w_i is a linear precoder. The transmitting antenna has access to the its corresponding entry from the local calibration matrix which can be used for the precoder as

$$w_i = \frac{1}{\alpha_i} \tilde{t}_i^{-1} r_i. \tag{23}$$

Therefore, by sending N_α pilots over the same link to average out the noise, we can have an estimate of $\frac{1}{\alpha_i} \tilde{r}_j g_{ij} \tilde{r}_i$. By doing the same transmission in the opposite direction and taking into account the reciprocity of the propagation channel between the panels, i.e., $g_{ij} = g_{ji}$, we can have an estimate of $\frac{1}{\alpha_j} \tilde{r}_i g_{ji} \tilde{r}_j$. By dividing both estimates, we can then obtain an estimate for the ratio $\frac{\alpha_i}{\alpha_j}$. If we do the same process between a reference panel and all other panels, we will have the calibration matrix $\tilde{\boldsymbol{C}}$ as described above.

The above technique relies on time averaging to estimate α_n ratios, obtained throughout N_α pilot transmission between single antenna elements from different panels. Alternatively, we can exploit the complete inter-panel channels, i.e., employing the full M antennas at each panel, to find these ratios, which we refer to as spatial averaging. For this purpose, each M-antenna panel transmits M pilots to other panels. Combining the M pilot vectors into a matrix form, the matrix containing the received signal vectors at panel p can be written as

$$\boldsymbol{Y}_p = \boldsymbol{R}_p \boldsymbol{G}_{np} \tilde{\boldsymbol{T}}_n \boldsymbol{W}_n \boldsymbol{S} + \boldsymbol{N}_p, \tag{24}$$

where $\boldsymbol{G}_{np}$ is the $M \times M$ channel matrix between LIS-panels n and p, $\boldsymbol{S}$ is the $M \times M$ pilot matrix, and $\boldsymbol{W}_n$ is the $M \times M$ precoding matrix. Panel n can exploit the inverse of the local calibration matrix $\tilde{\boldsymbol{C}}_n^{-1}$ to precode the transmitted pilot as

$$\boldsymbol{W}_n = \tilde{\boldsymbol{C}}_n^{-1} = \frac{1}{\alpha_n} \tilde{\boldsymbol{T}}_n^{-1} \boldsymbol{R}_n. \tag{25}$$

If the transmitted pilot matrix $\boldsymbol{S}$ is invertible, we have

$$\boldsymbol{Y}_p \boldsymbol{S}^{-1} = \frac{1}{\alpha_n} \boldsymbol{R}_p \boldsymbol{G}_{np} \boldsymbol{R}_n + \boldsymbol{N}_p \boldsymbol{S}^{-1}. \tag{26}$$

By transmitting pilots in the opposite direction with the same procedure, we

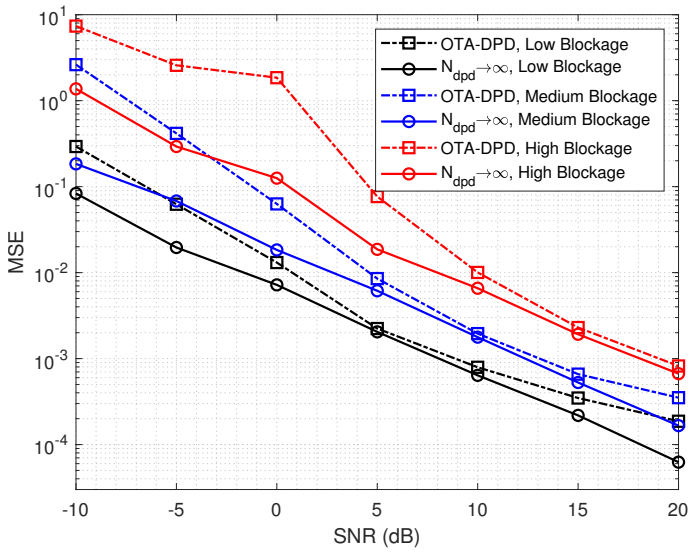

Figure 1: MSE of calibration matrix estimation using the proposed OTA-based DPD and Calibration under different levels of channel blockage.

have

$$\boldsymbol{Y}_n\boldsymbol{S}^{-1} = \frac{1}{\alpha_p}\boldsymbol{R}_n\boldsymbol{G}_{np}^T\boldsymbol{R}_p + \boldsymbol{N}_n\boldsymbol{S}^{-1}. \tag{27}$$

Therefore, $\boldsymbol{Z}_p = \boldsymbol{Y}_p\boldsymbol{S}^{-1}$ and $\boldsymbol{Z}_n = (\boldsymbol{Y}_n\boldsymbol{S}^{-1})^T$ are noisy versions of the same matrix $\boldsymbol{R}_p\boldsymbol{G}_{np}\boldsymbol{R}_n$ scaled by $1/\alpha_n$ and $1/\alpha_p$, respectively. By averaging over the M^2 entry-by-entry divisions of $\boldsymbol{Z}_n$ and $\boldsymbol{Z}_p$, we can find an accurate estimate of the ratio between α_n and α_p. The same process can be done between a reference panel and all other panels to effectively characterize the LIS calibration matrix.

5 Numerical Results

In this section, we present numerical results to study the performance of the OTA-based methods introduced in this paper. The LIS panels are placed on a $\sqrt{N} \times \sqrt{N}$ grid with equal distance of 5λ. Each panel corresponds to a square uniform planar array with inter-antenna spacing of 0.5λ. The BS TX-chains non-linearity parameters are obtained from an 11-th order polynomial model based on [11] for a Gallium Nitride (GaN) amplifier operating at 2.1 GHz at a sample rate of 200 MHz and a signal bandwidth of 40 MHz. The coupling gain model from [7] is adopted for intra-panel and inter-panel channel models. The complex gains associated to the RX-chains from each panel are modeled using the values in [7], which consider $r_m = 0.9+0.2\frac{M-m}{M}\exp(j2\pi m/M)$. To perform

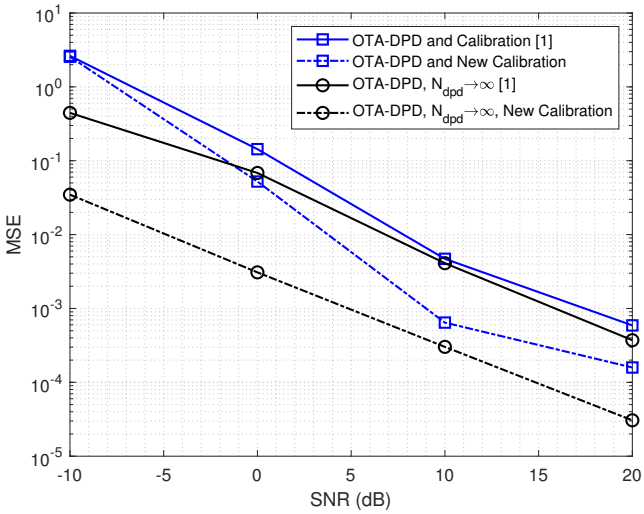

Figure 2: Average MSE of calibration matrix estimation using the proposed OTA-based DPD and Alternative Calibration.

the DPD, we generate a look-up table based on the OTA data to implement the inverse function of the non-linear response. For the mutual coupling channel gains, we have used the linear LS fit based on the measurements in [7]. We perform the simulations for different levels of a reference OTA link SNR, given by the RX-SNR for the link between the antennas with least mutual coupling gain. For the performance metric, we use the MSE of the calibration matrix $\tilde{\boldsymbol{C}}$, defined as

$$\text{MSE} = \mathbb{E}\left[\frac{\|\text{diag}(\tilde{\boldsymbol{C}} - \boldsymbol{C})\|^2}{MN}\right] \tag{28}$$

which represents the average estimation error of the calibration coefficients over all the antenna elements on the LIS.

In Fig. 1, we analyze the performance of the OTA-based method for a panel-based LIS scenario, where we have selected antenna 1 from panel 1 as the reference element, and assumed that panel 2 has a blockage in its channel to reference antenna causing an extra -6 dB, -10 dB, and -20 dB attenuation on the channel between panel 1 and 2. We can see that the estimation performance is degraded significantly for medium to high values of blockage. Therefore, alternative approaches and techniques are needed to improve the performance of the OTA-based method under such conditions.

In Fig. 2, we consider the high blockage case from previous figure, and apply the two-way OTA-based approach to improve the calibration performance. We have considered two cases, one with a limited length N_{DPD}, and one with an

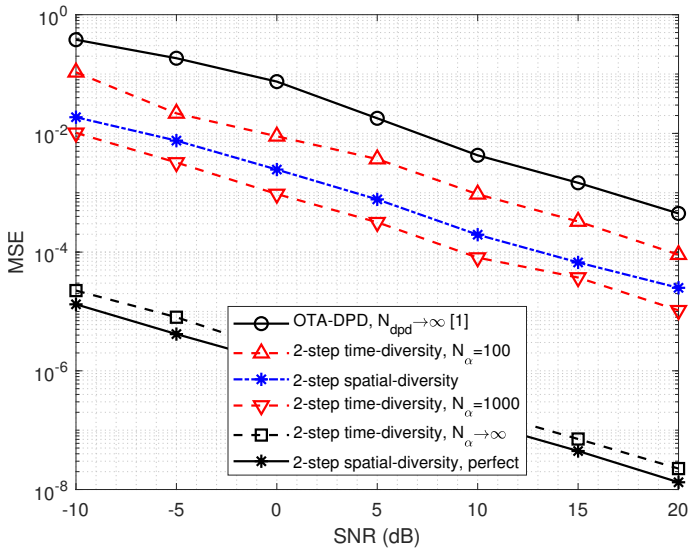

Figure 3: MSE of calibration matrix estimation using the proposed OTA-based DPD and Calibration under different levels of channel blockage.

ideal DPD. We can see that in both cases, the proposed method can boost the performance of the calibration matrix estimation, and the gain of adopting this technique is more significant if the DPD is more accurate in the first stage of the OTA-based method.

In Fig. 3, we have performed the second and third proposed technique which performs the calibration in two steps, one based on time-averaging and the other one on spatial-averaging. We have considered the same channel conditions as in Fig. 2, and performed the simulations for different lengths of N_α in the second step. We can see that, for a large enough N_α, the calibration error reduces significantly compared to the original OTA-based method. On the other hand, the spatial-averaging technique achieves a better performance for lower number of pilot transmission.

6 Conclusion

In this paper, we have proposed OTA-based reciprocity calibration and DPD schemes for LIS systems. In particular, we present an OTA-based method to perform DPD on a LIS with non-linear TX-chains modeled by an arbitrary-high order polynomial, followed by an OTA-based reciprocity calibration. We show that, although this method can be effective in general for LIS systems, its performance can be degraded under unfavorable channel conditions, such as severe

attenuation. In particular, in panel-based LIS, which is widely considered as a more practical implementation scheme for LIS, the original OTA-based method performance can be affected by unfavorable inter-panel channel conditions. For this scenarios, we propose two techniques to further improve the OTA-based DPD and calibration. Numerical results show that the proposed techniques can improve the performance of the OTA-based methods significantly, effectively enabling the OTA-DPD and calibration for practical panel-based LIS systems.

References

[1] S. Hu, F. Rusek, and O. Edfors, "Beyond massive MIMO: The potential of data transmission with large intelligent surfaces," *IEEE Transactions on Signal Processing*, vol. 66, no. 10, pp. 2746–2758, 2018.

[2] C. Huang et al., "Holographic MIMO surfaces for 6g wireless networks: Opportunities, challenges, and trends," *IEEE Wireless Communications*, vol. 27, no. 5, pp. 118–125, 2020.

[3] E. Björnson, L. Sanguinetti, H. Wymeersch, J. Hoydis, and T. L. Marzetta, "Massive MIMO is a reality—what is next?: Five promising research directions for antenna arrays," *Digital Signal Processing*, vol. 94, pp. 3–20, 2019, Special Issue on Source Localization in Massive MIMO.

[4] A. Pereira, F. Rusek, M. Gomes, and R. Dinis, "Deployment strategies for large intelligent surfaces," *IEEE Access*, vol. 10, pp. 61 753–61 768, 2022.

[5] S. Hu, H. Wang, and M. C. Ilter, "Design of near-field beamforming for large intelligent surfaces," *IEEE Transactions on Wireless Communications*, vol. 23, no. 1, pp. 762–774, 2024.

[6] H. Wei, D. Wang, H. Zhu, J. Wang, S. Sun, and X. You, "Mutual coupling calibration for multiuser massive MIMO systems," *IEEE Transactions on Wireless Communications*, vol. 15, no. 1, pp. 606–619, 2015.

[7] J. Vieira, F. Rusek, O. Edfors, S. Malkowsky, L. Liu, and F. Tufvesson, "Reciprocity calibration for massive MIMO: Proposal, modeling, and validation," *IEEE Transactions on Wireless Communications*, vol. 16, no. 5, pp. 3042–3056, 2017.

[8] A. Sheikhi, O. Edfors, and J. V. Alegría, "Over-the-air DPD and reciprocity calibration in massive MIMO and beyond," *IEEE Wireless Communications Letters*, pp. 1–1, Aug. 2025.

[9] S. M. Kay, *Fundamentals of statistical signal processing: estimation theory*. USA: Prentice-Hall, Inc., 1993.

[10] C. Eun and E. Powers, "A new volterra predistorter based on the indirect learning architecture," *IEEE Transactions on Signal Processing*, vol. 45, no. 1, pp. 223–227, 1997.

[11] "Further elaboration on PA models for NR," *document 3GPP TSG-RAN WG4, R4-165901, Ericsson, Stockholm, Sweden*, Aug. 2016.

Paper VII

Power Scaling Laws for Radio Receiver Front Ends

In this paper, we combine practically verified results from circuit theory with communication-theoretic laws.As a result, we obtain closed-form theoretical expressions linking fundamental system design and environment parameters with the power consumption of analog front ends (AFEs) for communication receivers.This collection of scaling laws and bounds is meant to serve as a theoretical reference for practical low power AFE design.We show how AFE power consumption scales with bandwidth, *SNDR*, and *SIR*.We build our analysis based on two well established power consumption studies and show that although they have different design approaches, they lead to the same scaling laws.The obtained scaling laws are subsequently used to derive relations between AFE power consumption and several other important communication system parameters, namely, digital modulation constellation size, symbol error probability, error control coding gain, and coding rate.Such relations, in turn, can be used when deciding which system design strategies to adopt for low-power applications.For instance, we show how AFE power scales with environment parameters if the performance is kept constant and we use these results to illustrate that adapting to fading fluctuations can theoretically reduce AFE power consumption by at least 20x.

In *IEEE Transactions on Circuits and Systems I: Regular Papers*, vol. 68, no. 5, pp. 2183-2195, May 2021.

1 Introduction

Low power consumption is one of the main design targets for communication receivers, and its importance is especially high when it comes to wireless devices, which are often battery-powered and therefore energy-limited. At the same time, receivers also need to satisfy some performance requirement, such as minimum throughput and maximum bit error rate (BER). Designing receivers that jointly meet power consumption and performance criteria tends to be predominantly based on the experience of hardware designers. Additionally, more often than not, receiver designs are optimized based on the worst-case scenario of operation (the most adverse possible combination of environment conditions under which satisfying performance must be delivered). The latter, conservative design methodology in particular is what prevents hardware designs from exploiting their full potential for low-power operation.

It would be of significant interest to be able to theoretically predict how much power would be consumed by a receiver with certain performance requirements, with all system and environment constraints taken into consideration. Such a result would serve as a benchmark and motivation for both practical hardware and system design, an indicator of how low the power consumption can really be driven. If combined with the knowledge of the statistical properties of environment variables, it can also provide a measure of how much power can be saved if the receiver adapts to the communication environment.

The analog front end (AFE) (the chain of analog signal blocks of the receiver excluding the oscillator) typically has a defining impact on the overall performance of the receiver, while also consuming a substantial portion of its power. Therefore, the achieved performance gain by scaling the AFEs power consumption is an important aspect in designing low-power receivers. As an example, it can help the designer to know how much power can be saved by relaxing the AFE design when techniques such as error-control coding are adopted in the system. It can also determine the saved power when the receiver is made adaptive to communication environment conditions (e.g. channel fading or out-of-band interference), compared to a design based on worst-case conditions.

The theoretical analysis of the relation between analog circuit power consumption and performance appears not to have gained a lot of attention in the scientific community. The relation between power consumption and performance for individual analog blocks is analyzed in [1] and [2]. It is found that power consumption grows linearly with the dynamic range of an analog circuit block[11]. Analysis of this relation for a chain of analog blocks becomes rather involved because performance metrics for the entire chain exhibit a complex dependence on gain, noise and linearity properties for individual blocks. Moreover, there are practically infinitely many combinations of per-block parameters

[11]The definitions of dynamic range differ slightly between these two papers. As will be shown, here we adhere to the definition given in [1] and adopted in [3].

that satisfy the performance requirements for the entire chain, with each combination resulting in a unique power consumption. A sensible approach is then to find the combination that yields the minimum power consumption, which then makes it possible to reveal the implicit or explicit connection between the performance requirement and the obtained optimal power consumption. In [3], [4], [5], [6], this approach is adopted, with the focus being mostly on how to conveniently model the power-performance relation for individual blocks and how to solve the power optimization problem. The analysis in [5] extends the ideas from [4], with the power-performance relation also being given some treatment in the context of communication systems.

There also exists a body of academic work [7], [8], [9], [10], [11] that examines the topic of environment-adaptive AFEs and receivers, with the focus being primarily on practical hardware implementations. It is demonstrated that adaptive receivers are implementable, and various implementation strategies are suggested. Furthermore, measured power numbers from these designs indicate that substantial power reduction is attainable if environment-adaptive receiver techniques are adopted.

What is found to be largely missing in the existing literature is a work that takes the power-performance laws from circuit theory and combines them with classical results from communication theory to formulate joint circuit-communication-theoretical laws of system behavior [12]. With such laws at hand, system design initial questions can be addressed in a precise and immediate fashion, with less educated guessing or iterative hardware redesign and simulation/measurement cycles.

Here we aim at bridging this gap between circuit and communication theory. The idea is to obtain theoretical expressions that will describe how optimal AFE power consumption scales with important system and environment parameters such as signal-to-noise-and-distortion ratio (SNDR), signal to interference ratio (SIR) and bandwidth. We first derive our scaling laws from a known relation between performance and minimum power consumption for AFEs which is presented and verified in actual hardware implementations [3]. In this design approach, noise and linearity of the AFE blocks are optimized to give the minimum total power consumption. We also consider another design approach presented in [5], [6] where AFE power consumption is minimized by deriving the optimum gain and linearity for the AFE blocks. Although [3], [5] and [6] are different in the sense of their AFE power consumption model, design approach, and the proposed optimum power consumption, we are able to derive the same scaling laws from both of them, which suggests that the laws are both general and widely applicable to different AFEs.

The AFE power consumption relations are modified so that they can be

[12] A rare example is [5], but with the analysis limited only to the connection between throughput and relative level of the out-of-band blocking signal.

seamlessly combined with communication-theoretic laws. The results are then employed in finding closed-form expressions for AFE power scaling with QAM constellation size, symbol error rate and error-control coding gain, which are further used to decide on appropriate system-level strategies for low-power design. In another line of results, we obtain power-law type relations between AFE power and environment parameters. These are combined with fading and blocker statistics, yielding important theoretical bounds on average power savings of environment-adaptive front ends, which demonstrate that substantial power savings are possible if the environment-adaptive design approach is adopted.

2 Optimal power consumption of AFEs

Let us observe a chain of analog circuit blocks that form the front end of a communications receiver. One example of such a chain can be the direct conversion receiver with the structure LNA - downconversion mixer - channel select filter - variable gain amplifier. While the direct conversion receiver is given as an example, we emphasize that the forthcoming analysis holds for any type of receiver chain.

Each of the blocks in the chain can be qualitatively characterized by noise and linearity properties (serving as performance quantifiers) and by an associated power consumption. Noise performance is commonly quantified by noise power spectral density $\overline{V}_{\mathrm{N}}^2$ $\left[\mathrm{V}^2/\mathrm{Hz}\right]$, and linearity as V_{IIP3}^2 $[\mathrm{V}^2]$, the input-referred third-order intercept voltage squared. Additionally, we denote by F_{AFE} the total noise factor and by $V_{\mathrm{IIP3,\,AFE}}^2$ the total IIP3 voltage squared of the AFE chain. These are usually set by performance requirements dictated by the digital baseband. Given F_{AFE} and $V_{\mathrm{IIP3,\,AFE}}^2$, one would preferably like to select $\overline{V}_{\mathrm{N}}^2$ and V_{IIP3}^2 of individual blocks such that the power consumption of the entire chain is minimized.

In order to solve this task, we first need to look into the nature of the relation between the performance quantifiers and power consumption for each block. The dynamic range of a block with index j is defined as

$$DR_j \triangleq \frac{V_{\mathrm{IIP3},j}^2}{\overline{V}_{\mathrm{N},j}^2}. \tag{1}$$

As presented [1] and [3], for a wide range of the most common front-end blocks, the power consumption of a circuit is linear with the dynamic range and can be modeled as

$$P_j = \kappa_j DR_j, \tag{2}$$

where κ_j is a proportionality factor that can be taken as a natural figure-of-

merit for analog blocks.

Starting from this simple but powerful relation, the authors in [3] have devised a method of finding $\overline{V}_{\mathrm{N},j}^2$ and $V_{\mathrm{IIP3},j}^2$ that results in minimum power consumption of the whole AFE chain. Although proof is given in [3] that relation (2) holds for standard CMOS circuits (such as a common-source stage LNA, a double-balanced Gilbert cell mixer and an OTA-C baseband filter), the results of the optimization are valid for any chain of analog blocks that satisfy (2) and are hence not limited only to CMOS circuits. Moreover, [3] provides a comparison of theoretically optimal $\overline{V}_{\mathrm{N},j}^2$ and $V_{\mathrm{IIP3},j}^2$ with measured noise PSD and IIP3 from an actual "hand-optimized" Bluetooth receiver implementation, with a good match between the two. This hardware verification naturally extends to our analysis, which considers optimally designed AFEs in communication system settings.

What is important for our analysis is that the method from [3] provides the connection between the optimal power consumption of the entire AFE, denoted by P_{AFE}, and $V_{\mathrm{IIP3,\ AFE}}^2$ and F_{AFE}, which reads [3, eq. (60)]

$$P_{\mathrm{AFE}} = \frac{V_{\mathrm{IIP3,\ AFE}}^2}{(F_{\mathrm{AFE}} - 1)kTR_{\mathrm{ref}}} \left(\sum_{j=1}^{M} \sqrt[3]{\kappa_j} \right)^3, \tag{3}$$

where k is Boltzmann constant, T temperature in Kelvin and R_{ref} a reference resistance, usually 50 Ω. Remarkably, the optimal power consumption of the chain is independent of power/voltage gains of individual blocks. If we are to use (3) for drawing conclusions on the system-level behaviour of receivers, it would be convenient to "translate" these result to system designer parlance, so that it features power-related parameters:

- received wanted signal power at the antenna - p_{S},
- total input-referred thermal noise power - p_{N},
- power of the out-of-band (OOB) interfering signal at the antenna - p_{I}. [13]

As a first step, we can relate p_{N} and F_{AFE} through

$$p_{\mathrm{N}} = kTBF_{\mathrm{AFE}}, \tag{4}$$

with B being the noise-equivalent bandwidth of the system, and IIP3 power

[13] The results (1) and consequently, (3) were derived with the assumption of a two-tone interference model. For the sake of consistency, we maintain this model throughout our analysis, and p_{I} then denotes the total power of the two interfering tones. However, we conjecture that the obtained trends hold even in the case of modulated interferers.

and voltage are related by

$$p_{\text{IIP3, AFE}} = \frac{V_{\text{IIP3, AFE}}^2}{R_{\text{ref}}}. \tag{5}$$

In order to directly assess the impact of third-order nonlinearity on system performance, we need to relate the IIP3 to p_{IM3}, the power of the in-band third-order intermodulation (IM3) distortion. A well-known relation linking p_{IIP3}, p_{I} and p_{IM3} reads [12]

$$p_{\text{IIP3}} = \sqrt{\frac{p_{\text{I}}^3}{p_{\text{IM3}}}}. \tag{6}$$

For the purpose of notational convenience, we denote the AFE power coefficient in (3) as

$$\kappa_{\text{circuit}} \triangleq \left(\sum_{j=1}^{M} \sqrt[3]{\kappa_j} \right)^3 \tag{7}$$

and use (4), (5) and (6) in conjunction with (3) to obtain

$$P_{\text{AFE}} = B \frac{p_{\text{I}}^{3/2}}{p_{\text{N}} \sqrt{p_{\text{IM3}}}} \frac{F_{\text{AFE}}}{F_{\text{AFE}} - 1} \kappa_{\text{circuit}}. \tag{8}$$

For the analysis at hand it is convenient to define the power ratio of intermodulation distortion and noise

$$\alpha_{\text{IM3}} \triangleq \frac{p_{\text{IM3}}}{p_{\text{N}}}, \tag{9}$$

which combined with (8) yields

$$P_{\text{AFE}} = \frac{B}{\sqrt{\alpha_{\text{IM3}}}} \left(\frac{p_{\text{I}}}{p_{\text{N}}} \right)^{3/2} \frac{F_{\text{AFE}}}{F_{\text{AFE}} - 1} \kappa_{\text{circuit}}, \tag{10}$$

with $p_{\text{I}} > 0$, which follows from the constraint $V_{\text{IIP3, AFE}}^2 > 0$. The obtained formula for AFE power consumption in (10) will be used as a basis for deriving simple but very useful scaling laws, as presented in the following section.

3 Scaling laws of AFE power consumption

A holistic receiver system design benefits greatly from the availability of closed form relations between receiver power consumption and other system parameters. This way, a mathematically tractable analysis of the tradeoffs encountered

during receiver system design is made possible. When it comes to real-world hardware, obtaining such relations is not a trivial task, and there always exists a tradeoff between the accuracy of the functional dependencies and their analytical tractability. Ideally, they should appear in form of simple power scaling laws. It turns out that (10), under some realistic assumptions, can yield such simple relations. The advantage of using (10) for this purpose is that it is soundly grounded in circuit theory which has also been verified against real-life receiver designs in [3], so it enables striking a good balance between accuracy, simplicity and theoretical rigour.

We derive and formulate these power scaling laws in Section III-A. Ideally, we would like to validate the laws individually by circuit verification and measurement setups. This is however an overwhelming task and beyond the scope of this paper. What we can do to support and validate the laws nonetheless is to show that they are not specific to the design approach and models in [3]. For that purpose, in Section III-B, we will show that the same scaling laws can be derived for a different AFE design approach and power consumption model. Additionally, in Section III-C, we apply our laws to reported noise and nonlinearity parameters of an existing front end implemented in 180 nm CMOS. Power scaling predicted by our laws is in line with the power numbers reported for the front end, which further corroborates the validity of our analysis.

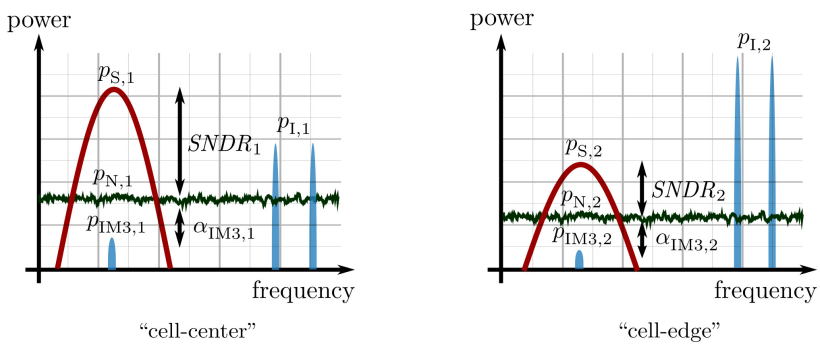

Figure 1: Illustration of system parameters for the cell center scenario (left: strong wanted signal, weak OOB interference, high *SNDR* requirement) and cell edge scenario (right: weak wanted signal, strong OOB interference, low *SNDR* requirement).

3.1 Deriving the Scaling Laws

To start with, a performance metric is needed that will provide a link between baseband metrics, like bit error rate (*BER*), via power-related system parameters, with circuit parameters F_{AFE} and $V^2_{\mathrm{IIP3,\,AFE}}$. A commonly used such

metric is the signal-to-noise-and-distortion ratio[14], which is defined as

$$SNDR \triangleq \frac{p_{\mathrm{S}}}{p_{\mathrm{N}} + p_{\mathrm{IM3}}} = \frac{p_{\mathrm{S}}}{(1 + \alpha_{\mathrm{IM3}})\, p_{\mathrm{N}}}. \tag{11}$$

Now we focus our attention on four fundamental receiver design parameters, namely, *SNDR* and B (the values of which are determined by the particular application), and p_{S} and p_{I} (which describe the environment and are generally stochastic). The values of the fundamental parameters define distinct application-environment scenarios. We structure our analysis around a pair of such scenarios: an initial (pre-scaling) and a target (post-scaling) scenario. An illustration of the relations between parameters of importance for an example scenario pair is given in Fig. 1. For each of the two scenarios–under practical constraints on parameter values–we assume that an AFE with minimal power consumption is designed using the procedure described in [3]. Further, we assume that $\kappa_{\mathrm{circuit}}$ is the same for both pre- and post-scaling circuits. In practice, this usually implies that the two front ends being compared consist of the same number of blocks having identical, or very similar, structure. Our aim is relating the scaling of fundamental parameter values between the two scenarios and the scaling of optimal front end power consumption. To this end, we label variables corresponding to pre-scaling and post-scaling scenarios with indices 1 and 2, respectively. The scaling of the optimal power consumption is denoted as

$$\varsigma_{\mathrm{P}} \triangleq \frac{P_{\mathrm{AFE},2}}{P_{\mathrm{AFE},1}}. \tag{12}$$

The scaling factors of bandwidth, *SNDR*, signal and interference power are defined analogously to ς_{P} and denoted respectively as ς_{B}, $\varsigma_{\mathrm{SNDR}}$, ς_{S} and ς_{I}. By using (10) and (11), the scaling of front end power reads

$$\varsigma_{\mathrm{P}} = \varphi\ \delta\ \varsigma_{\mathrm{B}} \varsigma_{\mathrm{SNDR}}^{3/2}\ \varsigma_{\mathrm{I}}^{3/2}\ \varsigma_{\mathrm{S}}^{-3/2}, \tag{13}$$

where, for analytical convenience, we have introduced the factors

$$\varphi \triangleq \frac{F_{\mathrm{AFE},2}}{F_{\mathrm{AFE},1}} \frac{F_{\mathrm{AFE},1} - 1}{F_{\mathrm{AFE},2} - 1} \tag{14}$$

[14]It is commonly assumed that the third-order distortion is the dominant nonlinear impairment in analog systems. Therefore, along with thermal noise, we consider it a determining factor of system performance. All other possible impairments, such as second-order distortion, flicker noise, phase noise–either in-band or due to reciprocal mixing–are through appropriate design assumed to be dominated by thermal noise and third-order distortion in all scenarios considered.

and

$$\delta \triangleq \sqrt{\frac{\alpha_{\mathrm{IM3,1}}}{\alpha_{\mathrm{IM3,2}}}} \left(\frac{1+\alpha_{\mathrm{IM3,2}}}{1+\alpha_{\mathrm{IM3,1}}} \right)^{3/2}. \tag{15}$$

Expression (13) is a universal tool for calculating AFE power scaling and can be used for all application-environment scenarios, under the condition that the corresponding AFEs are implementable. However, one does need to use (13) in a careful and structured way due to interdependencies between the fundamental parameters ($SNDR, B, p_{\mathrm{S}}, p_{\mathrm{I}}$) and noise-distortion ratio α_{IM3}, system-level design parameters ($p_{\mathrm{N}}, p_{\mathrm{IM3}}, p_{\mathrm{IIP3}}$) and circuit-level parameters ($F_{\mathrm{AFE}}, V_{\mathrm{IIP3}}^2$). More specifically, for a particular scenario, $SNDR$, B, p_{S}, p_{I} and α_{IM3} will through (6), (9) and (11) yield p_{N}, p_{IM3} and p_{IIP3}, which through (4) and (5) result in F_{AFE} and V_{IIP3}^2. Combining F_{AFE} from pre- and post-scaling scenarios yields φ from (14), noise-distortion ratios α_{IM3} give the value of δ from (15), and the values of fundamental parameters result in respective scaling ratios, all of which is combined in (13) for the final result.

3.2 Validation of the Scaling Laws: Theory

In order to show that the power scaling laws are both general and widely applicable to different AFEs, we also consider another AFE design approach presented in [5], [6] and show that the same scaling laws can be derived for them as well. To avoid misunderstanding, we use superscript * to explicitly show that a parameter is based on the results from [5], [6]. In [5], [6], the power consumption minimization is conducted by optimizing the gain and linearity of each AFE block. It is shown that the the power consumption of each block in the AFE can be modeled as

$$P_j^* = \theta_j A_j p_{\mathrm{IIP3,j}} \tag{16}$$

where θ_j is the effective figure of merit (EFOM), A_j is the block power gain, and $p_{\mathrm{IIP3,j}}$ is the IIP3 power. This is a generic model for individual blocks power consumption and the value of EFOM depends on the IC technology, circuit topology etc [5], [6]. Considering this model for each AFE block, the problem of minimizing the total power consumption of the AFE is formulated and solved analytically using Lagrangian multiplier method. This optimization is performed over A_j and $p_{\mathrm{IIP3,j}}$, for given individual noise figures, total AFE gain, non-linearity, and noise figure which defines a constraint on A_j via the Friis' Formula. The optimal values of $p_{\mathrm{IIP3,j}}$ and A_j are calculated and the

final solution for minimum power consumption is

$$P^*_{\mathrm{AFE}} = p_{\mathrm{IIP3,\ AFE}} \left(\sqrt{\theta_M A_{\mathrm{AFE}}} + \sqrt{\frac{F_w}{F_{\mathrm{AFE}} - f_1}} \right)^2, \tag{17}$$

where

$$F_w = \left(\sum_{j=1}^{M-1} \sqrt[3]{\theta_j \left(f_{j+1} - 1 \right)} \right)^3 \tag{18}$$

and f_i denotes the noise figure of the $i-th$ block. By following the same steps and using the same definitions that turned (3) into (10), the power consumption P^*_{AFE} in (17) can be reformulated as

$$P^*_{\mathrm{AFE}} = \frac{B}{\sqrt{\alpha_{\mathrm{IM3}}}} \left(\frac{p_{\mathrm{I}}}{p_{\mathrm{N}}} \right)^{3/2} F_{\mathrm{AFE}}\ \Gamma, \tag{19}$$

where

$$\Gamma = \left(\sqrt{kT\theta_M A_{\mathrm{AFE}}} + \sqrt{\frac{kTF_w}{F_{\mathrm{AFE}} - F_1}} \right)^2. \tag{20}$$

One should note that the optimal power consumption results in (10) and (19) are different for two reasons. Firstly, they are based on different modeling of individual blocks power consumption. Secondly, (10) is derived by optimizing the power consumption over noise and linearity of AFE blocks, whereas (19) is obtained by optimizing the power with respect to the individual blocks gains and linearity. By exploiting the definitions in (11) and (12), the power scaling law for P^*_{AFE} reads

$$\varsigma_{P^*} = \tau\ \delta\ \varsigma_{\mathrm{B}} \varsigma_{\mathrm{SNDR}}^{3/2}\ \varsigma_{\mathrm{I}}^{3/2}\ \varsigma_{\mathrm{S}}^{-3/2}, \tag{21}$$

where

$$\tau \triangleq \frac{F_{\mathrm{AFE},2}}{F_{\mathrm{AFE},1}} \frac{\Gamma_2}{\Gamma_1}. \tag{22}$$

By comparing (13) and (21), it can be seen that no matter which design approach one chooses to optimize the AFEs power consumption, the power scaling behaviour with *SNDR*, bandwidth, p_{S}, and p_{I} are the same, which suggests that the scaling laws are general and can be widely applied to different AFEs.

Table 1: Measured numbers and environment parameter values for the three test scenarios in [7]: relaxed, high-linearity demanding (HLD), and low-noise demanding (LND).

Scenario	Test conditions		Front end parameters at optimal working point		
	p_S (dBm)	p_I (dBm)[15]	F (dB)	IIP3 (dBm)	Current (mA)
Relaxed	-75	-35	11.5	-7	11.2
HLD	-68	-25	18.2	3.7	20.6
LND	-87.5	N/A	4.8	-12.2	17.6

3.3 Validation of the Scaling Laws: Published Performance

Another way of checking the validity of our scaling laws is to test them on measured performance parameters of an actual front end implementation. Here, we opt to use the numbers for the adaptive front end presented in [7]. This direct-conversion front end, implemented in 180 nm CMOS, is capable of attaining a wide range of gain, noise figure and IIP3 values that are efficiently traded off with power consumption using dynamic biasing of LNA, mixer and analog baseband filter. The architecture presented in [7] also supports real-time adaptation to a wide range of p_S, p_I values and SNDR requirements, guaranteeing that the operating point with minimum power consumption for a given setting is always found. All in all, the design setup in [7] fits very well with the setup of our analysis which makes the (very well documented) measurement results from [7] a prime choice for testing our findings.

There are three scenarios described in [7]: relaxed, high-linearity demanding (HLD), and low-noise demanding (LND). Table 1 lists out the reported noise figure, IIP3 and current consumption for optimal working points for each of the scenarios, together with environment parameters for the scenarios. In all scenarios, optimal points are found such that they satisfy the SNDR requirement of 12.7 dB. More details about the data can be found in [7, Table II, Fig. 23, Sect. VII].

Numbers reported in Table 1 are used as input to our power scaling law (13) for all three combinations of optimal designs (scaling from HLD setup to relaxed, etc.). The obtained scaling results, compared with actual power

[15] A modulated blocker with power $p_B = -40/-30$ dBm is accompanied by a single-tone blocker with 5 dB larger power, resulting in SNDR approximately equal to one obtained through (6) and (11) with $p_I = -35/-25$ dBm.

Table 2: Ratios of power consumption between pairs of optimal designs: measured values (final column in Table I) vs. values predicted by the scaling law.

Power Scaling	Measured [7]	Predicted by the scaling law (13)
$\varsigma_{P,relaxed/HLD}$	0.54	0.42
$\varsigma_{P,relaxed/LND}$	0.64	0.51
$\varsigma_{P,LND/HLD}$	0.85	0.83

scaling as reported in Table 1, are given in Table 2. One probable reason for the discrepancy between the measured power scaling and the one predicted by the scaling law is individual elements in the chain not having optimal noise figure and linearity as per the recipe in [3] (which is understandable since the approach in [3] was never claimed to be followed in [7], and per-block optimality would be hard to achieve anyway in a tunable design). Regardless of this, the scaling law gives an overall good prediction of achievable downscaling of power when switching from one operating point of the front end to the other.

3.4 Detailed discussion of the scaling laws

In order to isolate the scaling of power with only one of the fundamental parameters, we assume that the value of the parameter in question scales between the scenarios while other parameters remain constant. In this way, we obtain a restricted set of application-environment scenarios with high practical relevance, examined in detail in Section 4. Additionally, in all scenarios it is assumed that pre- and post-scaling α_{IM3} values are the same, i.e. that input-referred thermal noise and third-order distortion levels are kept at a constant ratio. Available literature on systematic receiver design suggests that in practice, the value of α_{IM3} is chosen to be small so that the third-order distortion is much weaker than the thermal noise, with the choice being consistent over different application-performance scenarios [12, Ch. 13]. This consistency over scenarios is in line with our constant-α_{IM3} assumption.

The laws describing the scaling of front end power with fundamental parameters are given in Table 3, expr. (23)-(26). Note that the constraints on the scaling of B also double as explicit design requirements. It is well known that the power consumption of standard analog blocks scales linearly with bandwidth [2]. The bandwidth scaling law in (23) demonstrates that the linear power-bandwidth relation extends also to a chain of analog blocks. The SNDR scaling law in (24) serves as a fundamental relation for analyzing power-

Table 3: Collection of fundamental scaling laws for analog front end power consumption. Each of the four rows of the table, corresponding to a particular scaling law, also provides a comprehensive list of application-environment constraints (columns 1-4), together with a list of resulting system/circuit design requirements (columns 4-8) needed for scaling laws to hold in practical implementations, obtained through (4)-(6).

Constraints			Design requirements					Power scaling	Properties of φ
Performance	Environment		System			Circuit			
$SNDR_2 =$	$p_{\mathrm{S},2} =$	$p_{\mathrm{I},2} =$	$B_2 =$	$p_{\mathrm{N},2} =$	$p_{\mathrm{IM3},2} =$	$F_2 =$	$V^2_{\mathrm{IIP3},2} =$		
$SNDR_1$	$p_{\mathrm{S},1}$	$p_{\mathrm{I},1}$	$\varsigma_{\mathrm{B}} B_1$	$p_{\mathrm{N},1}$	$p_{\mathrm{IM3},1}$	$\frac{F_1}{\varsigma_{\mathrm{B}}}$	$V^2_{\mathrm{IIP3},1}$	$\varsigma_{\mathrm{P}} = \varphi \varsigma_{\mathrm{B}}$ (23)	$\varphi < 1, \quad 0 < \varsigma_{\mathrm{B}} < 1$ $\varphi \geq 1, \quad 1 \leq \varsigma_{\mathrm{B}} < F_1$
$\varsigma_{\mathrm{SNDR}} SNDR_1$	$p_{\mathrm{S},1}$	$p_{\mathrm{I},1}$	B_1	$\frac{p_{\mathrm{N},1}}{\varsigma_{\mathrm{SNDR}}}$	$\frac{p_{\mathrm{IM3},1}}{\varsigma_{\mathrm{SNDR}}}$	$\frac{F_1}{\varsigma_{\mathrm{SNDR}}}$	$\sqrt{\varsigma_{\mathrm{SNDR}}} V^2_{\mathrm{IIP3},1}$	$\varsigma_{\mathrm{P}} = \varphi \varsigma_{\mathrm{SNDR}}^{3/2}$ (24)	$\varphi < 1, \quad 0 < \varsigma_{\mathrm{SNDR}} < 1$ $\varphi \geq 1, \quad 1 \leq \varsigma_{\mathrm{SNDR}} < F_1$
$SNDR_1$	$\varsigma_{\mathrm{S}} p_{\mathrm{S},1}$	$p_{\mathrm{I},1}$	B_1	$\varsigma_{\mathrm{S}} p_{\mathrm{N},1}$	$\varsigma_{\mathrm{S}} p_{\mathrm{IM3},1}$	$\varsigma_{\mathrm{S}} F_1$	$\frac{V^2_{\mathrm{IIP3},1}}{\sqrt{\varsigma_{\mathrm{S}}}}$	$\varsigma_{\mathrm{P}} = \varphi \varsigma_{\mathrm{S}}^{-3/2}$ (25)	$\varphi < 1, \quad \varsigma_{\mathrm{S}} > 1$ $\varphi \geq 1, \quad \frac{1}{F_1} < \varsigma_{\mathrm{S}} \leq 1$
$SNDR_1$	$p_{\mathrm{S},1}$	$\varsigma_{\mathrm{I}} p_{\mathrm{I},1}$	B_1	$p_{\mathrm{N},1}$	$p_{\mathrm{IM3},1}$	F_1	$\varsigma_{\mathrm{I}}^{3/2} V^2_{\mathrm{IIP3},1}$	$\varsigma_{\mathrm{P}} = \varsigma_{\mathrm{I}}^{3/2}$ (26)	$\varphi = 1$

performance tradeoffs in analog receiver design, as analyzed more in-depth in Sections 4.2 and 4.3. The received power scaling law in (25) will be useful in analyzing power savings of a front end that adapts to a fluctuating received signal level while maintaining constant performance, as will be presented in Section 4.4. By defining the signal-to-interference ratio $SIR = p_S/p_I$, the scaling law in (26) can be reformulated as $\varsigma_P = \varsigma_{SIR}^{-3/2}$, where ς_{SIR} is the scaling of the *SIR*. This result is of importance when analyzing the power consumption of an AFE that dynamically adapts its linearity to the interference level while maintaining constant performance. A detailed theoretical analysis of such an AFE will be given in Section 4.5.

Laws (23) - (25) are characterized by the fact that the underlying scaling asks for tuning of the noise figure, which in turn makes the parameter φ scaling-dependent. More specifically, for ς_*, where $* \in (\mathrm{B}, \mathrm{SNDR})$,

$$\varphi = \frac{F_{\mathrm{AFE},1} - 1}{F_{\mathrm{AFE},1} - \varsigma_*}, \tag{27}$$

whereas for ς_S we have

$$\varphi = \frac{F_{\mathrm{AFE},1} - 1}{F_{\mathrm{AFE},1} - \frac{1}{\varsigma_S}}. \tag{28}$$

The dependence of φ on the scaling parameters is outlined in the last column of Table 3. The constraint $\varphi > 0$, i.e. the fact that it is physically impossible to have an AFE with $F < 1$ imposes theoretical limitations on the values of scaling ς. Furthermore, dependence of φ on ς causes deviations from the ideal scaling of power (linear with bandwidth or following the 3/2 power law in case of *SNDR* and received power). In order to have proper scaling laws, it is necessary for φ to be independent of ς. This condition is approximately satisfied in two cases:

- $F_{\mathrm{AFE},1} \gg 1 \Rightarrow \varphi \approx 1$;
- $\varsigma_B, \varsigma_{SNDR} \ll 1$ or $\varsigma_S \gg 1 \Rightarrow \varphi \approx \frac{F_{\mathrm{AFE},1}-1}{F_{\mathrm{AFE},1}}$.

At first, it can appear that the set of scenarios in which power scaling laws (23)-(25) are close to ideal ($\varphi \approx 1$) is based on such a restrictive sequence of assumptions that their practical relevance is questionable. However, a closer look reveals that all the assumptions we used are commonplace in practice and/or of high practical interest for low-power design. To start with, $F_{\mathrm{AFE},1} \gg 1$ is typical for worst-case AFE designs with a large OOB blocking signal present [12, Ch. 13], [13]. Moreover, radical scaling down of system bandwidth (e.g. going from a wideband to a narrowband system), drastic downscaling of *SNDR* requirement (due to e.g. use of power-efficient transmission techniques) or adaptation to wanted signal power that becomes much larger than worst-case

(reference sensitivity) due to fading fluctuations are all use-cases of interest for low-power applications [14], [15]. It can be shown that the parameter τ is also scaling-independent in each of the proposed scaling laws.

4 Ramifications of the scaling laws

The scaling laws presented in the previous section constitute a set of tools which prove to be very useful in the design of receivers where power consumption is of high importance. Namely, as the laws in the preceding section formally show, the power consumption of the AFE can be lowered by using one (or more) of the following techniques:

- Intentionally degrading the bit/symbol error rate (*SER*), which consequently reduces the *SNDR* requirement;
- Keeping *BER* or *SER* constant while applying some transmission technique that allows for lower *SNDR* (e.g. use of error control coding);
- Keeping the *SNDR* constant while making the AFE reconfigurable so that it adapts to the changes in the environment (e.g. fading level fluctuations, OOB interference level).

The scaling laws serve as a basis for estimates of the extent of power savings that can be achieved in the AFE if the aforementioned techniques are applied. System designers can then decide on which techniques to incorporate in their systems, and hardware designers are provided with general guidelines on how to increase the power efficiency of circuit designs.

4.1 Preliminaries: limitations on hardware relaxation

Throughout the analysis that follows, we consider AFEs designed for different target values of noise and distortion. When it comes to realistic hardware designs, however, it is reasonable to assume that the range of these values is limited. Naturally, there are fundamental physical constraints on the minimum noise (or distortion) level that a circuit can deliver, but, equally important, there are also upper bounds, imposed by either functionality or technology process constraints [2]. Hence, in line with considerations from the previous section, we establish a permissible tuning range μ that applies to both noise figure and IP3. It is defined as the value of scaling of noise/linearity for which, given all architectural and physical limitations, the following holds:

- The noise figure F_{AFE} can be degraded from the reference value $F_{\mathrm{AFE},1}$ to a maximum value of $F_{\mathrm{AFE},2} = \mu F_{\mathrm{AFE},1}$,

- It is possible to degrade IP3 from the reference value $V^2_{\mathrm{IIP3},1}$ to a minimum possible value of $V^2_{\mathrm{IIP3},2} = \frac{1}{\sqrt{\mu}} V^2_{\mathrm{IIP3},1}$.

Apart from functionality or process constraints, data rate requirements of the overlying data transmission can also impose limits on how much the front-end hardware can be degraded. More specifically, in some applications (such as voice calls) there is a minimum requirement on data rate, and performance cannot be compromised beyond what is necessary to support the minimum data rate. More details on this topic are given in [16].

4.2 Power- and energy-efficient AFEs through intentional degradation of performance, uncoded case

In this section, we focus on systems using M-QAM without any error control coding. With the aim of saving power, System 2 either uses a lower QAM constellation order M or operates at a higher symbol error probability P_{e}, formally, $M_2 \leq M_1$ or $P_{\mathrm{e},2} \geq P_{\mathrm{e},1}$. As indicated in Section 3, the two systems are otherwise assumed to use the same bandwidth (and thus the same symbol rate R_{s}), are affected by same OOB interference level and experience the same wanted signal power.

We assume that the classical matched-filter detector is employed at the receiver. If the thermal Gaussian noise dominates the IM3[16], i.e. $\alpha_{\mathrm{IM3}} \ll 1$, the matched-filter receiver is optimal in the sense of maximum aposteriori detection. Under these circumstances, an upper bound on *SER* for a square M-QAM ($M = 2^{2k},\ k \in \mathbb{N}$) can be determined [18], which yields the inequality

$$SNDR \leq \rho \frac{M-1}{3\log_2 M} \left[Q^{-1}\left(\frac{P_{\mathrm{e}}}{4}\right)\right]^2, \tag{29}$$

where $\rho = R_{\mathrm{b}}/B$ is the spectral efficiency of the uncoded system (R_{b} is the information bitrate) and $Q^{-1}(\cdot)$ the inverse of the upper tail probability function of a unit-variance Gaussian random variable. At high *SNDR*s, the upper bound in (29) is tight.

We proceed by constructing a ratio of the upper bounds from (29) that apply to the two distinct scenarios under analysis. This ratio is given as

$$\varsigma_{\mathrm{SNDR}} \geq \frac{M_2 - 1}{M_1 - 1} \left[\frac{Q^{-1}\left(P_{\mathrm{e},2}/4\right)}{Q^{-1}\left(P_{\mathrm{e},1}/4\right)}\right]^2, \tag{30}$$

[16] In case that nonlinear distortion is non-negligible, it can to a certain extent be estimated and cancelled in digital baseband, following the so-called "dirty-RF" approach [17]. This would improve the performance at the cost of increased power consumption.

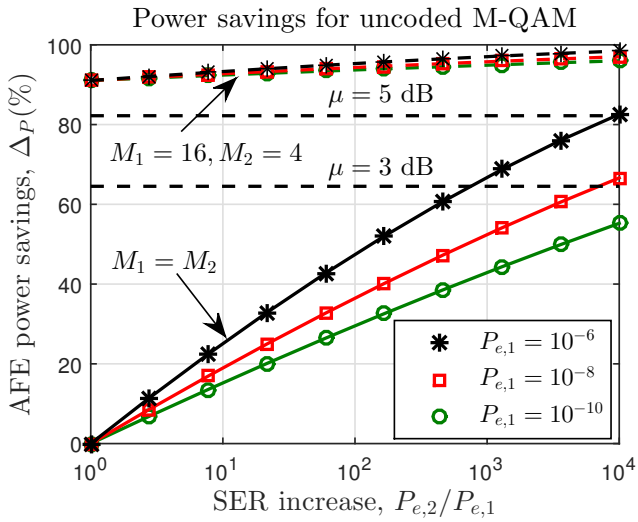

Figure 2: Savings in AFE power consumption when symbol error probability and/or constellation order are degraded, for uncoded square QAM. For limited flexibility AFEs, the savings cap at values indicated by horizontal dashed lines.

where the fact that B is the same for the two systems is used. Taking into account the practical limits on noise/linearity scaling, discussed in Section 4.1, along with law (24), the achievable scaling of AFE power, $\varsigma_{\mathrm{P,\,a}}$, is found to be

$$\varsigma_{\mathrm{P,\,a}} < \max\{\varsigma_{\mathrm{SNDR}}^{3/2}, \mu^{-3/2}\}. \tag{31}$$

By combining this together with (30) and the fact that the slack of the *SER* upper bound increases with decreasing *SNDR*, we obtain the upper bound on the achievable AFE power downscaling:

$$\varsigma_{\mathrm{P,\,a}} \leq \max\left\{\left(\frac{M_2-1}{M_1-1}\right)^{3/2}\left[\frac{Q^{-1}\left(P_{\mathrm{e},2}/4\right)}{Q^{-1}\left(P_{\mathrm{e},1}/4\right)}\right]^3, \mu^{-3/2}\right\}. \tag{32}$$

In other words, the AFE power can be decreased by *at least* the value of the right hand side of (32). For large *SNDR*s and large $F_{\mathrm{AFE},1}$, the bound is tight.

The obtained bound enables the derivation of laws describing the performance-power consumption tradeoff in systems using uncoded QAM when there are no limits on *SNDR* tuning, $\mu \to \infty$. In one case, we keep P_{e} constant but reduce the number of bits per symbol $b = \log_2 M$ by $\Delta_{\mathrm{b}} = b_1 - b_2$. This yields

$$\varsigma_{\mathrm{P}} < \left(\frac{M_2}{M_1}\right)^{3/2} = 2^{-\frac{3}{2}\Delta_{\mathrm{b}}}. \tag{33}$$

Therefore, the power consumption of an infinitely flexible AFE decreases at least exponentially with the difference in bits/symbol, or equivalently, with the difference in raw uncoded bitrate. In another setting, we assume M is the same between the two systems but target *SER* is increased from $P_{\mathrm{e},1}$ to $P_{\mathrm{e},2}$. Using the bound $Q(x) \leq e^{-x^2/2}$, we get

$$\varsigma_{\mathrm{P}} \leq \left[\frac{Q^{-1}\left(P_{\mathrm{e},2}/4\right)}{Q^{-1}\left(P_{\mathrm{e},1}/4\right)}\right]^3 \leq \left(\frac{1-1.66\log_{10} P_{\mathrm{e},2}}{1-1.66\log_{10} P_{\mathrm{e},1}}\right)^{3/2}. \tag{34}$$

Assuming additionally that the order of magnitude $\omega_{\mathrm{e}} = \log_{10} P_{\mathrm{e}}$ of *SER* is low enough, we get

$$\varsigma_{\mathrm{P}} \leq \left(\frac{\omega_{\mathrm{e},2}}{\omega_{\mathrm{e},1}}\right)^{3/2}. \tag{35}$$

In other words, we can say that the power consumption of the AFE with infinite flexibility scales at least as $\mathcal{O}\left(\omega^{3/2}\right)$.

For convenience of presenting numerical results, we define the percentage savings of AFE power

$$\Delta_{\mathrm{P}} \triangleq 100(1-\varsigma_{\mathrm{P}}) \quad [\%]. \tag{36}$$

These savings, represented in Fig. 2 imply that, if presented with a choice of whether to sacrifice bitrate or error rate in order to save power in the receiver, we should in general opt for the former. Taking into account hardware design limitations, substantial savings are achievable even when it is possible to scale down the *SNDR* by as little as e.g. 3 dB; naturally, in order to harvest the full potential of the savings, the AFE should be made as flexible as hardware constraints permit.

In order to provide a completely fair comparison between the systems, degradation of the performance and reduction of power consumption should be considered jointly. A joint metric for performance and power consumption is needed for this task, and one is readily found in the form of energy efficiency

$$\eta_{\mathrm{AFE}} \triangleq \frac{R_{\mathrm{b}}}{P_{\mathrm{AFE}}} \quad [\mathrm{bits/J}]. \tag{37}$$

In the case when constellation size M changes but error rate P_{e} stays fixed and with unlimited flexibility, the ratio of the two efficiencies is

$$\frac{\eta_{\mathrm{AFE},2}}{\eta_{\mathrm{AFE},1}} = \frac{1}{\varsigma_{\mathrm{P}}}\frac{R_{\mathrm{b},2}}{R_{\mathrm{b},1}} \geq \left(\frac{M_1-1}{M_2-1}\right)^{3/2}\frac{\log_2 M_2}{\log_2 M_1}. \tag{38}$$

From here we can conclude that, for a fixed P_{e}, η_{AFE} will always improve if the size of the square QAM constellation is reduced. We note that, in the case

when η is defined with respect to *transmit signal power*, it is a well known fact that the energy efficiency increases with decreasing QAM constellation size [18]. However, we show that this energy efficiency property of QAM constellations extends to the case of *power consumption of analog receiver hardware*.

4.3 Power- and energy-efficient AFEs through use of error control coding

Error control coding (ECC) techniques are used to improve reliability (error rate performance) of communication systems when *SNDR* is kept fixed. Seen from another angle, when the error rate is constrained to be the same for uncoded and coded systems, coding can be used to improve the power efficiency of communication systems as a consequence of relaxed requirements on *SNDR*. Here we analyze the case when this potential for increased power efficiency is used by the receiver (it can also be used by the transmitter, or be distributed between the two).

Power efficiency gain of coded systems is usually expressed in terms of the coding gain g_c. By assuming that $\alpha_{\mathrm{IM3}} \ll 1$, we can approximate the PSD of the sum of all impairments by additive white Gaussian noise PSD N_0 and define the ratio E_b/N_0 of energy per bit E_b and N_0. Given the E_b/N_0 values required to achieve the same error probability with and without coding, the coding gain is defined as

$$g_\mathrm{c} \triangleq \frac{(E_\mathrm{b}/N_0)_{\mathrm{uncoded}}}{(E_\mathrm{b}/N_0)_{\mathrm{coded}}}. \tag{39}$$

For finding the achievable AFE power reduction, we need to connect the coding gain g_c with the *SNDR* downscaling $\varsigma_{\mathrm{SNDR}}$, where $SNDR_1$ corresponds to the uncoded system and $SNDR_2$ to the coded one. We do this by assuming that the system bandwidth is equal for both systems, which is a reasonable assumption for all applications where bandwidth is a limited resource. Consequently, using ECC will reduce spectral efficiency from ρ_{uncoded} to $\rho_{\mathrm{coded}} = r_\mathrm{c}\rho_{\mathrm{uncoded}}$, where r_c is the coding rate. We additionally use the fact that $E_\mathrm{b}/N_0 = SNDR/\rho$ to obtain

$$\varsigma_{\mathrm{SNDR}} = \frac{r_\mathrm{c}}{g_\mathrm{c}}, \tag{40}$$

and the associated achievable AFE power reduction (cf. (31)) is then given by

$$\varsigma_{\mathrm{P,\,a}} < \max\left\{\left(\frac{r_\mathrm{c}}{g_\mathrm{c}}\right)^{3/2}, \mu^{-3/2}\right\}. \tag{41}$$

Table 4: System parameters and theoretical power numbers for AFEs and decoders in systems using error control coding

Information bitrate [Mbps]	Code	r_c	g_c @ $BER = 10^{-3}$ [dB]	P_{AFE} [mW]	P_{dec} [mW]	$P_{AFE} + P_{dec}$ [mW]	Total EE [Gbits/J]
26.7	uncoded	-	-	35 (**ref. [19]**)	0	35	0.76
13.35	convolutional (7, 5)	1/2	3.1 (**ref. [20]**)	4.26	0.56 (**ref. [20]**)	4.82	2.77
8.89	turbo N = 6144	1/3	6.1 (**ref. [21]**)	0.82	8.3 (**ref. [21]**)	9.12	0.96

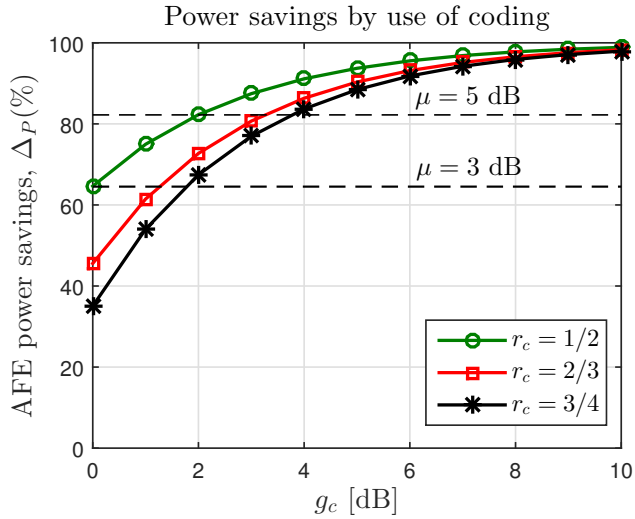

Figure 3: Savings in AFE power consumption coming from use of error control coding. For limited flexibility AFEs, the savings cap at values indicated by horizontal dashed lines.

The savings function (36) for systems using coding is illustrated in Fig. 3. An important observation to make here is that a large portion of the power savings (in absolute power terms) is harvested by low to intermediate coding gains. Additional absolute power savings that are brought about by employing stronger codes with larger coding gains are only marginal. This point is further elaborated in the follow-up.

Numerical example

here we provide a system design scenario that serves to illustrate the potential savings of AFE power consumption when ECC is used, and also to give some system-level design guidelines. We assume a system with passband bandwidth of 40 MHz, BPSK modulation and single carrier transmission using raised cosine pulses with roloff of 0.5 over a flat-faded channel. Total receiver power (AFE + decoder) is calculated for three versions of the system: one uncoded and two with different types of ECC. If coding is used, the AFE design is relaxed accordingly. Power consumption values used here are ballpark quantities based on actual hardware designs. For the decoders, the power numbers obtained from the designs are modified to match the information bitrate (assuming that a linear extrapolation of decoder power consumption is possible at lower bitrates) and scaled to the same process (65 nm CMOS) and voltage (1.2 V).

System parameters and calculated power numbers are listed out in Table 4.

The use of coding allows for relaxation of the AFE by making it noisier and less linear, so its power consumption is ideally reduced as per (41). However, the overhead in power consumption stemming from the channel decoders also needs to be taken into account in order for the full story to be told. It can be seen that in the case of the system using convolutional codes (CC), a massive reduction of AFE power comes with a relatively small power overhead for the decoding. Using turbo codes allows for further reductions of AFE power compared to the CC case, but at a cost of a relatively high decoding power overhead, which is due to the iterative nature of the turbo decoder. Dividing the information bitrate with total power consumption yields the energy efficiency of the receiver, which indicates that coding indeed enables an improvement of the receiver energy efficiency, but the best strategy is to use "light" codes, with moderate coding gains and simpler decoders. We note that the relation between error control coding and overall energy efficiency of the system is a long-standing research topic, examined both empirically and theoretically in, e.g., [22] and [23]. However, these papers analyze the combination of decoding power and *transmit power*, whereas we focus on the *total power of the receiver*, that is, the sum of decoding power and power consumed by supporting analog hardware.

As for the energy efficiency of the AFE alone, it can be quickly shown that it always improves with coding. This is done by setting up the ratio of energy efficiencies (37) for the coded and uncoded system, which gives

$$\frac{\eta_{\text{coded}}}{\eta_{\text{uncoded}}} = \frac{1}{\varsigma_{\text{P}}} \frac{R_{\text{b},coded}}{R_{\text{b},uncoded}} = \frac{r_{\text{c}}}{\varsigma_{\text{P}}} > \frac{g_{\text{c}}^{3/2}}{\sqrt{\varsigma_{\text{P}}}} \tag{42}$$

in the case of infinite AFE flexibility. But the obtained ratio is always > 1 for $g_{\text{c}} > 1$ (for a properly designed code operating at a large enough *SNDR*).

Overall, the results in this section lead to the conclusion that low power applications that harness error control coding gains for the goal of relaxing the receiver favor simple codes with modest coding gains and simpler decoders over more powerful codes that ask for more involved decoding algorithms. If we, on the other hand, consider solely the AFE, it can be shown that coding always improves its energy efficiency.

4.4 Power-efficient AFEs through adaptation to fading

In this section, we assume a single carrier transmission over a frequency flat wireless channel. Due to fading, received power p_{S} will be time varying and can be well described as a random process, $p_{\text{S}}(t) = \beta\phi(t)$, where β subsumes the transmit power, transmit and receive antenna gains, pathloss and large-scale fading, which are all assumed constant in this context. Additionally, $\phi(t) = |h(t)|^2$, where $h(t)$ is a zero-mean unit-variance complex Gaussian random process, i.e. the small-scale fading adheres to the common Rayleigh fading

model. It is well known that $\phi(t)$ has an exponential pdf, $f_\Phi(\phi) = e^{-\phi}, \phi \geq 0$. [24]

A common design parameter for wireless systems is the outage probability Ω, defined as the probability that the normalized fading power ϕ falls below some minimum acceptable level $\phi_{\min}$ [24]. In conjunction with $\phi_{\min}$, an outage *SNDR* is usually defined, which represents the minimum *SNDR* that provides acceptable performance. Using $\phi_{\min}$ and $SNDR_{\min}$, a minimum (worst-case) thermal noise level is calculated as

$$p_{\mathrm{N,\ min}} = \frac{\beta \phi_{\min}}{(1 + \alpha_{\mathrm{IM3}})\, SNDR_{\min}}. \tag{43}$$

Therefore, a minimum noise level $p_{\mathrm{N,\ min}}$ and a minimum third-order distortion $p_{\mathrm{IM3,\ min}}$ need to be delivered by the AFE at least at the time instants where $\phi(t) = \phi_{\min}$. For all practical purposes, however, AFEs are built so that they deliver minimum noise and distortion *all the time*. Since the outage probability Ω is typically chosen to be quite low (for example, on the order of 10^{-2}), this means that for the vast majority of time, *SNDR* delivered by these worst-case designs will be much larger than $SNDR_{\min}$ and performance far better than the minimum acceptable one.

Unless the variations in *SNDR* are leveraged for increasing throughput (via adaptive modulation and coding), having the front end operate in a fixed manner represents a waste of power. If a fixed throughput and error rate are acceptable for a particular application, front end noise and linearity can be tuned to track the variations of received power and maintain constant *SNDR* (effectively "equalizing" the channel). As indicated by results of Section 3, such an approach would result in a reduction of power consumed by the front end.

We now turn to quantifying this reduction. Firstly, in line with considerations in Section 4.1, it is reasonable to assume that the noise level in an adaptive front end can be tuned only in a limited range $\left(p_{\mathrm{N,\ min}},\ \mu p_{\mathrm{N,\ min}}\right)$ while being kept constant at the range boundaries for too small/large values of $\phi(t)$. The same logic extends to adapting the distortion level by means of tuning the nonlinearity, which yields the allowed range for the distortion of $\left(p_{\mathrm{IM3,\ min}},\ \mu p_{\mathrm{IM3,\ min}}\right)$. The adaptation rule for thermal noise in a fading-adaptive front end with limited adaptation range is given in Table 5, with the most important parameters of interest illustrated in Fig. 4. Using relations (4) - (6), $\alpha_{\mathrm{IM3},1} = \alpha_{\mathrm{IM3},2}$ and the set of constraints from the third row of Table 3, these rules can be translated to feature circuit design parameters. We further denote by $P_{\mathrm{AFE,\ wc}}$ the power consumption of the non-adaptive, worst-case front end architecture, designed to deliver $p_{\mathrm{N,\ min}}$ and $p_{\mathrm{IM3,\ min}}$ throughout. Taking into account scaling law (25), the power consumption of the adaptive front end $P_{\mathrm{AFE}}(t)$ normalized by $P_{\mathrm{AFE,\ wc}}$ depends on $\phi(t)$ and is given in Table 5. From there, assuming that $\phi(t)$ is an ergodic process, the expected value of

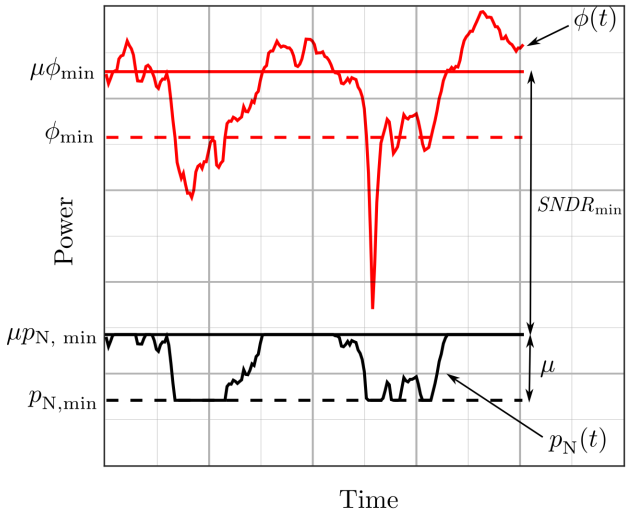

Figure 4: Illustration of time-varying fading and system parameters for the fading-adaptive front end design

power scaling ς_{P} for the adaptive front end can be calculated as

$$\begin{aligned}\mathbb{E}\{\varsigma_{\mathrm{P}}\} \leq\ & 1\ -\ e^{-\phi_{\min}}\ +\ \mu^{-3/2}e^{-\mu\phi_{\min}} \\ & + 2\phi_{\min}e^{-\phi_{\min}}\left(1-\frac{1}{\sqrt{\mu}}e^{(1-\mu)\phi_{\min}}\right) \\ & + 2\phi_{\min}^{3/2}\left[\Gamma\left(\frac{1}{2},\mu\phi_{\min}\right)-\Gamma\left(\frac{1}{2},\phi_{\min}\right)\right],\end{aligned} \tag{44}$$

where $\Gamma(a,x)$ is the upper incomplete gamma function [25].

Achieving continuous tuning of noise and linearity can be challenging in practical implementations. Apart from adapting to the environment, the issue of random PVT (process, voltage, temperature) variations also needs to be accounted for. In fact, process variations can be considered as a major obstacle in implementing adaptive circuits, because real-world adaptive circuits may need to correlate electrical parameters like bias voltage and currents to non-linearity and noise parameters. There exist solutions for jointly solving these practical problems, such as the one presented in [10], where LNAs with orthogonally tunable noise and linearity are combined with a simple online optimization algorithm, yielding substantial power savings.

An alternative way of tackling this issue is to form a bank of front ends that are optimally designed for different noise and linearity settings. During

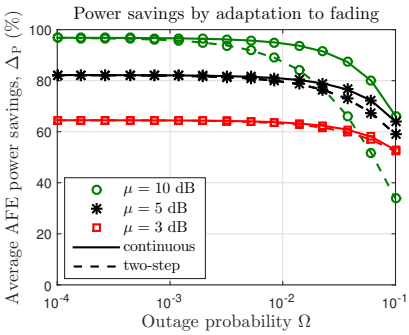

(a) Average power savings of continuous

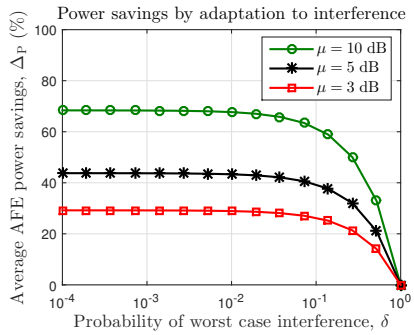

(b) Average power savings of two-step (51)

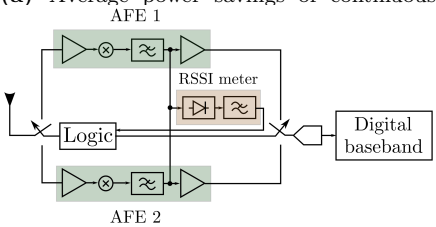

(c) Example architecture for two-step fading-adaptation. AFE 1 has low noise figure and high IP3; AFE 2 high noise figure and low IP3.

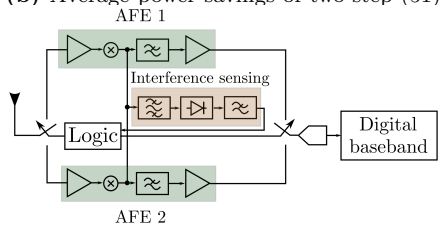

(d) Example architecture for two-step interference-adaptation. AFE 1 has high IP3; AFE 2 low IP3.

Figure 5: Theoretical power savings and conceptual illustrations of architectures for adaptive receivers

operation, the receiver would switch between different front ends based on the measured received power, keeping one front end active and switching off the rest. In the most basic case, such a bank would consist of only two front ends. A switching rule for this two-step adaptive front end that guarantees $SNDR \geq SNDR_{\min}$ can be defined as

$$p_N = \begin{cases} p_{N,\,\min}, & \phi(t) \leq \mu\phi_{\min}, \\ \mu p_{N,\,\min}, & \phi(t) > \mu\phi_{\min}. \end{cases} \tag{45}$$

Average power downscaling for the two-step front end is found to be

$$\mathbb{E}\{\varsigma_P\}_{\text{two-step}} \leq 1 - \left(1 - \mu^{-3/2}\right) e^{-\mu\phi_{\min}}. \tag{46}$$

Average power scaling for flexible and two-step front ends is converted to average savings as per (36) and shown in Fig. 5a. When the tuning range μ is small, normalized signal power $\phi(t)$ is either in outage or above $\mu\phi(t)$ for most of the time, so continuous and two-step front ends have similar power savings. As the tuning range increases, more power can be saved, but in the case of large

Table 5: Noise tuning parameters and normalized power consumption of fading-adaptive AFEs

Fading level	$p_{\mathrm{N}}(t)$	$\frac{P_{\mathrm{AFE}}(t)}{P_{\mathrm{AFE,\ wc}}}$	$\frac{SNDR}{SNDR_{\mathrm{min}}}$
$\frac{\phi(t)}{\phi_{\mathrm{min}}} \leq 1$	$p_{\mathrm{N,\ min}}$	$= 1$	< 1
$1 < \frac{\phi(t)}{\phi_{\mathrm{min}}} \leq \mu$	$\frac{\beta\phi(t)}{\left(1+\alpha_{\mathrm{IM3}}\right)SNDR_{\mathrm{min}}}$	$< \left[\frac{\phi(t)}{\phi_{\mathrm{min}}}\right]^{-3/2}$	$= 1$
$\frac{\phi(t)}{\phi_{\mathrm{min}}} > \mu$	$\mu p_{\mathrm{N,\ min}}$	$< \mu^{-3/2}$	> 1

outage probability, $\phi(t)$ is rarely larger than $\mu\phi(t)$. This means that in the case of the two-step front end, the noisy, nonlinear, low power front end rarely gets activated and the power savings are significantly lower compared to continuous adaptation. In any case, the obtained savings are substantial[17], which should serve as a motivation for implementing fading-adaptive front ends in practice. In the case of two-step adaptation, such implementations can have an appealing simplicity. As means of illustration, we provide a high-level conceptual sketch of how they might look like, shown in Fig. 5c. Under the condition that the channel select filter removes most of the OOB interference, the wanted signal power can be measured in the baseband by a simple power detector. This information, properly calibrated to account for in-band gains, can be used by a logic circuit which will drive the switching between the two front ends.

4.5 Power-efficient AFEs through adaptation to out-of-band interference

The analysis of practical implications of the AFE power scaling laws is concluded by looking into how much power can be saved if the AFE adapts its linearity to the OOB interferer level. It is assumed that the wanted signal, whose level does not change, is accompanied by two interferers with total power p_{I} and equal, slowly time varying amplitudes, so that they can be well approximated by two tones.

We analyze a receiver structure that is able to adjust its linearity in two discrete steps and in doing so, adapt to the fluctuating interference level. To this end, suppose that we have two analog front end designs at our disposal. One of them is designed for the worst-case interference level $p_{\mathrm{I,\ wc}}$ (a value commonly prescribed in communication standards) and its linearity is equal to $p_{\mathrm{IIP3,wc}}$. On the other hand, the IP3 of the other design has been degraded down

[17] We reiterate that the front end power can be scaled down by *at least* the values given by the right hand side of (44) and (46), i.e. Fig. 5a illustrates a lower bound on possible savings!

to the limits of implementability and is equal to $p_{\mathrm{IIP3,wc}}/\sqrt{\mu}$ [18]. Otherwise, the bandwidth and noise figure of the two front ends are the same.

The task of the receiver is to track the interference power and switch between the two front ends so that a minimum performance requirement is always satisfied, $SNDR \geq SNDR_{\min}$, or equivalently, that the intermodulation distortion is always kept below a certain level:

$$p_{\mathrm{IM3}} \leq p_{\mathrm{IM3,wc}} = \frac{p_{\mathrm{I,\,wc}}^3}{p_{\mathrm{IIP3,wc}}^2}. \tag{47}$$

Condition (47) is met by a receiver which will tune its IP3 by switching between the described front ends in line with the following rule:

$$p_{\mathrm{IIP3}} = \begin{cases} p_{\mathrm{IIP3,wc}}, & \frac{1}{\sqrt[3]{\mu}} p_{\mathrm{I,\,wc}} < p_{\mathrm{I}} \leq p_{\mathrm{I,\,wc}}, \\ \frac{1}{\sqrt{\mu}} p_{\mathrm{IIP3,wc}}, & p_{\mathrm{I}} \leq \frac{1}{\sqrt[3]{\mu}} p_{\mathrm{I,\,wc}}, \end{cases} \tag{48}$$

with one front end with desired linearity being on and the other one switched off.

In order to characterize average power savings, it is not necessary to have the knowledge of the actual distribution of p_{I}. It is sufficient to assume that the probability of $p_{\mathrm{I}} > p_{\mathrm{I,\,wc}}$ is negligible (which is why this case is not covered by the adaptation rule), and that only the probability δ of interference being "high" is known, i.e.

$$\begin{aligned} \Pr\left\{ \frac{1}{\sqrt[3]{\mu}} p_{\mathrm{I,\,wc}} < p_{\mathrm{I}} \leq p_{\mathrm{I,\,wc}} \right\} &= \delta, \\ \Pr\left\{ p_{\mathrm{I}} \leq \frac{1}{\sqrt[3]{\mu}} p_{\mathrm{I,\,wc}} \right\} &= 1 - \delta. \end{aligned} \tag{49}$$

As in the preceding section, we normalize the power consumption of the adaptive receiver with the power consumed by a non-adaptive receiver that utilizes only the high linearity front end. By using (26), we obtain

$$\frac{P_{\mathrm{AFE,\,adaptive}}}{P_{\mathrm{AFE,\,fix}}} = \begin{cases} 1, & \frac{1}{\sqrt[3]{\mu}} p_{\mathrm{I,\,wc}} < p_{\mathrm{I}} \leq p_{\mathrm{I,\,wc}}, \\ \frac{1}{\sqrt{\mu}}, & p_{\mathrm{I}} \leq \frac{1}{\sqrt[3]{\mu}} p_{\mathrm{I,\,wc}}, \end{cases} \tag{50}$$

which, combined with (49), yields

$$\mathbb{E}\left\{\varsigma_{\mathrm{P}}\right\} = \delta + \frac{1-\delta}{\sqrt{\mu}}. \tag{51}$$

[18] This value is chosen in line with considerations from Section 4.1 and provides a fair comparison with other results in this section.

Average power savings of such a receiver are shown in Fig. 5d. For example, given that $\mu = 10$ dB, the range of OOB interferer values for which the high linearity AFE is activated (worst-case interference) is $(0.46\ p_{\mathrm{I,\ wc}},\ p_{\mathrm{I,\ wc}})$. If the interference power is inside this range for 10% of the time, the low linearity AFE would be used for the remaining 90% of the time and the average power savings compared to a non-adaptive design are 60%. Taking the ballpark power numbers for a front end from [19], this signifies a reduction of average front end power from 35 mW to 14 mW. Paper [19] also suggests a practical implementation of the interference sensing circuit, consisting of a passband filter and an energy detector. We include this sensor in the high-level conceptual illustration of an interference-adaptive receiver, shown in Fig. 5d. The sensor from [19] consumes 10 mW, which combined with the reduced average AFE power consumption (and neglecting the consumption of the logic circuitry) yields 24 mW, which is still 30% less than the power consumed by the non-adaptive receiver.

5 Conclusion

Based on a known result from circuit theory that has also been verified in practice, we determine scaling laws between performance and power consumption of an analog front end (AFE). The power consumption of the AFE is found to scale as $SIR^{-3/2}$ and at least as $SNDR^{3/2}$. These simple scaling laws can be used in a wide variety of communication-theoretic contexts, and some of the most important ones are explored. Namely, the power-SNR scaling law is extended to find the scaling laws between AFE power consumption and QAM constellation size, symbol error probability for QAM and error control coding gain and rate. Some general rules for low-power system design can be drawn from these laws: one example rule is that low-power applications favor "light" channel codes with moderate coding gains (such as simple convolutional codes) over more powerful ones, like turbo codes. Moreover, we derive laws that describe how front end power scales with environment parameters when performance is kept constant. Combined with fading and out-of-band blocker statistics, this enables us to determine theoretical average power savings of AFEs that adapt to the environment. The impressive results (about one order of magnitude reduction of power consumption in some cases) indicate that designing the front end so that it adapts to the environment is definitely a worthwhile effort.

Acknowledgement

The authors would like to thank the Swedish Foundation for Strategic Research (SSF), which provided the funding of this research in the scope of the Digitally

Assisted Radio Evolution (DARE) project.

References

[1] A. A. Abidi, G. J. Pottie, and W. J. Kaiser, "Power-conscious design of wireless circuits and systems," *Proceedings of the IEEE*, vol. 88, no. 10, pp. 1528–1545, Oct. 2000.

[2] C. Svensson, "Towards power centric analog design," *IEEE Circuits and Systems Magazine*, vol. 15, no. 3, pp. 44–51, thirdquarter 2015.

[3] Wenjun Sheng, A. Emira, and E. Sanchez-Sinencio, "CMOS RF receiver system design: A systematic approach," *IEEE Transactions on Circuits and Systems I: Regular Papers*, vol. 53, no. 5, pp. 1023–1034, May 2006.

[4] P. G. M. Baltus and R. Dekker, "Optimizing RF front ends for low power," *Proceedings of the IEEE*, vol. 88, no. 10, pp. 1546–1559, Oct. 2000.

[5] J. H. C. van den Heuvel, Y. Wu, P. G. M. Baltus, J. P. M. G. Linnartz, and A. H. M. van Roermund, "Front end power dissipation minimization and optimal transmission rate for wireless receivers," *IEEE Transactions on Circuits and Systems I: Regular Papers*, vol. 61, no. 5, pp. 1566–1577, May 2014.

[6] P. Baltus, "Minimum power design of RF front ends," Ph.D. dissertation, Department of Electrical Engineering, Technische Universiteit Eindhoven, 2004.

[7] M. Meghdadi and M. Sharif Bakhtiar, "Two-dimensional multi-parameter adaptation of noise, linearity, and power consumption in wireless receivers," *IEEE Transactions on Circuits and Systems I: Regular Papers*, vol. 61, no. 8, pp. 2433–2443, Aug. 2014.

[8] A. V. Do, C. C. Boon, M. A. Do, K. S. Yeo, and A. Cabuk, "An energy-aware CMOS receiver front end for low-power 2.4-GHz applications," *IEEE Transactions on Circuits and Systems I: Regular Papers*, vol. 57, no. 10, pp. 2675–2684, Oct. 2010.

[9] R. Senguttuvan, S. Sen, and A. Chatterjee, "Multidimensional adaptive power management for low-power operation of wireless devices," *IEEE Transactions on Circuits and Systems II: Express Briefs*, vol. 55, no. 9, pp. 867–871, Sep. 2008.

[10] S. Sen, D. Banerjee, M. Verhelst, and A. Chatterjee, "A power-scalable channel-adaptive wireless receiver based on built-in orthogonally tunable LNA," *IEEE Transactions on Circuits and Systems I: Regular Papers*, vol. 59, no. 5, pp. 946–957, May 2012.

[11] D. Banerjee, B. Muldrey, X. Wang, S. Sen, and A. Chatterjee, "Self-learning RF receiver systems: Process aware real-time adaptation to channel conditions for low power operation," *IEEE Transactions on Circuits and Systems I: Regular Papers*, vol. 64, no. 1, pp. 195–207, Jan. 2017.

[12] B. Razavi, *RF Microelectronics (2nd Edition) (Prentice Hall Communications Engineering and Emerging Technologies Series)*, 2nd. USA: Prentice Hall Press, 2011.

[13] J. Borremans et al., "A 40 nm CMOS 0.4–6 GHz receiver resilient to out-of-band blockers," *IEEE Journal of Solid-State Circuits*, vol. 46, no. 7, pp. 1659–1671, Jul. 2011.

[14] J. Xu, J. Yao, L. Wang, Z. Ming, K. Wu, and L. Chen, "Narrowband internet of things: Evolutions, technologies, and open issues," *IEEE Internet of Things Journal*, vol. 5, no. 3, pp. 1449–1462, Jun. 2018.

[15] S. Sen, "Invited: Context-aware energy-efficient communication for IoT sensor nodes," in *2016 53nd ACM/EDAC/IEEE Design Automation Conference (DAC)*, Jun. 2016, pp. 1–6.

[16] D. Banerjee, S. K. Devarakond, X. Wang, S. Sen, and A. Chatterjee, "Real-time use-aware adaptive RF transceiver systems for energy efficiency under BER constraints," *IEEE Transactions on Computer-Aided Design of Integrated Circuits and Systems*, vol. 34, no. 8, pp. 1209–1222, Aug. 2015.

[17] G. Fettweis, M. Lohning, D. Petrovic, M. Windisch, P. Zillmann, and W. Rave, "Dirty RF: A new paradigm," in *2005 IEEE 16th International Symposium on Personal, Indoor and Mobile Radio Communications*, vol. 4, 2005, pp. 2347–2355.

[18] J. G. Proakis and M. Salehi, *Digital communications, fifth edition*. McGraw-Hill, 2014.

[19] M. Abdulaziz, W. Ahmad, A. Nejdel, M. Törmänen, and H. Sjöland, "A cellular receiver front-end with blocker sensing," in *2016 IEEE Radio Frequency Integrated Circuits Symposium (RFIC)*, May 2016, pp. 238–241.

[20] C. Studer, S. Fateh, C. Benkeser, and Q. Huang, "Implementation trade-offs of soft-input soft-output MAP decoders for convolutional codes," *IEEE Transactions on Circuits and Systems I: Regular Papers*, vol. 59, no. 11, pp. 2774–2783, Nov. 2012.

[21] S. Belfanti, C. Roth, M. Gautschi, C. Benkeser, and Q. Huang, "A 1Gbps LTE-advanced turbo-decoder ASIC in 65nm CMOS," in *2013 Symposium on VLSI Circuits*, Jun. 2013, pp. C284–C285.

[22] S. L. Howard, C. Schlegel, K. Iniewski, and K. Iniewski, "Error control coding in low-power wireless sensor networks: When is ECC energy-efficient?" *EURASIP Journal on Wireless Communications and Networking*, vol. 2006, no. 1, p. 074 812, May 2006.

[23] P. Grover, K. Woyach, and A. Sahai, "Towards a communication-theoretic understanding of system-level power consumption," *IEEE Journal on Selected Areas in Communications*, vol. 29, no. 8, pp. 1744–1755, Sep. 2011.

[24] A. Goldsmith, *Wireless Communications*. USA: Cambridge University Press, 2005.

[25] M. Abramowitz and I. A. Stegun, *Handbook of Mathematical Functions with Formulas, Graphs, and Mathematical Tables*, ninth Dover printing, tenth GPO printing. New York: Dover, 1964.